Single-cell imaging in *Saccharomyces cerevisiae* uncovers a critical role for the G1/S transition activator Bck2 in cell size adaptation

Dissertation der Fakultät für Biologie
der Ludwig-Maximilians-Universität München

Yagya Chadha

Munich, April 2025

This work was carried out in the laboratory of Dr. Kurt Schmoller at the Institute of Functional Epigenetics, Helmholtz Centre Munich.

First examiner: Prof. Dr. Pascal Falter-Braun
Second examiner: Prof. Dr. Andreas Klingl
Date of submission: April 4th, 2025
Date of oral examination: October 13th, 2025

EIDESSTATTLICHE ERKLÄRUNG

Ich versichere hier mit an Eides statt, dass meine Dissertation selbständig und ohne unerlaubte Hilfsmittel angefertigt worden ist.
Die vorliegende Dissertation wurde weder ganz, noch teilweise bei einer anderen Prüfungs kommission vorgelegt.
Ich habe noch zu keinem früheren Zeitpunkt versucht, eine Dissertation einzureichen oder an einer Doktorprüfung teilzunehmen.

München, den 3. Dezember 2025

Yagya Chadha

Dedicated to the
Chadha and Hans lineages.
Thank you for
the nature and the nurture.

Table of Contents

Affidavit

Herewith I certify under oath that I wrote the accompanying Dissertation myself.

Title: Single-cell imaging in *Saccharomyces cerevisiae* uncovers a critical role for the G1/S transition activator Bck2 in cell size adaptation

In the thesis no other sources and aids have been used than those indicated. The passages of the thesis that are taken in wording or meaning from other sources have been marked with an indication of the sources (including the World Wide Web and other electronic text and data collections). Furthermore, all parts of the thesis that were de novo generated with the help of artificial intelligence tools were identified by footnotes/annotations at the appropriate places and the artificial intelligence tools used were listed. The prompts used were listed in the appendix. This statement applies to all text, graphics, drawings, sketch maps, and pictorial representations contained in the Work.

Munich, 3rd December 2025

(Location/date)

YAGYA CHADHA

(First and last name in block letters)

YAGYA CHADHA

(Signature)

Declaration

Hereby I declare that this work, complete or in parts, has not yet been submitted to another examination institution and that I did not undergo another doctoral examination without success.

Munich, 3rd December 2025

(Location/date)

YAGYA CHADHA

(Signature)

Parts of this work are published in:

Chadha, Y., Kukhtevich, I.V., Padovani, F., Schneider, R., Schmoller, K.M., 2024b. Single-cell imaging reveals a key role of Bck2 in budding yeast cell size adaptation to nutrient challenges. bioRxiv 2024.10.04.616606. https://doi.org/10.1101/2024.10.04.616606

Kukhtevich, I.V., Rivero-Romano, M., Rakesh, N., Bheda, P., Chadha, Y., Rosales-Becerra, P., Hamperl, S., Bureik, D., Dornauer, S., Dargemont, C., Kirmizis, A., Schmoller, K.M., Schneider, R., 2022. Quantitative RNA imaging in single live cells reveals age-dependent asymmetric inheritance. Cell Rep. 41, 111656. https://doi.org/10.1016/j.celrep.2022.111656

Padovani, F., Čavka, I., Neves, A.R.R., López, C.P., Al-Refaie, N., Bolcato, L., Chatzitheodoridou, D., Chadha, Y., Su, X.A., Lengefeld, J., Cabianca, D.S., Köhler, S., Schmoller, K.M., 2024. SpotMAX: a generalist framework for multi-dimensional automatic spot detection and quantification. bioRxiv 2024.10.22.619610. https://doi.org/10.1101/2024.10.22.619610

Chadha, Y., Khurana, A., Schmoller, K.M., 2024a. Eukaryotic cell size regulation and its implications for cellular function and dysfunction. Physiol. Rev. 104, 1679–1717. https://doi.org/10.1152/physrev.00046.2023

Acknowledgements

In the world as it is today, to be able to conduct and publish research freely feels like a privilege. I am grateful for having been able to immerse myself into this scientific pursuit for the last few years - an experience which has, paradoxically, felt selfish and selfless at the same time. Looking back, it has been a period of drastic personal and professional growth and will always be cherished. Like most research, this work was a collective effort and is built on the contributions and support of a lot of people.

First and foremost, I would like to thank my supervisor, Dr. Kurt Schmoller, for guiding me on how to navigate this research question and for teaching me the skills and the techniques that the question demanded. Kurt's expertise, patience and fairness have been inspiring and have made me a better scientist and a better person.

I would like to thank the members of my thesis advisory committee, Prof. Dr. Pascal Falter-Braun, who is also my official doctoral supervisor at the university, and Prof. Dr. Andreas Klingl. Thank you for taking out time to regularly review my progress and for sharing your invaluable input to shape this work. I would also like to express my gratitude towards Prof. Dr. Robert Schneider, head of the Institute of Functional Epigenetics (IFE), for his guidance and collaboration in this work as well as in the diSpinach RNA imaging project.

This work would have been impossible without the support of two incredible post-docs at the IFE: Dr. Igor Kukhtevich and Dr. Francesco Padovani. Igor's expertise in microfluidics-based microscopy was fundamental to most data acquisition in this work. Thank you, Igor, for your immense help with the numerous experiments and for the insightful discussions and advice. The massive image dataset would have been much more challenging to analyse had Francesco not created Cell-ACDC and SpotMAX. Thank you, Francesco, for customising Cell-ACDC to so many of my needs and for dealing with the bugs in the beta-version at lightning speed. Most importantly, thank you Francesco for patiently introducing me to Python and data analysis downstream of Cell-ACDC.

The members of the Schmoller group have been an absolute joy to work with. Thank you Daniela Bureik, Francesco Padovani, Kora-Lee Claude, Anika Seel, Dimitra Chatzitheodoridou, Benedikt Mairhörmann, Alissa Finster, Arohi Khurana, Luisa Hernández Götz and Timon Stegmaier for teaching me so many valuable lab and life lessons and for always having my back. I consider myself really fortunate to find such amazing friends in my colleagues and to go through this journey with you. I would also like to thank all members of the IFE for creating such a pleasant and cooperative

work environment. I express my gratitude to Sükriye Koccayir and Hanife Hisenaj whose work behind the scenes has been indispensable for the experiments included in this thesis.

Last but not the least, I would like to thank my family - Meenu, Sanjay and Lavya Chadha - for their endless support and love that has always encouraged me to expand my horizons. Thank you for being my role models and my safety net in my conventional and unconventional life choices. My gratitude extends to my grandmothers - Saroj Chadha and Gian Hans – two indomitable women who raised me to be resilient and open-minded. I am also deeply grateful to my partner, Bernhard Lederer, who stood by my side every day of this experience and brought an infectious lightness and optimism into my life. Thank you, Berni, for being an excellent companion, in thesis-writing and otherwise. I would also like to take this opportunity to thank Shweta Chaudhary, Anshul Sharma and Navya Sharma for being my rock and my home away from home. Finally, I would like to thank all my friends and family who have looked after me and strengthened me in this endeavour.

Abstract

In constant environments, cell size control maintains a constant mean cell size with a low variation in a process known as size homeostasis. In changing environments, cell size control must also adjust the mean cell size to the optimum for the new environment before implementing size homeostasis, in a process known as size adaptation. A wealth of data is available on eukaryotic size homeostasis, while comparatively little is known about size adaptation. This is partially because investigation of cell size control mechanisms requires single-cell information obtained through complex and time-intensive analysis of time-lapse microscopy data. This image analysis becomes even more complex in changing nutrient conditions as it additionally requires complete pedigrees and cell categorization. This work uses recent advances in machine-learning-assisted image analysis to characterize size adaptation to changing nutrients at the single cell level. Importantly, it reveals that in the eukaryotic unicellular fungus *Saccharomyces cerevisiae* (budding yeast), size regulators that appear redundant in size homeostasis serve unique functions in size adaptation.

Three major regulators of size homeostasis in budding yeast are the G1/S transition activator proteins Cln3 and Bck2, and the G1/S transition inhibitor, Whi5. Surprisingly, deletions of *WHI5, BCK2* or *CLN3* affect cell size but do not strongly disrupt size homeostasis efficiency. This work finds that a double deletion of *WHI5* and *BCK2* results in a strain that is surprisingly similar to wild-type cells in cell size and does not show a loss of size homeostasis efficiency during fermentative growth. Thus, there is an unexplained redundancy in size homeostasis, both in the sense that size homeostasis is robust to deletions of major size regulators and that regulators like Bck2 and Cln3, which are synthetically lethal, serve the same function of G1/S transition activation. Given that Whi5, Cln3 and Bck2 have all previously been linked to nutrient sensing or nutrient response, this work tested if changing nutrient conditions could reveal a cost of the *whi5Δbck2Δ* double deletion to size homeostasis. Nutrient-switch experiments from glucose to glycerol-ethanol media revealed that immediately after a nutrient switch, the *whi5Δbck2Δ* strain indeed had a worse size homeostasis efficiency than wild-type cells. Moreover, size homeostasis efficiency had not been systematically studied in changing environments before and this work reported a strong but temporary increase in cell size and decrease in size homeostasis efficiency after the nutrient switch.

Live cell microscopy coupled to a nutrient switch and followed by machine learning-assisted image analysis allowed tracking and categorization of individual cells as well as their progeny. This complex categorization revealed strong heterogeneous phenotypes within the cell population. All cells arrested in the ongoing cell cycle stage immediately after the switch. Cells that faced the switch in S/G2/M phase of the cell cycle, either as mother or bud, also arrested in the G1 phase of the next cell cycle, indicating that a memory of the nutrient switch persists in these cells. Strains that had a

BCK2 deletion experienced longer G1 arrests and more cellular overgrowth during those arrests than strains with a *CLN3* deletion, indicating a more critical role for Bck2 in exit from post-switch G1 arrests. Cln3 has previously been shown to be depleted upon a nutrient switch from rich to poor growth medium. Therefore, this work hypothesizes that a temporary nutrient-dependent depletion of Cln3 after the nutrient switch makes Bck2 the only available G1/S activator. Altogether, this work demonstrates that mimicking traits of natural environments in the laboratory can help resolve redundancies reported in steady-state studies.

List of Figures

List of Abbreviations

3D: three-dimensional

a.u.: arbitrary units

ACDC: analysis of cell division cycle

***ADE2*:** “Adenine requiring”, Budding yeast gene encoding a phosphoribosylaminoimidazole carboxylase

ANOVA: analysis of variance

***BCK2*:** “Bypass of C kinase”, Budding yeast gene encoding a serine/threonine-rich protein that activates the G1/S transition

***CCR4*:** “Carbon Catabolite Repression”, Budding yeast gene encoding a component of the CCR4-NOT complex

***CDC13*:** “Cell division cycle”, Fission yeast gene encoding a G2/M transition B-type cyclin

***CDC2*:** “Cell division cycle”, Fission yeast gene encoding the cyclin-dependent protein kinase Cdk1

***CDC25*:** “Cell division cycle”, Fission yeast gene encoding a tyrosine phosphatase that activates the G2/M transition

***CDKG1*:** “Cyclin dependent kinase”, *Chlamydomonas reinhardtii* gene encoding a D-type-cyclin-dependent-kinase

cDNA: complementary deoxyribonucleic acid

***CDR2*:** “Changed division response”, Fission yeast gene encoding serine/threonine protein kinase

***CglaLEU2*:** *Candida glabrata* (renamed to *Nakaseomyces glabratus*) gene encoding a 3-isopropylmalate dehydrogenase

***CglaTRP1*:** *Candida glabrata* (renamed to *Nakaseomyces glabratus*) gene encoding a phosphoribosylanthranilate isomerase involved in tryptophan biosynthesis

***CLN1*:** “Cyclin”, Budding yeast gene encoding a G1 cyclin (Cln1)

***CLN2*:** “Cyclin”, Budding yeast gene encoding a G1 cyclin (Cln2)

***CLN3*:** “Cyclin”, Budding yeast gene encoding a G1 cyclin (Cln3)

clonNAT: Nourseothricin

CV: Coefficient of Variation

DAPI: 4′,6-diamidino-2-PHENYLINDOLE

DNA: deoxyribonucleic acid

dNTP: deoxynucleotide triphosphates

ENO2: “Enolase”, Budding yeast gene encoding a phosphopyruvate hydratase

fL: femtolitre

FLAG-tag: octapeptide epitope made up of the sequence DYKDDDDK (D=aspartic acid, Y=tyrosine, K=lysine)

***GAL*:** Budding yeast genes involved in galactose metabolism

GFP: green fluorescent protein

GUI: graphical user interface

HF: high-fidelity

HTB2**:** “Histone h two B”, Budding yeast gene encoding the core histone protein H2B

IGO1/2**:** “Initiation of G0”, Budding yeast paralogue genes encoding two proteins that are required for the initiation of the G0 program

KlacURA3**:** *Kluyveromyces lactis* gene encoding an orotidine-5'-phosphate decarboxylase

KRP4**:** “Kip-related protein 4”, *Arabidopsis thaliana* gene encoding the Kip-related protein 4

LB: Luria-Bertani medium for propagation of *E.coli*

LED: light emitting diode

L-R: left to right

LSM: laser scanning microscope

MAT**:** Budding yeast mating type locus

MCM1**:** “mini chromosome maintenance”, Budding yeast gene encoding the transcription factor Mcm1

min: minutes

MPK1**:** Budding yeast gene encoding a serine/threonine mitogen-activated protein (MAP) kinase

mRNA: messenger ribonucleic acid

OD$_{\mathbf{600nm}}$**:** optical density measured at a wavelength of 600 nm

PEG: polyethylene glycol

PKA: protein kinase A

PKC1**:** “Protein kinase C”, Budding yeast gene encoding a protein serine/threonine kinase that is essential for cell wall remodeling during growth

PP2A: Budding yeast holoenzyme protein phosphatase 2A

RB**:** “Retinoblastoma”, Human gene encoding the Rb protein that negatively regulates the cell cycle.

RIM15**:** “regulator of IME2”, Budding yeast gene encoding a protein kinase involved in cell proliferation in response to nutrients

RNA: ribonucleic acid

Rpm: revolutions per minute

RT-qPCR: reverse-transcriptase quantitative polymerase chain reaction

SBF: “SCB-binding factor”, Budding yeast transcription complex made up of Swi4 and Swi6 subunits that binds the Swi4/6 cell cycle box (SCB) sequence in the DNA

SCD: synthetic complete medium with 2% glucose

SCGE: synthetic complete medium with 2% glycerol and 1% ethanol

SGD: *Saccharomyces* genome database

smFISH: single molecule fluorescence in situ hybridisation

SUT509**:** Budding yeast non-coding RNA

SWI4**:** “Switching deficient”, Budding yeast gene encoding the Swi4 protein which is the DNA binding subunit of the SBF transcription complex

TAE: Tris-acetate-ethylenediamine tetraacetic acid

TE: Tris-ethylenediamine tetraacetic acid

TNY1**:** *Chlamydomonas reinhardtii* gene encoding a cytosolic RNA binding protein

TOR: target of rapamycin

UBR5**:** Human gene encoding an E3 ubiquitin protein ligase

URA3**:** “Uracil requiring”, Budding yeast gene encoding an orotidine-5'-phosphate (OMP) decarboxylase

UV: ultraviolet

WHI5**:** “Whiskey”, Budding yeast gene encoding a protein that represses transcription in G1

Whi5-WIQ: Budding yeast Whi5 protein mutant where the amino acids R185, A189, and K192 have been mutated to W185, I189 and Q192 respectively.

WHI7**:** “Whiskey”, Budding yeast gene that is a paralogue of *WHI5* and an unstable repressor of transcription in G1

WT: wild type

YPD: yeast extract peptone medium with 2% glucose

1. Introduction

1.1. Cell size is tightly regulated

Cell volume can vary drastically across diverse eukaryotes, spanning a range of over 14 orders of magnitude[2,3]. While cell populations of distinct cell types can have very different mean cell masses, the variability observed within the mass distribution of a given cell type is surprisingly low, as assessed by the coefficient of variation (CV) of cell mass[4] (Fig.1). This indicates that cell size is tightly regulated around the optimum for each cell type (Fig.1). Cell size is a strong regulator of cell function[5–8], which could potentially explain why cells evolved such strict size regulation. Cell size sets the scale for the abundance of biomolecules and organelles within the cell as well as the scale of biosynthesis. Bigger cells have higher total transcript content[9,10] and higher total protein content[11,12]. Thus, total transcript and proteome amounts scale with cell size, and their concentrations are constant at most sizes within the physiological range. However, at large cell volumes near the upper extreme of the physiological range, this scaling breaks down as the genome becomes limiting, leading to cytoplasmic dilution[11,13]. It is therefore no surprise that abnormally large cell size has often been correlated with disease states such as cancer and obesity, and with cellular senescence and cellular aging[14–19]. For many years, this correlation was attributed to increased cell size potentially being just a phenotypic consequence of the cell's dysfunction. Exciting new work challenges this narrative, showing that increased cell size may even be causative for some cellular dysfunction states such as senescence and aging[20–23]. These findings not only emphasise the role of cell size homeostasis in maintenance of robust cell function but also reiterate a need for understanding the size homeostasis system that affects virtually all intracellular processes.

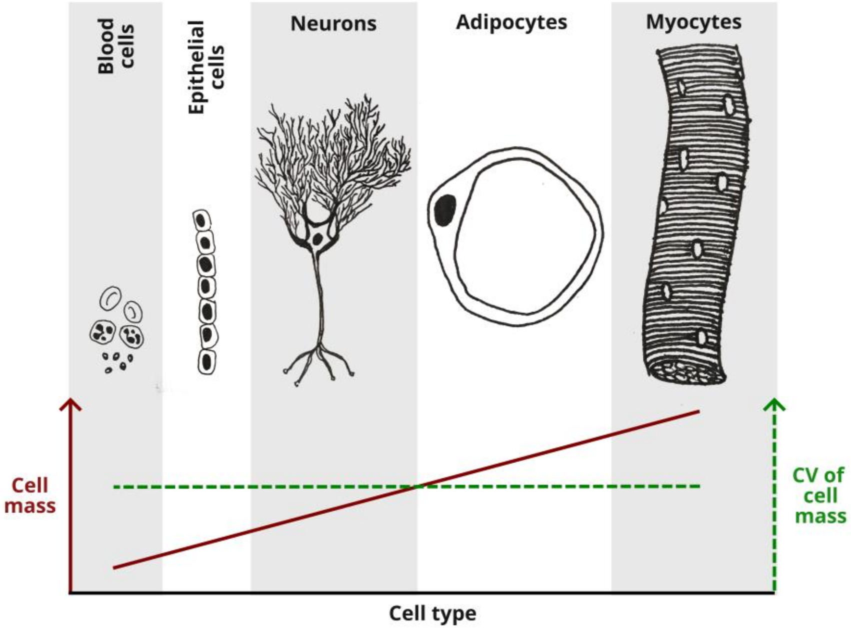

Figure 1: Cell mass varies drastically between different cell types but CV of cell mass does not. Schematic representation adapted from the study by Hatton *et al.*[4]. While the average cell mass of certain cell types such as myocytes can be many orders of magnitude more than that of other cell types, such as blood cells, the CV of cell mass does not vary between the cell types, indicating presence of cell type specific size control. Example cell illustrations are not drawn to scale.

1.2. The mechanism of cell size homeostasis

If a proliferating cell is born with a deviation in cell size, the deviation can be corrected either by modulation of the growth rate or the time until the next division[24] (Fig. 2). For example, a cell that is born too small can either spend more time in the cell cycle to grow closer to the average population size or can achieve the same size in a shorter duration by increasing its growth rate. Thus, cell size homeostasis emerges from a coupling of cell growth and cell division to cell size. The coupling of cell growth to cell size is well described in mammalian cells, where the absolute cellular growth rate has been found to be negatively correlated with cell volume to maintain size homeostasis[25,26]. Perturbations of cell size or cell cycle durations in mammalian cells have been shown to lead to compensatory modulations of growth rates[25,26]. Mechanistically, this coupling of cell growth to cell size has been attributed to increased protein degradation via global activation of proteasomes in larger cells[27]. While this coupling between cell growth and cell size is only now beginning to be understood, the coupling of cell division or cell cycle progression to cell size has long been reported in diverse model organisms and multiple mathematical models have been proposed to explain it[23,25,28–33].

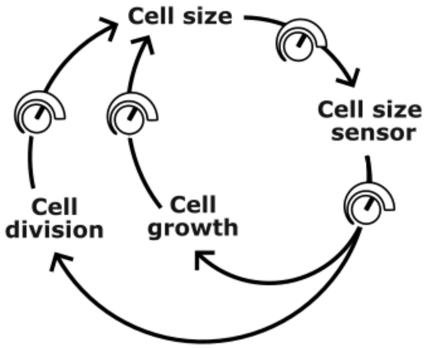

Figure 2: Cell size homeostasis is implemented through a coupling of cell growth and cell division to cell size. A cell size sensor mechanism allows cell growth and cell division to be regulated based on the current size of the cell. Cells born smaller than the target size can either increase their growth rate or delay cell division. This regulation allows cell size in the following generation to be closer to the target cell size. Cells born bigger than the target size shorten the time until cell division to minimise growth during the current cell cycle.

The main difference between these models coupling cell division to cell size is the parameter that controls cell division. In the *adder* model, for example, cells add a fixed amount of volume in every cell cycle, independent of their birth volumes (Fig. 3A). Cell division occurs once the cell has increased in volume by this fixed amount. Alternatively, in the *sizer* model a critical size threshold is met before cell division i.e., only cells that attain a certain size go through cell division (Fig. 3A). A *sizer* mechanism requires cells that are born smaller to grow more before division, thereby reducing cell size variation at division. Theoretically, a strong, close-to-ideal *sizer* can correct size deviations within a single cell cycle whereas an *adder* would need multiple cell cycles to do the same[32]. The third model coupling cell division to cell size is the *timer*, in which cells spend the same duration of time in the cell cycle before division (Fig. 3A). As per the *timer*, cells of all sizes undergo the same cell cycle duration. The effect of the *timer* on cell size therefore depends on whether the cells grow linearly or exponentially. Linear growth means that cells of all sizes have the same growth rate, i.e., grow in volume at the same speed. In exponential growth, on the other hand, cells that are bigger grow proportionally faster. A *timer* in linear growth, therefore, leads to all cells growing by the same amount in a fixed time period, and is, in effect, the same as an *adder*. Conversely, in exponentially growing cells, a *timer* leads to a widening of the size distribution (Fig. 3A) and therefore does not qualify as a size homeostasis mechanism alone[32]. It is important to note here that size homeostasis mechanisms associated with these models do not always control cell division but can also control other cell cycle phase transitions i.e., they can be modular and cell-cycle-phase specific. For example, in budding yeast, a weak *sizer* is observed in G1 and a *timer* is observed in S/G2/M but an *adder* is observed when the whole cell cycle is considered[31,34–36]. Moreover, multiple models can influence the same cell cycle phase transition. For example, the fission yeast G2/M transition is controlled based on cell surface area, cell volume and time information[37] and an overall *sizer* emerges over the complete cell cycle[28,37]. In fact, the fission yeast *sizer* is one of the strongest known size homeostasis systems in eukaryotes and can correct most cell size deviations within a single cell cycle[38]. Proulx-Giraldeau *et al*.[35] used simulations of size homeostasis evolution to find that the relative lengths of cell cycle phases contribute to the size homeostasis model that emerges over the entire cell cycle. Thus, the size homeostasis model in the longer cell cycle phase is likely to dominate the size homeostasis model that is observed over the complete cell cycle. They also found that if a *sizer* occurs earlier in the cell cycle and is followed by a *timer*, as seen in budding yeast, an overall *adder* is likely to emerge over the complete cell cycle. On the contrary, if a *timer* precedes the *sizer* in the cell cycle, as seen in fission yeast, an overall *sizer* is likely to emerge. The overall adder in Proulx-Giraldeau *et al*.'s simulated observation was supported by the experimental budding yeast model from Chandler-Brown *et al.*[34]

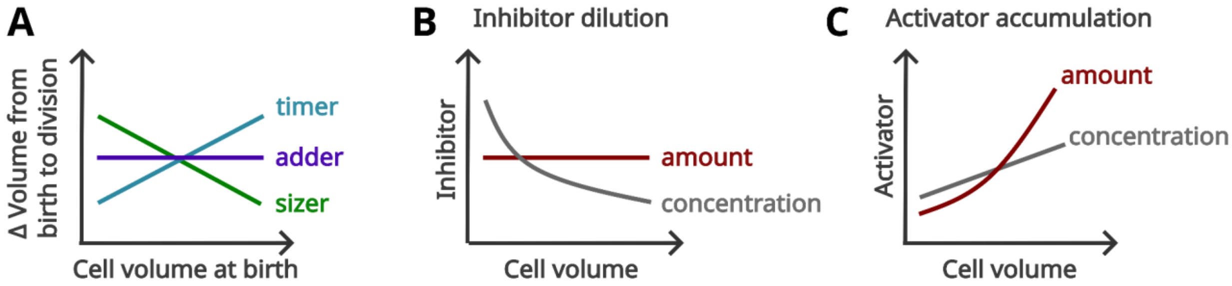

Figure 3: Cell size homeostasis models in proliferating cells and the biochemical mechanisms behind size-sensing. (**A**) The relation between cell growth during the cell cycle and cell volume at birth is plotted for sizers (green), adders (purple) and timers (blue) in exponentially growing cells. (**B**) As an example of the *inhibitor-dilution* size-sensing mechanism, the trends in amount (red) and concentration (grey) of a cell cycle phase inhibitor are shown as a cell grows in volume. The same is plotted in (**C**) as an example of *activator-accumulation*. Figure adapted from the review by Chadha *et al*.[14].

Sizers, *adders* and *timers* are facilitated through molecular mechanisms that can sense cell size, cell growth and time, respectively. These molecular sensors are typically cell volume- or time-based changes in concentrations of reporter proteins that can in turn tune cell cycle progression. For example, the cell-growth based dilution of an inhibitor of a cell cycle phase transition allows the likelihood of the transition to increase with an increase in cell size. This mechanism is referred to as *inhibitor-dilution* (Fig. 3B). Typically, the amount of an inhibitor remains constant as the cell grows and the concentration decreases with an increase in cell volume, leading to dilution of the inhibitor (Fig. 3B). Alternatively, the accumulation of a cell cycle transition activator with cell growth or time also leads to a higher likelihood of transition after a threshold amount of cell growth has occurred or time has elapsed. This mechanism is referred to as *activator-accumulation* (Fig. 3C). In this mechanism, the amount of the activator superscales with cell volume, leading to higher concentrations of the activator in bigger cells (Fig. 3C).

Both *inhibitor-dilution* and *activator-accumulation* have now been reported in diverse organisms[14]. For example, in the budding yeast *Saccharomyces cerevisiae*, cell size-based dilution of the G1/S transition inhibitor protein, Whi5, allows size-dependent G1/S transition[39]. Similarly, size-dependent G1/S transition in the shoot apical meristem of the flowering plant *Arabidopsis thaliana* occurs due to the cell growth-based dilution of the indirect G1/S inhibitor protein KRP4 (KIP-related protein 4)[40]. In animal cells, the functional homolog of yeast Whi5, Rb, has been identified as a potential size sensor protein. Rb is an inhibitor of the G1/S transition and its concentration decreases as animal cells grow in size in G1[41,42]. This decrease in concentration of Rb is implemented through its degradation via the E3 ligase UBR5[43]. Alongside size-dependent modulation of G1 duration, animal cells have also been shown to modulate their growth rate based upon cell size[25,26]. In the single-cell alga *Chlamydomonas reinhardtii*, two size sensing mechanisms have been discovered. The first one is the size-dependent accumulation of the G1/S activator CDKG1, a cyclin-dependent kinase that superscales with cell size during late G1, i.e., increases in concentration as cell size increases[44,45]. The second size-sensing mechanism is a form of *inhibitor-dilution*, where an RNA-binding protein, TNY1, that represses CDKG1 has been found to subscale with cell size during G1[45]. In the fission yeast *Schizosaccharomyces pombe*, *activator-accumulation* is observed for two G2/M transition activators: Cdc25, whose nuclear concentration accumulates with an increase in cell volume, and Cdc13, whose nuclear concentration accumulates over time[37]. A third fission yeast G2/M activator, Cdr2, is localised in cortical nodes in a band around the central part of the cell. The density of these cortical nodes in the medial cell cortex increases with an increase in cell surface area, thereby integrating surface area information into the mitotic-entry decision[30,46]. These examples illustrate that similar size-sensing strategies based on reporter concentrations have evolved across eukaryotes and understanding mechanisms of size homeostasis in one organism can provide fundamental insights into size homeostasis in other organisms. Improved knowledge of size homeostasis mechanisms could prove valuable for diagnosing, treating and possibly even preventing disease states that are correlated with disrupted cell sizes.

1.3. The budding yeast *Saccharomyces cerevisiae* as a model organism for cell size control

A lot of what is known about size homeostasis today comes from extensive studies performed on unicellular organisms such as the fission and budding yeasts. In the 1970s and 1980s, both yeasts had successfully been used as model organisms in the discovery and characterisation of cell cycle regulators[38,47–53]- work that earned Leland H. Hartwell, Sir Paul M. Nurse and Tim Hunt the Nobel Prize in Physiology in 2001. This early research on cell cycle regulation in budding and fission yeasts described the coupling between cell division and cell size and introduced the concept of a 'critical size' for yeast cell cycle progression[50,54]. These results were in agreement with the observations made by Killander and Zetterberg in mammalian cells in the 1960s[33,55], stating that a 'critical cell mass' seemed to initiate DNA synthesis. Together, these studies laid the foundation of the eukaryotic size homeostasis field. It was later discovered that both the budding yeast and the human homologues of the fission yeast *CDC2* gene, which encodes the cyclin-dependent protein kinase Cdk1, could rescue the fission yeast *cdc2* mutant [56–58], indicating that cell cycle control machinery was largely conserved from yeast to humans. Today, it is known that about 50% of essential budding yeast genes can be functionally replaced by their human homologues despite an evolutionary separation of 1 billion years between the two organisms[59–61]. Moreover, around 30% of human genes known to be involved in disease have a budding yeast homologue[59,62]. This high level of conservation of basic cellular processes between budding yeast and humans makes budding yeast a powerful tool for explorative research in eukaryotic biology. One example where budding yeast research was successfully translated into understanding a mammalian mechanism is the *inhibitor-dilution* size-sensing mechanism. This mechanism was first described in budding yeast for the size-sensing G1/S transition inhibitor, Whi5, which is diluted in concentration by cell growth during G1[39]. The study of the mammalian functional homologue of Whi5, Rb, led to the discovery of a similar size-sensing strategy in mammalian cells[41–43]. Rb concentration was also found to decrease during the G1 phase and this decrease is now known to be executed by a degradation of Rb via the E3 ligase UBR3[41–43]. These similarities indicated that not only mechanisms of cell cycle regulation, but also those of cell size regulation may be conserved from yeast to mammals.

Apart from being well-studied in the size homeostasis field (sections 1.4-1.8) and exhibiting strong conservation with distant eukaryotes, budding yeast has many other qualities that make it a suitable model organism for this project. It was the first eukaryote to have its genome fully sequenced, leading to the development of a plethora of tools for its genetic manipulation[59,63]. The complete budding yeast genome is annotated in a publicly accessible online database called the Saccharomyces Genome Database (SGD)[64]. Budding yeast's high efficiency of homologous recombination coupled with the ready availability of genomic information and molecular tools makes it an ideal model organism for gene additions, deletions or modifications[65]. Additionally, budding yeast has very short cell cycles of around 90 minutes, making it easy to maintain and propagate in the laboratory[65]. These short cell cycles also make it a suitable model organism for time-lapse microscopy experiments as they allow imaging of multiple generations of cells. Another characteristic of budding yeast that is advantageous for time-lapse microscopy is its immotility, which enables easy recognition of the same cell over multiple time points of imaging. The simple ovoid or spherical morphology makes it a relatively easy cell to segment in downstream image analysis[66]. Moreover, multiple well-established experimental protocols, such as single-molecule fluorescence in-situ hybridisation (smFISH), fluorescent-protein tagging and reverse-transcriptase quantitative polymerase chain reactions (RT-qPCRs) are available for quantification of RNA and proteins in yeast cells. Together, these qualities make budding yeast an ideal model organism for projects requiring genetic manipulation, observation of cell cycle phenotypes and RNA and protein visualisation and quantification.

1.4. The budding yeast G1/S size homeostasis network

Budding yeast G1 is the initial gap phase of the cell cycle where the cell grows in size but has not yet begun to bud or replicate its genome[67] (Fig. 4A). The transition from G1 into S phase is a commitment to cell division that kicks off the expression of the G1/S regulon, a set of about 200 genes[68,69] (Fig. 4A-B). This point of commitment to the G1/S transition and cell division is called *Start*[69] (Fig. 4A). S-phase is marked by DNA replication and bud emergence, and is followed by a second gap phase G2[67], during which the cell prepares for mitosis (Fig. 4A). Most cell growth during the S and G2 phases occurs in the bud[34]. G2 is followed by mitosis, during which the chromosomes are separated into the mother and the bud and the cell divides to give rise to two G1 cells[67] (Fig. 4A). Size homeostasis in budding yeast is most apparent at the *Start* checkpoint of the G1/S transition[34,39], supported by studies that have reported longer G1 durations in cells that are smaller at birth[50,70]. The underlying size-sensing at the *Start* checkpoint is attributed to the *inhibitor-dilution* model[39,71–73]. Additionally, there is increasing evidence of a second size checkpoint in the G2/M phase that ensures sufficient bud growth occurs before cell division[36,74,75].

This work is focused on regulators involved in the G1/S size homeostasis network. The protein Whi5 binds the transcription factor complex SBF and inhibits expression of the G1/S regulon, thereby keeping cells in G1 for longer[76,77]. At the start of G1, all cells have roughly equal amounts of Whi5, and Whi5 synthesis during G1 is negligible[39] (Fig. 5A). The amount of Whi5 therefore remains largely constant as the cell grows in size during G1 and the concentration of Whi5 continually decreases[39,71,72,78,79] (Fig. 5A). This dilution of the G1/S inhibitor Whi5 with the increase in cell size during G1 serves as a size sensing mechanism. Two activators of the G1/S transition, Cln3 and Bck2, also bind SBF and promote expression of the G1/S regulon[76,77,80,81] (Fig. 4B). The synthesis of Cln3 and Bck2, unlike that of Whi5, scales with size and they are maintained at a constant concentration during G1[39] (Fig 5B). The shifting balance between the constant concentrations of G1/S activators and the decreasing concentration of the G1/S inhibitor increases the likelihood of

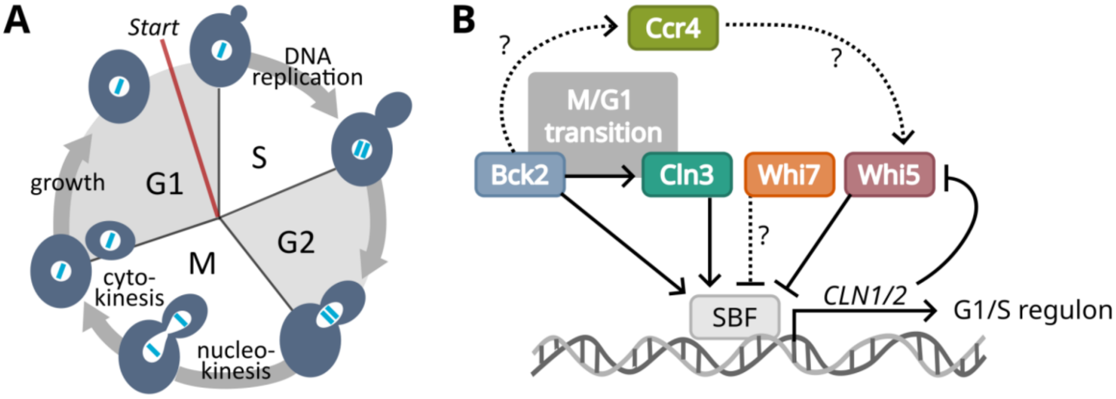

Figure 4: The budding yeast cell cycle and G1/S size homeostasis network. (**A**) The budding yeast cell cycle is divided into G1, S, G2 and M phases. The cell is represented in dark blue, the nucleus in white and the genome in light blue. G1 is the initial gap phase during which cell growth occurs. The *Start* checkpoint is located near the end of G1. Once cells attain a threshold size, they pass *Start* and enter S-phase, committing to cell division. The bud emerges at the start of S-phase and grows over the S, G2 and M phases. S-phase is also marked by DNA replication. G2 is the second gap phase during which the cell prepares for mitotic division. G2 is followed by M phase or mitosis, during which the nucleus divides (nucleokinesis) and enters the bud, followed by cell division (cytokinesis). Cell division gives rise to two new G1 cells. (**B**) The transcription factor complex SBF promotes expression of the G1/S regulon which enables the G1/S transition. SBF is inhibited by Whi5 and activated by Cln3 and Bck2. Upon expression of the G1/S regulon, the two cyclins Cln1 and Cln2 are expressed early on. These cyclins in turn inhibit Whi5 to form a positive feedback loop that makes the G1/S transition switch-like. Bck2 was found to promote expression of Cln3 at the M/G1 transition. Whether or not Bck2 also regulates Whi5 mRNA by activating the cytoplasmic deadenylase Ccr4 is yet to be confirmed. Additionally, while Whi5 is the major G1/S inhibitor under normal conditions, Whi7, a paralog of Whi5, is known to be the major G1/S inhibitor during conditions of cell wall stress. Whether Whi7 compensates for Whi5 in a *whi5Δ* mutant is not yet known.

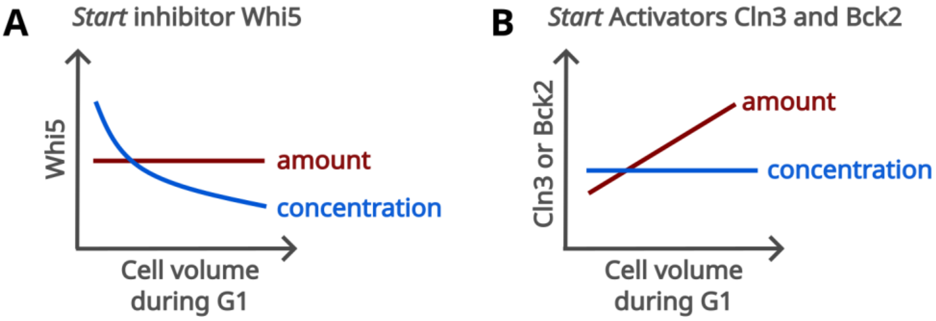

Figure 5: Trends in amounts and concentrations of *Start* regulators. (A) The size sensing attributed to the budding yeast *Start* inhibitor Whi5 can be explained by the size dependence of its concentration during G1. Since Whi5 synthesis is negligible during G1, its amount remains constant. As cell size increases due to G1 growth, the concentration of Whi5 continually decreases. (B) The synthesis of *Start* activators Cln3 and Bck2 scales with cell size, which means that the amount of these proteins increases as cells grow in G1. Their concentrations, therefore, remain constant.

the cell to pass *Start* when a threshold cell size is achieved. The expression of cyclins Cln1 and Cln2 at *Start* constitutes a positive feedback loop. The cyclins form a complex with the cyclin dependent kinase Cdk1, which hyperphosphorylates Whi5 and leads to its export from the nucleus, thereby further promoting transcription of the G1/S regulon[69,82] (Fig. 4B). *Start* or the commitment to cell cycle progression has been reported to occur when this positive feedback loop is triggered and 50% of Whi5 is exported from the nucleus[83]. This positive feedback loop ensures the switch-like behaviour of the G1/S transition. In this manner, the *inhibitor-dilution* model enables the coupling of cell cycle progression to cell size. The major proteins involved in the budding yeast G1/S size homeostasis network are discussed in further detail in the following sections.

1.5. Major regulators in the G1/S size homeostasis network

Discovered in a screen for gene deletions leading to smaller cell sizes[84] and allegedly named after a bet over a bottle of whiskey between two investigators[85], the **Whi5** protein has been an important point of discussion in the budding yeast cell size field in the last decade. After Whi5 was described as a potential cell size sensor in 2015[39], the dilution of the protein during G1 was disputed by studies from Litsios *et al*.[86], Dorsey *et al*.[87] and Tollis *et al*.[88]. However, reanalysis of the primary data from Litsios *et al*.[86] indeed confirmed the dilution of Whi5 during G1[71], and clarified that the differences in conclusions stemmed from differing analytical approaches. The dilution of Whi5 has since been reported by independent studies from at least six research groups, and has been observed despite differences in strains, techniques and analysis methods[71–73,79,89]. The observation of similar *inhibitor-dilution* strategies in plants and animals, as discussed in section 1.2, further supports the existence of such a mechanism in budding yeast.

Whi5 localises to the nucleus in a cell cycle dependent manner, entering it just before cell division and staying in the nucleus until the positive feedback loop of the G1/S transition is triggered[90]. Once the expression of the G1/S regulon starts, the cyclin dependent kinase Cdk1, in association with cyclins Cln1 and Cln2, hyperphosphorylates Whi5, leading to its export from the nucleus and ending its inhibition of SBF[76,77,82] (Fig. 4B). The dilution of Whi5 during G1, therefore, occurs while it is localised in the nucleus, the size of which is tightly coupled to cell size[91]. Whi5 re-enters the nucleus during telophase in mitosis[90] and is partitioned in equal amounts to the mother and daughter at division, likely by being bound to chromatin and segregating with the genome[78].

Whi5 concentration during G1 can predict the rate at which cells pass *Start* but only when **Bck2**, the aforementioned activator of the G1/S transition, is deleted[39]. This implies that while Whi5 may be the only identified size-sensor protein, other proteins such as Bck2 also regulate cell size as well as the G1/S transition. At the G1/S transition, Bck2 promotes expression of *CLN2* by binding to the transcription factors SBF and Mcm1[80,92] (Fig. 4B). Bck2's interaction with Mcm1 also allows it to promote expression of Swi4, a part of the SBF complex, and of Cln3 at the M/G1 transition[80] (Fig. 4B). As expected, a loss of Bck2 leads to a delayed G1/S transition and an increased cell size[77,93]. Nevertheless, Bck2 is still a poorly understood protein, with one known conserved domain - the transcriptional activation domain- and some similarity to an RNA binding domain[80,92]. It was discovered in a screen for suppressors of a C-type kinase (Pkc1) mutation and hence got the name Bypass of C-type Kinase (Bck2)[94]. The Pkc1 kinase is required for yeast cell wall remodelling as the cell grows[94]. Bck2 induces expression of around 20 proteins involved in cell wall structure or biosynthesis, which could explain how its overexpression rescues the lethality of the *pkc1Δ* mutation[92].

Another reason Bck2 is important in the discussion of the G1/S size homeostasis network is that it is synthetically lethal alongside **Cln3**, another activator of the G1/S transition[95] (Fig. 4B). The presence of one of the two activators is necessary for G1 exit and cell viability. Cln3 is a G1 cyclin that, in a complex with the cyclin-dependent kinase Cdk1, activates the G1/S transition by phosphorylating RNA polymerase II to promote expression of SBF target genes[81] (Fig. 4B). Thus, the mechanisms by which Cln3 and Bck2 activate the G1/S transition are fundamentally different but their deletions lead to the similar phenotype of increased cell volume[77,93]. Unlike Whi5, Cln3 and Bck2 are maintained at a constant concentration during G1[39] (Fig. 5B).

These observations make it abundantly clear that G1/S size homeostasis integrates inputs from multiple regulators, of which Whi5 is the only known size sensor. It has been proposed that the dilution of Whi5 during G1 may be a form of titration against the constant concentrations of other proteins in the size homeostasis network, and that the balance between G1/S inhibitors and activators dictates the likelihood of commitment to the G1/S transition[73]. The fact that other activators and inhibitors of the G1/S transition have been identified[73,96] and modulations of Whi5 abundance only partially disrupt size homeostasis[73,78,79] further supports the existence of multiple redundant inputs regulating the G1/S transition decision.

1.6. The redundancy in budding yeast size homeostasis

An obvious advantage of having multiple regulators of size homeostasis is the robustness it provides against loss or malfunction of single regulators. Indeed, we know from previous bulk studies that when *CLN3*, *WHI5* and *BCK2* are individually deleted, the average cell size of the population shifts, but the efficiency of cell size homeostasis, as assessed by the coefficient of variation (CV) of cell size, remains largely unchanged[73,77,93]. The CV is a mean-normalised measure of the standard deviation in a population. The normalisation to the mean makes the CV a measure of size homeostasis efficiency that is comparable between differently sized strains. The higher the CV of cell volume, the more variable is the cell volume in the population and the worse is the size homeostasis efficiency. While the *whi5Δ* mutant is smaller than wild-type (WT) cells and the *bck2Δ* and *cln3Δ* mutants are bigger than WT, their CVs of cell volume are very similar to that of WT[39,73,77,93]. Interestingly, bulk experiments show that even strains with double deletions of *whi5Δbck2Δ* or *whi5Δcln3Δ* have mean cell volumes that are very similar to WT[77]. This evidence indicates that size homeostasis is robust to the deletions of important size regulator proteins. While such robustness is one explanation for why cells have evolved multiple redundant *Start* regulators, another possible explanation is that the apparently redundant regulators such as Bck2 and Cln3 fulfil unique roles in specific conditions that have not yet been identified. In fact, Bck2 and Whi5 have previously been proposed to be involved in nutrient sensing and Cln3 has been shown to be extremely sensitive to nutrient availability[72,80,89,97,98]. This raises the question of whether the robustness of size homeostasis and the phenotypic redundancy between Cln3 and Bck2 persist under changing nutrient conditions, which is addressed in section 1.8. Before that, it is important to consider that the observed redundancy in size homeostasis could also stem from the presence of additional size regulating proteins that can compensate in the absence of or regulate known size regulators. The next section (section 1.7) describes two such potential candidates.

1.7. Other potential candidates in the Bck2-Cln3-Whi5 network

To better understand the redundancy in size homeostasis at the G1/S transition, it is imperative to also test the potential contribution of two proteins - Whi7 and Ccr4. **Whi7** is a paralogue of Whi5 that arose from a whole genome duplication event[99]. Like Whi5, Whi7 is also an inhibitor of *Start* (Fig. 4B) but its deletion leads to only a small reduction in cell size at budding[100]. One study finds that in asynchronous cultures, a deletion of *WHI7* has no effect on the average cell size of the population[99]. Thus, under normal conditions, Whi5 is the major transcriptional repressor in G1, likely due to the instability and low abundance of Whi7[99,101,102] (Fig. 4B). On the contrary, Whi7 expression is upregulated in conditions of cell wall stress and it serves as a cell cycle brake during the cell wall stress response[101–103]. It is, therefore, a possibility that the only partial loss of size homeostasis observed in the *whi5Δ* mutant is due to compensation for the absence of Whi5 by an upregulation of Whi7. Thus, testing whether Whi7 compensates in a *whi5Δ* mutant would be key to obtaining a complete picture of the G1/S size homeostasis network.

The second protein of interest is the cytoplasmic deadenylase **Ccr4**. As part of the Ccr4-Not complex, this protein is involved in the global regulation of mRNAs at all stages: production, export from the nucleus, translation and degradation[104,105]. A singular study by Manukyan *et al*.[106] proposes that Bck2 stimulates Ccr4 to degrade *WHI5* mRNA (Fig. 4B). They observe abnormally large cells in the *CCR4* deletion and an increase in the stability of *WHI5* mRNA in a *GALpr-WHI5 ccr4Δ* strain after a switch from galactose to glucose medium[106]. Specifically, they turn off *GALpr-WHI5* expression by switching cells from galactose to glucose medium and then use northern blotting to compare *WHI5* mRNA amounts at multiple time points after the switch. They find that *WHI5* mRNA stability is higher in a strain with a *CCR4* deletion as compared to one with no *CCR4* deletion. Thus, they propose that Ccr4 regulates cell size by degrading *WHI5* mRNA. However, since this is a bulk study on cells carrying *WHI5* under the control of a non-endogenous promoter in changing nutrient conditions, it begs the question of whether the phenotype can be reproduced at the single-cell level in steady-state conditions with the endogenous *WHI5* promoter. This remains to be tested and would again be crucial for furthering the understanding of the G1/S size homeostasis network.

1.8. Size homeostasis in changing nutrients

Most studies on cell size homeostasis have been conducted in steady-state conditions, *i.e.*, on cells in the exponential phase of growth in constant environments. However, outside the laboratory, microorganisms often encounter rapid changes in the nutritional quality of their environments and must adapt their size to the changed environment. As has long been known, the nutrient availability in the environment is a major regulator of cell size, with richer nutrients leading to higher cell volumes[50,72]. Studies have shown that changing nutrients can affect cell size through a modulation of both cell growth and cell cycle progression. For example, different nutrients lead to different cellular growth rates, which has in turn been proposed to lead to different ‘critical’ sizes at which cells pass *Start*[107]. In theory, such a growth-rate-dependent *sizer* can facilitate quick size adaptation to nutrient changes, so long as they affect the growth rate[107]. Nutrient availability can also affect cell cycle progression, as shown by Irvali *et al*.[108], who followed single live cells through a nutrient change and found that starving post-*Start* cells leads to a re-entry of Whi5 into the nucleus and a reversal of Cdk1 activation. This revealed that the commitment to the G1/S transition, which was so far thought to be irreversible, is reversible under conditions of starvation. They also discovered that the specific cell cycle stage of the cell at the time of nutrient deprivation affects how quickly the cell re-imports Whi5 into the nucleus and thereby affects the cell’s response to the nutrient deprivation. Another example of nutrients affecting cell cycle progression comes from Leitao *et al*.[74], who used changing nutrients to investigate if nutrient modulation of cell size was limited to the G1/S transition or if it also occurred at other points in the cell cycle. Indeed, they identified an additional layer of size homeostasis in buds during mitosis, which takes into account the nutritional status of the environment and accordingly regulates the duration of bud growth before mitotic exit[74,75]. Cell cycle arrests in all stages of the cell cycle have been observed upon acute nutrient deprivation[108–110], further confirming that nutrients can affect cell cycle progression.

Multiple biochemical pathways involved in nutrient sensing have been described in budding yeast[14,111,112]. Nutrient-specific receptors and transceptors (transporter-receptors) detect nutrient availability and signal it to the major pathways regulating cell growth and metabolism: the TOR (target of rapamycin) and PKA (protein kinase A) pathways[111,113–115] (Fig. 6). Thus, the biochemical link between nutrient sensing and growth regulation is well-characterised. Relatively lesser is known about how nutrient sensing is linked to cell cycle progression. One way that nutrient signals could regulate cell cycle progression could be through the regulation of cell growth itself[111], with cell growth leading to *inhibitor-dilution* or *activator-accumulation* (Fig. 6). Additionally, the TOR and PKA pathways have been shown to regulate cell cycle regulators such as Whi5 and Swi4 either through the Greatwall-Endosulfine-PP2A circuit or directly[111,116–118] (Fig. 6). In budding yeast, Greatwall is known as Rim15 and Endosulfine refers to two small proteins Igo1 and Igo2[118] (Fig. 6). Whether nutrient sensing can directly regulate cell cycle progression, or whether other cell cycle regulators may be regulated by TOR and PKA or involved in nutrient sensing itself, is not clear. There is a gap in the field's knowledge about how cell size adaptation to changing nutrients works at the single cell level, how size homeostasis efficiency is affected by a nutrient change and how size homeostasis is reinstated following a nutrient shift. Observing single cells undergoing a nutrient switch could help answer many of these questions.

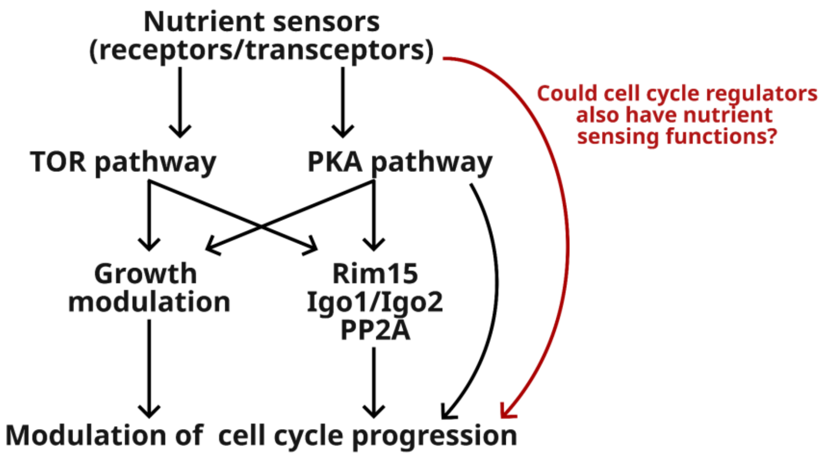

Figure 6: The main pathways involved in nutrient signalling dependent growth and cell cycle modulation. Nutrient sensors relay nutrient availability to the TOR and PKA pathways. These pathways accordingly modulate cell growth. The cell growth, in turn, can affect cell cycle progression by affecting the cell size. Additionally, the TOR and PKA pathways have also been shown to regulate Rim15 activity, which, via the Igo1-Igo2 complex and PP2A, can regulate the activity of cell cycle regulators. Whether nutrient sensing can directly regulate cell cycle progression, or whether major cell cycle regulators can respond to nutrient availability are open questions in the field.

Because changing nutrient conditions require dynamic adaptation of cell size, it is possible that size regulators that appear redundant in steady-state have unique roles in size adaptation in changing environments. In fact, as briefly mentioned in section 1.6, Cln3, Whi5 and Bck2 have all been previously implicated in the cellular response to nutrient changes. The high instability of the Cln3 protein means that for maintenance of its constant concentration during G1, its synthesis must scale with cell size. This continued synthesis makes Cln3 a great candidate for a reporter for global protein synthesis[89,119], which may vary dramatically with environmental changes. One study has already shown that Cln3 is quickly depleted upon a switch from a rich to a poor carbon environment[89]. Cln3 mRNA amounts were also found to be nutrient- and growth-phase-dependent[98]. Whi5 has been shown to record environmental information from the previous cell cycle and accordingly adjust the G1 length in the current cycle[72]. Qu *et al.*[72] found that the amount of Whi5 in the current cell cycle is proportional to the doubling time of the past cell cycle, allowing it to serve as a memory of the cell's growth rate and therefore its environment from the previous cell cycle. Bck2, which is less studied than Whi5 or Cln3, has also been reported to interact with multiple proteins involved in nutrient sensing pathways[80]. For example, Bck2 interacts with Tpd3, the scaffolding subunit of the protein phosphatase PP2A[80]. PP2A is part of the cascade by which TOR and PKA, two nutrient-sensing pathways, regulate cell cycle progression at *Start*[111,118,120] (Fig. 6). Bck2's interactions with proteins involved in nutrient-dependent growth signalling and its ability to regulate the cell cycle indicate that it could potentially link the nutrient state of the environment to the cell cycle progression decision[80]. These results indicate unique roles for G1/S regulators under changing nutrient conditions and raise the question of whether the redundancies in size homeostasis could be disrupted with nutrient switch experiments.

1.9. State-of-the-art analysis of microfluidics-based nutrient switch microscopy experiments

To observe the implementation of size homeostasis at the single cell level, cell size and cell cycle information over multiple time points is required. This is performed using time-lapse or live-cell microscopy, where the same cell is imaged repeatedly as it grows over time. Some of the earliest cell size homeostasis observations were made in a time-lapse microscopy set-up using agar plates and steel mesh grids for relocation of the same cells over multiple time points[50,121]. The repeated acquisition of the photomicrographs and the downstream image analysis were both performed manually[50,121]. Today, cells can be grown and imaged in microfluidic devices which allow much longer imaging and limit colony growth to the focal plane. Microfluidic devices trap cells in transparent cavities and allow exchange of medium through or around these cavities at controlled flow rates, enabling cell growth by providing fresh growth medium and removing waste. These devices can be used under the microscope to automatically image multiple locations of cell growth over several hours[1]. These experiments can generate long videos containing single-cell information of thousands of cells. The bottleneck in live-cell time-lapse microscopy in recent years has been the downstream analysis of these videos[122]. The downstream analysis of biological image data requires cell segmentation, which is the process of detecting individual cells in the image by identifying all the pixels within a cell to create a cellular mask. This is followed by the process of tracking, which connects the same cell between time frames. Cell segmentation and tracking are followed by cell cycle annotation, which comprises assignment of mother-bud connections and cell cycle stages to allow pedigree generation. Before the development of deep-learning approaches, automated cell segmentation, tracking and cell cycle annotations were erroneous and corrections were time and labour-intensive, rendering large parts of the automatically annotated videos unusable. With the recent advances in deep-learning based algorithms, the accuracy and automation of cell segmentation and tracking have greatly improved[122,123], drastically reducing the amount of manual correction required and making more of the image data usable. A state-of-the-art GUI-framework for using deep-learning approaches for image analysis, Cell-ACDC, was developed in the same research group as the one where this project was carried out[122]. Using the YeaZ neural network[123] within the Cell-ACDC framework enabled accelerated segmentation, tracking and cell-cycle annotation in time-lapse microscopy videos and the GUI expedited manual correction of errors. This image-analysis pipeline maximised the number of cell cycles analysed and facilitated the generation of a fully annotated, manually checked dataset of over 13700 complete cell cycles within this doctoral project. Moreover, the microfluidics system enabled automated nutrient switching during time-lapse imaging, allowing observation of the size adaptation response at the single cell level.

Microfluidics-based live-cell microscopy has been widely used for studying steady-state growth of cells in constant growth conditions. However, the use of the technique for investigating cell growth during nutrient switches is not as common and is dominated by studies in the transcriptional memory field using the *GAL* induction network[108,124–127]. Analysis of steady-state growth videos, albeit complex, is still less complex than analysis of nutrient switch videos. In steady-state videos, cells grow exponentially, and key insights can be obtained by grouping and studying all cell cycles, regardless of the time at which they appear in the video. In nutrient switch videos, on the contrary, the temporal position of a cell cycle matters because the history of a cell, particularly its cell cycle stage at the time of the switch, affects how the cell and its offspring adapt to the new environment[108]. This requires a multi-generational tracking of cells and categorisation based on their cell-cycle stage at the time of nutrient switch. The functionalities provided in Cell-ACDC and the embedded neural networks are very useful for overcoming the complexity of single-cell categorisation combined with multi-generational tracking. Taken together, these developments in image analysis provide new opportunities in the study of cell size homeostasis efficiency and how it is affected by changing nutrients and mutations at the single-cell level.

1.10. Aims of this study

Cell size homeostasis is the phenomenon of cell populations of a particular cell type having narrow distributions of cell size, or in other words, having low variance in cell size. Cell size homeostasis is maintained by a coupling of cell growth and cell cycle progression to cell size, indicating that cells are capable of sensing their own size. The major size-sensing mechanism in budding yeast is the size-dependent dilution of the G1/S inhibitor Whi5, also known as the *inhibitor-dilution* model[39]. Whi5 concentration during G1 can predict the rate at which cells pass *Start* but only when accompanied by a simultaneous deletion of the *Start* activator, Bck2[39]. Moreover, perturbation of Whi5 only leads to a partial loss in size homeostasis efficiency[73,78,79]. Together, these two findings indicate that in addition to Whi5, there are more factors regulating *Start* and Bck2 is likely one of them (section 1.5-1.6). One study proposes that Bck2 may in fact regulate *WHI5* mRNA by stimulating Ccr4 to degrade it[106] (section 1.7). This finding, however, has not yet been reproduced in steady state conditions with Whi5 under the control of its endogenous promoter. The first aim of this study, therefore, is to test whether Whi5 is downstream of Bck2 or whether they regulate *Start* independent of each other. This aim also encompasses testing whether *WHI5* mRNA is degraded by Ccr4.

While Whi5 is the only budding yeast size-sensor identified so far, multiple other proteins that can directly or indirectly regulate *Start* have been identified, indicating that size homeostasis at the G1/S transition potentially integrates inputs from a network of proteins. This is in agreement with the observed robustness of the size homeostasis system, as bulk studies have shown that deletions of single *Start* regulators do not affect the efficiency of size homeostasis[73] (section 1.6). Moreover, mutants with deletions of two *Start* regulators, particularly *whi5Δbck2Δ* and *whi5Δcln3Δ* are surprisingly similar to wild-type (WT) cells in size[77]. The second aim of this study, therefore, is to test whether this robustness of size homeostasis to deletions of *Start* regulators can be reproduced at the single-cell level, and how cell cycle properties are affected by these deletions. An important aspect of this aim is to test whether the *whi5Δbck2Δ* double mutant shows loss of size control efficiency despite having an average cell size similar to that of WT. A potential candidate that could help maintain size homeostasis efficiency in the absence of Whi5 could be its paralogue Whi7, which is the major *Start* inhibitor in conditions of cell wall stress (section 1.7). The third aim of this study, therefore, is to test whether Whi7 compensates for Whi5 in the *whi5Δ* mutant. Together, the three aims listed so far would provide insight into roles of specific regulators within the G1/S size homeostasis network and help characterise the interactions between them.

A simultaneous deletion of Bck2 and Cln3 is lethal; one of the two *Start* activators is required to prevent a permanent G1 arrest. This redundancy raises the question of why cells evolved two mechanistically different activators for the same transition. Given the proposed links between Bck2 and Cln3 and nutrient sensing, this study hypothesizes that the two apparently redundant activators may play unique roles under specific conditions, for example, in changing nutrients. The fourth aim of the study, therefore, is to test whether putting the cells through a nutrient switch can reveal unique size phenotypes of the *cln3Δ* and *bck2Δ* strains. So far, cell size homeostasis has largely been studied under steady-state conditions and while these studies have been indispensable for identifying major size regulators, they cannot provide insight into the specific functions these regulators potentially serve in conditions other than steady-state. This study is aimed at not only revealing such condition-specific functions, but also at understanding what happens to size homeostasis when cells enter the lag phase of growth following a nutrient switch.

As part of an additional collaborative project, a parallel aim of this study is to utilise the single molecule fluorescence in-situ hybridisation (smFISH) method to validate an orthogonal single-cell RNA visualisation method: diSpinach tagging[1] (section 3.20).

2. Materials and Methods

2.1. Chemicals and consumables

Table 1: The chemicals and consumables used in this study are listed alphabetically, alongside their source.

Chemical/Consumable	Manufacturer
10X rCutSmart™ Buffer	New England Biolabs, USA
10% Sodium Dodecyl Sulfate Solution	Thermo Fisher Scientific, USA
5X Phusion® HF Buffer	New England Biolabs, USA
5X Q5 High GC Enhancer	New England Biolabs, USA
5X Q5 Reaction Buffer	New England Biolabs, USA
Agarose SERVA Wide Range	Serva Electrophoresis, Germany
Amino acids	Sigma-Aldrich, USA
Ammonium sulfate	Sigma-Aldrich, USA
Ampicillin	Roth, Karlsruhe, Germany
Bacto™ Peptone	Gibco, Thermo Fisher Scientific, USA
Bacto™ Yeast Extract	Gibco, Thermo Fisher Scientific, USA
Coverslips (18 x 18 mm)	VWR International, USA
Coverslips (24 x 50 mm)	Gerhard Menzel GmbH, Germany
DAPI stain	Lab stock
Deoxynucleotide (dNTP) solution mix	New England Biolabs, USA
D(+) Glucose	Sigma-Aldrich, USA
DIFCO™ Granulated Agar	BD, USA
DIFCO™ Yeast Nitrogen Base	BD, USA
D-Sorbitol	Sigma-Aldrich, USA
EDTA disodium salt	Sigma-Aldrich, USA
Ethanol, CH_3CH_2OH	Sigma-Aldrich, USA
Formaldehyde 37% (w/w) in H_2O	VWR International, USA
Formamide, Ultrapure	VWR International, USA
Glycerol	Sigma-Aldrich, USA

Chemical/Consumable	Manufacturer
DNA sodium salt from herring testes	Sigma-Aldrich, USA
Isoton II Diluent	Beckman Coulter, Germany
LB Agar (Lennox)	Sigma-Aldrich, USA
LB Broth (Lennox)	Sigma-Aldrich, USA
LightCycler 480 Multiwell Plate 96	Roche, Switzerland
Lithium acetate dihydrate	Sigma-Aldrich, USA
Microscopy slides	Gerhard Menzel GmbH, Germany
Nourseothricin (clonNAT)	Jena Bioscience GmbH, Germany
Nuclease free water	Qiagen, Germany
Phenol/ Chloroform/ Isoamyl alcohol (25:24:1)	Thermo Fisher Scientific, USA
Phusion polymerase	Lab stock
Poly(ethylene glycol), (PEG), BioXtra	Sigma-Aldrich, USA
Potassium phosphate dibasic, K_2HPO_4	Sigma-Aldrich, USA
ProLong^{TM} Gold Antifade Mountant	Thermo Fisher Scientific, USA
Q5® High-Fidelity DNA Polymerase	New England Biolabs, USA
Sodium hydroxide (pellets)	Thermo Fisher Scientific, USA
SsoAdvanced™ universal SYBR® Green supermix	Bio-Rad, USA
Stellaris® smFISH probes	LGC Biosearch Technologies, UK
Stellaris® RNA FISH hybridization buffer	LGC Biosearch Technologies, UK
Stellaris® RNA FISH wash buffer A	LGC Biosearch Technologies, UK
Stellaris® RNA FISH wash buffer B	LGC Biosearch Technologies, UK
StuI restriction enzyme	New England Biolabs, USA
SuperFrost Plus™ Adhesion slides (25x75x1mm)	Epredia, USA
SYBR™ Safe DNA Gel Stain	Invitrogen, Thermo Fisher Scientific, USA
Tris acetate	Sigma-Aldrich, USA
Tris/HCl solution	Thermo Fisher Scientific, USA
Triton® X 100,	Roth, Germany

Chemical/Consumable	Manufacturer
TriTrack DNA Loading Dye (6X)	Thermo Fisher Scientific, USA
TURBO™ DNase	Invitrogen, Thermo Fisher Scientific, USA
Vectashield® mounting medium	Vector Laboratories, USA
Zymolyase	Zymo Research, USA

2.2. Devices

Table 2: Alphabetical list of devices used for the experiments in this study, alongside their manufacturers.

Device	Manufacturer
Andor iXon Ultra 888 Camera	Oxford Instruments, UK
Bandelin Sonopuls HD 2070 Ultrasonic-Homogenizer	Bandelin electronic GmbH, Germany
Ecotron shaking incubator	Infors HT, Switzerland
Elveflow OB1 Pressure Controller	Elveflow, France
Eppendorf Centrifuge 5910 R	Eppendorf SE, Germany
LightCycler® 96	Roche, Switzerland
Megafuge™ 8 Centrifuge	Thermo Fisher Scientific, USA
Mupid One Electrophoresis System	Nippon Genetics, Germany
NanoDrop OneC	Thermo Fisher Scientific, USA
Nikon Eclipse Ti-E Microscope	Nikon, Japan
Pico™ 17 Microcentrifuge	Thermo Fisher Scientific, USA
Proflex PCR system	Applied Biosystems, Thermo Fisher Scientific, USA
Smart Illuminator (UV)	Eurogentec, Belgium
SPECTRA X Light Engine	Lumencor, USA
U:Genius3 gel imaging system	Syngene, Synoptics Group, UK
Z2 Coulter Particle Count and Size Analyzer	Beckman Coulter, Germany
Zeiss Axiocam 506 camera	Zeiss, Germany
Zeiss LSM 800 microscope	Zeiss, Germany

2.3. Kits

Table 3: List of the molecular biology kits used in this study alongside their manufacturers.

Kit	Manufacturer
High-capacity cDNA Reverse Transcription Kit with RNase Inhibitor	Life Technologies, USA
NucleoSpin Gel and PCR Clean-up	Macherey-Nagel, Germany
NucleoSpin Plasmid	Macherey-Nagel, Germany
YeaStar RNA Kit	Zymo Research, USA

2.4. Strains

The *Saccharomyces cerevisiae* strains used in this work are haploid derivatives of W303, except for the Y7092 strain which is isogenic with BY4741[128] and the IK12 strain, which is based on the Y7092 strain. The complete genotype of W303 is *MATa/MATα {leu2-3,112 trp1-1 can1-100 ura3-1 ade2-1 his3-11,15} [phi*$^+$*]* and of BY4741 is *MATa his3Δ1 leu2Δ0 met15Δ0 ura3Δ0*. A detailed genotypic description of the strains used in this study is available in Table 4.

Table 4: List of strains used in this study and their genotypic descriptions.

Name	Genotype	Source	Description
MMY116-2C	*MATα ADE2*	Lab stock	"WT" in Fig. 7, 8, 10, 11-23, 28-31.
YCY001-1	*MATα ADE2 bck2Δ::CglaTRP1*	This study	*"bck2Δ"* in Fig. 7, 8, 10, 11-23, 28-31.
YCY002-1	*MATα ADE2 ccr4Δ::CglaTRP1*	This study	*"ccr4Δ"* in Fig. 7, 10, 11-13, 15-17.
YCY004-5	*MATα ADE2 whi5Δ::KlacURA3*	This study	*"whi5Δ"* in Fig. 7, 8, 10, 11-23, 28-31.
YCY005-1	*MATα ADE2 bck2Δ::CglaTRP1 whi5Δ::KlacURA3*	This study	*"whi5Δbck2Δ"* in Fig. 7, 10, 11, 13-23, 28, 29, 31.
YCY006-1	*MATα ADE2 ccr4Δ::CglaTRP1 whi5Δ::KlacURA3*	This study	*"whi5Δccr4Δ"* in Fig. 7, 10, 11, 13, 15-17.
YCY024-1	*MATα ADE2 ura3::Act1promoter-WHI5WIQ-mCitrine-URA3 htb2::HTB2-mScarlet-I-natMX6*	This study	"WT" in Fig. 24-27. Strain with Whi5-WIQ tagged with mCitrine and Htb2 tagged with mScarlet-I.
YCY030-2	*MATα ADE2*	This study	*"whi5Δ"* in Fig. 25-27.

Name	Genotype	Source	Description
	ura3::Act1promoter-WHI5WIQ-mCitrine-URA3 *htb2::HTB2-mScarlet-I-natMX6* *whi5Δ::CglaTRP1*		Strain with Whi5-WIQ tagged with mCitrine and Htb2 tagged with mScarlet-I, plus a *WHI5* deletion.
YCY037-1	*MATα ADE2* *ura3::Act1promoter-WHI5WIQ-mCitrine-URA3* *htb2::HTB2-mScarlet-I-natMX6* *bck2Δ::CglaLEU2*	This study	*"bck2Δ"* in Fig. 25-27. Strain with Whi5-WIQ tagged with mCitrine and Htb2 tagged with mScarlet-I, plus a *BCK2* deletion.
YCY038-1	*MATα ADE2* *ura3::Act1promoter-WHI5WIQ-mCitrine-URA3* *htb2::HTB2-mScarlet-I-natMX6* *whi5Δ::CglaTRP1* *bck2Δ::CglaLEU2*	This study	*"whi5Δbck2Δ"* in Fig. 25-27. Strain with Whi5-WIQ tagged with mCitrine and Htb2 tagged with mScarlet-I, plus a *WHI5* and a *BCK2* deletion.
YCY021-2	*MATα ADE2 cln3Δ::CglaLEU2*	This study	*"cln3Δ"* in Fig. 28, 29, 31.
YCY022-2	*MATα ADE2 cln3Δ::CglaLEU2* *whi5Δ::KlacURA3*	This study	*"whi5Δcln3Δ"* in Fig. 28, 29, 31.
YCY023-1	*MATα ADE2 cln3Δ::CglaLEU2* *whi5Δ::KlacURA3* *bck2Δ::CglaTRP1*	This study	*"whi5Δbck2Δcln3Δ"* in Fig. 28, 29, 31.
MK40	*MATa ADE2 cln3::TRP* *ura3::CLN3pr-FLAG-CLN3-URA3*	Mardo Kõivomägi	"WT" in the "MK40 background" in Fig. 30. Strain with the endogenous *CLN3* deleted and a FLAG-tagged *CLN3* inserted in the URA3 locus.
YCY027-1	*MATa ADE2 cln3::TRP* *ura3::CLN3pr-FLAG-CLN3-URA3* *bck2Δ::CglaLEU2*	This study	*"bck2Δ"* in the "MK40 background" in Fig. 30. Strain with the endogenous *CLN3* and *BCK2* deleted and a FLAG-tagged *CLN3* inserted in the URA3 locus.
YCY031-4	*MATa ADE2 cln3::TRP* *ura3::CLN3pr-FLAG-CLN3-URA3* *whi5Δ::natMX6*	This study	*"whi5Δ"* in the "MK40 background" in Fig. 30. Strain with the endogenous *CLN3* and *WHI5* deleted and a FLAG-tagged *CLN3* inserted in the URA3 locus.
JE103	*MATa ADE2*	Jennifer Ewald	"WT" in the "JE103 background" in Fig. 30.
YCY040-1	*MATa ADE2 bck2Δ::CglaLEU2*	This study	*"bck2Δ"* in the "JE103 background" in Fig. 30.

Name	Genotype	Source	Description
			JE103 with a *BCK2* deletion.
YCY039-3	*MATa ADE2 whi5Δ::CglaTRP1*	This study	*"whi5Δ"* in the "JE103 background" in Fig. 30. JE103 with a *WHI5* deletion.
Y7092	*MATα can1Δ::STE2pr-Sp_his5 lyp1Δ*	Boone Lab	WT strain without diSpinach tagging, used in Fig. 32 B, D, E.
IK12	*MATα pRS406 (2µOri-SUT509pr-SUT509-8xdiSPINACH-CYC1term-URA3)*	Igor Kukhtevich	Strain with plasmid containing *SUT509-diSpinach*, used in Fig. 32 A, C.

2.5. Plasmids

Table 5: List of the plasmids used for yeast transformations in this study.

Plasmid name	Description	Source
pPP2960/pFA6a-CglaTRP1	Knockout template with *C. glabrata TRP1* gene	Peter Pryciak
pPP2961/pFA6a-KlacURA3	Knockout template with *K. lactis URA3* gene	Peter Pryciak
pPP3129/pFA6a-CglaLEU2	Knockout template with *C. glabrata LEU2* gene	Peter Pryciak
pCA13	Plasmid with *NATMX6* gene	Lab stock
KSE141	Plasmid with *Act1promoter-WHI5WIQ-mCitrine-URA3*	Kurt Schmoller
pFA6a-mScarletI-NatMX6	Plasmid with *mScarlet-I-NATMX6*	Igor Kukhtevich

2.6. Oligonucleotides

Table 6: List of primers used for RT-qPCRS in this study. All primers were obtained from Sigma Aldrich.

Gene	Direction	Sequence (5'-3')
WHI5	forward	ACAAGACACTTCCCGAGCTG
	reverse	CGCGTCTGCACTATCTGGAA
WHI7	forward	GGTTTCTCCCACAGCGGTTA
	reverse	ACCATTGCGCAGTTGAGTCT
ACT1	forward	AGTTGCCCCAGAAGAACACC

Gene	Direction	Sequence (5’-3’)
	reverse	GGACAAAACGGCTTGGATGG
MDN1	forward	CATCAACAAACCTGACCAACTAATCC
	reverse	CATCAAGGTTTTCCAAAGTGGGC

2.7. Buffers, growth media and plate compositions

Table 7: The composition of the various buffers, growth media and growth plates used in this study. After preparation and autoclaving, all growth media was stored at 4°C.

Buffer/ Growth Medium	Composition
TE buffer	10 mM Tris-HCl 1 mM EDTA, (adjust pH to 8.0)
0.1 M TE/Lithium acetate	0.1 M Lithium acetate 10 mM Tris-HCl 1 mM EDTA
1 M TE/Lithium acetate	1 M Lithium acetate 10 mM Tris/HCl 1 mM EDTA
DNA extraction buffer	2 % (v/v) Triton X 100 1 % (w/v) SDS 100 mM NaCl 10mM Tris-HCl 1mM EDTA
smFISH fixation buffer	1.2 M Sorbitol 0.1 M K_2HPO_4, (adjust to pH 7.5)
TAE buffer	40 mM Tris acetate 1 mM EDTA, (adjust to pH 8.5)
SCD (Synthetic complete medium with 2% glucose)	0.139 % (w/v) Synthetic complete mix 0.17 % (w/v) Yeast nitrogen base 0.5 % (w/v) Ammonium sulfate After autoclaving add: 2 % (w/v) Glucose (sterile-filtered 20% stock) For live cell microscopy: filter medium after adding glucose
SCGE (Synthetic complete medium with 2% glycerol and 1% ethanol)	0.139 % (w/v) Synthetic complete mix 0.17 % (w/v) Yeast nitrogen base 0.5 % (w/v) Ammonium sulfate After autoclaving add: 2 % (v/v) Glycerol (sterile-filtered stock)

Buffer/ Growth Medium	Composition
	1 % (v/v) Ethanol (sterile-filtered stock) For live cell microscopy: filter medium after adding glycerol and ethanol
YPD (Yeast extract peptone medium with 2% glucose)	1 % (w/v) Yeast extract 2 % (w/v) Peptone After autoclaving add: 2 % (w/v) Glucose (sterile-filtered 20% stock)
LB + Ampicillin	2 % (w/v) LB-powder After autoclaving add: 100 µg/mL Ampicillin
SCD plates	x g Synthetic complete/dropout mix as per Table 8. 0.17 % (w/v) Yeast nitrogen base 0.5 % (w/v) Ammonium sulfate 2 % (w/v) Agar 1 pellet NaOH per litre After autoclaving add: 2 % (w/v) Glucose (sterile-filtered 20% stock)
YPD plates	1 % (w/v) Yeast extract 2 % (w/v) Peptone 2 % (w/v) Agar 1 pellet NaOH per litre After autoclaving add: 2 % (w/v) Glucose (sterile-filtered 20% stock)
LB + Ampicillin plates	3.5 % (w/v) LB agar After autoclaving add: 100 µg/mL Ampicillin

Table 8: The amount of synthetic complete dropout mixes added to 1 litre of SC medium to create selective plates, as described in Table 7.

Mix	Amount per litre of SC medium
SC complete	1.385 g
SC-URA	1.365 g
SC-TRP	1.305 g
SC-LEU	1.265 g
SC-HIS	1.365 g

Table 9: The composition of the synthetic complete mix in SC medium. Selective plates were made by skipping single amino acids or nucleotides in the dropout mixture. All components were obtained from Sigma-Aldrich, USA.

Component	Final concentration (w/v)
Adenine hemisulfate salt	0.004%
L-Arginine	0.002%
L-Aspartic acid sodium salt monohydrate	0.01%
L-Glutamic acid potassium salt monohydrate	0.01%
L-Histidine monohydrochloride monohydrate	0.002%
L-Isoleucine	0.003%
L-Leucine	0.012%
L-Lysine monohydrochloride	0.003%
L-Methionine	0.002%
L-Phenylalanine	0.005%
L-Serine	0.0375%
L-Threonine	0.02%
L-Tryptophan	0.008%
L-Tyrosine	0.003%
Uracil	0.002%
L-Valine	0.015%

2.8. Cultivation of *Saccharomyces cerevisiae*

Yeast strains were stored long-term at -80°C in 15% (v/v) glycerol stocks made with SC medium. Before an experiment, the yeast cells from the glycerol stocks were streaked out on YPD plates and incubated at 30°C for one or two days to obtain colonies of cells. The thus obtained cells were inoculated into liquid YPD, SCD or SCGE medium, depending on the type of experiment and incubated at 30°C under shaking conditions (250 rpm). For live-cell microscopy and the bulk nutrient switch experiments, cells were first inoculated into YPD medium and allowed to grow at 30°C under shaking conditions (250 rpm) for 4-5 hours. They were then washed with and inoculated into the target medium (SCD or SCGE). For smFISH experiments, cells were directly inoculated into the target medium from the plates. The specific cell cultivation protocol used for each kind of experiment is described in the dedicated methods section for the experiment.

2.9. Preparation of transforming DNA

All transforming DNA used in this study was amplified from plasmids synthesized in *Escherichia coli* strains. The *E.coli* strains expressing the plasmids were stored long term at -80°C in 25% (v/v) glycerol stocks made with LB medium. When required, these strains were grown overnight in 3 mL LB medium containing 100 µg/mL Ampicillin at 37°C under shaking conditions (250 rpm). The saturated culture was used for plasmid isolation using the NucleoSpin Plasmid Kit and the accompanying protocol for isolation of high-copy DNA from *E.coli*. All the plasmids listed in Table 5 were purified in this manner. For all of the gene deletions performed in this study, the DNA insert from the plasmid that would be used to transform yeast was acquired by PCR-amplification. Primers that would add 60-80 bp overhangs homologous to the target locus in yeast were used for the amplification PCR of the insert. This insert DNA with target-specific homologous ends was used for transformation of yeast. For obtaining the yeast strain containing *Act1promoter-WHI5WIQ-mCitrine-URA3*, the KSE141 plasmid was digested with the StuI restriction enzyme as per the protocol described in Table 10. The restriction digest mixture was incubated at 37°C for one hour and then cleaned using the NucleoSpin Gel and PCR Clean-up kit. The complete digested plasmid was then inserted into the yeast *URA3* locus using the transformation protocol described in section 2.10.

Table 10: The reaction mixture for restriction digestion.

Component	Final Concentration (in Nuclease-free H_2O)
Plasmid DNA	1 µg total
10X CutSmart Buffer	1X
StuI	10 units / µg of DNA

2.10. Transformation of *Saccharomyces cerevisiae*

The yeast strain to be transformed was inoculated into 3 mL YPD medium and was allowed to grow overnight at 30°C to obtain a saturated culture in the morning. 1 mL of this saturated culture was used to inoculate 50 mL of YPD the next morning, which was incubated for 4 to 5 hours at 30°C. 50 mL of cells were centrifuged for 3 minutes at 4000 rpm and 21°C. The cell pellet was washed with 20 mL milliQ water and centrifuged again at the same settings. The supernatant was discarded and the cell pellet was resuspended in 800 µL of 0.1M LiOAc. The cells were centrifuged for 30 seconds at 6000 rpm at room temperature. The supernatant was discarded again and the cells were resuspended in 400 µL 0.1M LiOAc. These cells will now be referred to as competent cells. A receiving tube containing 240 µL 50% PEG, 32 µL 1M LiOAc, 25 µL 2 mg/mL herring sperm DNA and 13 µL transforming DNA was prepared. After vortexing the tube, 50 µL of competent cells were added to it and it was gently vortexed again and incubated at 30°C for 30 minutes. The tubes were then placed at 42°C for 20 minutes before being centrifuged at 6000 rpm for 30 seconds at room temperature. The supernatant was discarded and the cell pellet was resuspended in 400 µL milliQ water by hand vortexing i.e., running the tube across a microtube rack. Up to 300 µL of the resulting suspension was plated on selective plates. If the selective plates contained antibiotics for drug-resistance markers, the cells were first plated on YPD plates and incubated overnight at 30°C. The colonies obtained the next day were replica-plated onto plates containing the appropriate antibiotic. To ensure that colonies thus obtained contained only a single clone, up to five colonies were transferred onto new selective plates using the streak plate method to obtain single colonies again. Genomic DNA was extracted from the thus obtained clones and they were genotyped using confirmation PCRs and Sanger sequencing to test whether the transformation was successful or not.

2.11. Genomic DNA extraction

200 µL of DNA extraction buffer and roughly 0.3 g of acid-washed glass beads were added to a 1.5 mL Eppendorf tube. A generous scoop of yeast cells was transferred from the plate into the tube. Under the fume hood, 200 µL of phenol/chloroform/isoamyl alcohol was added to the tubes and they were vortexed. After waiting 5 minutes, 200 µL of 1X TE buffer was added to the tubes. They were inverted 8 times to mix them and then centrifuged at 13000 rpm for 5 minutes at room temperature. To a new tube, 1 mL of 100% ethanol was added. 300 µL of the aqueous phase from the centrifuged tube was transferred to the tube with 100% ethanol. After being inverted 8 times, this tube was centrifuged at 13000 rpm for 5 minutes at room temperature. The alcohol was poured out and the tube was blotted on a paper towel. 70% ethanol was added to the tube and it was inverted 8 times to mix. The tube was centrifuged again at 13000 rpm for 5 minutes at room temperature and the alcohol was poured off. The DNA pellet was allowed to air dry until all the ethanol evaporated and was then resuspended in 50 µL nuclease-free water. DNA was stored long-term at -20°C.

2.12. Polymerase Chain Reaction (PCR)

Amplification of specific DNA segments was performed using the polymerase chain reaction. Forward and reverse primers specific for the DNA region of interest were used. The reaction mixture was prepared as listed in Table 11. The DNA double strands were first denatured at 98°C for 10 seconds. The primers were allowed to anneal to the DNA for 30 seconds at a temperature based on the melting temperature of the primers, as obtained from the NEB T_m calculator (https://tmcalculator.neb.com/#!/main). Elongation was performed at 72°C and its duration was decided based on the length of the amplicon (roughly 1 minute for every 1000 base pairs). This cycle was repeated 35 times. Either the Phusion or the Q5 polymerase was used for elongation. Amplified DNA was stored at 4°C.

Table 11: Reaction mixture for PCR using Phusion polymerase.

Component	Final Concentration (in milliQ H_2O)
5X High Fidelity Phusion buffer	1X
dNTPs	0.2 mM
Forward primer	0.5 µM
Reverse primer	0.5 µM
Template DNA	variable
Phusion polymerase stock (100X)	1X

Table 12: Reaction mixture for PCR using Q5 polymerase.

Component	Final Concentration (in milliQ H_2O)
5X Q5 reaction buffer	1X
dNTPs	0.2 mM
Forward primer	0.5 µM
Reverse primer	0.5 µM
Template DNA	variable
Q5 High Fidelity DNA polymerase	0.02 U/µl
5X Q5 High GC Enhancer	1X

2.13. Agarose Gel Electrophoresis

1% w/v agarose was dissolved in 1X TAE buffer by heating. SYBR Safe DNA gel stain was added at a final concentration of 0.5X and mixed. The gel was poured into gel trays containing combs and allowed to set for 20 minutes at room temperature. The gel was then placed into the gel apparatus and submerged in 1X TAE buffer. PCR products were mixed with TriTrack DNA loading dye to achieve a final loading dye concentration of 1X. The DNA was then loaded into the gel wells and allowed to run at 100V for 25 minutes. The separated DNA segments were visualised under a UV lamp and imaged with the U:Genius3 gel imaging system.

2.14. RNA extraction

Cells were grown in SCD medium for a minimum of 17 hours to ensure that they were in the exponential phase of growth and OD_{600nm} was maintained below 1. Total RNA was extracted from 1-5 x 10^7 cells per strain using the YeaStar RNA Kit as per the manufacturer's protocol. Turbo DNase enzyme was used to selectively degrade any DNA in the extracted RNA as per the protocol from Thermo Fisher Scientific. RNA quality was checked using agarose gel electrophoresis and its concentration was measured using the NanoDrop spectrophotometer. The RNA was stored at -80°C.

2.15. Reverse transcription quantitative PCR (RT-qPCR)

cDNA was synthesized from 1 µg RNA using random primers and Thermo Fisher Scientific's high capacity cDNA reverse transcription kit. The cDNA was then diluted tenfold using double distilled water. 2 µL of this diluted cDNA was used as a template for quantitative PCR (qPCR) to compare relative mRNA amounts of genes of interest between strains. For each well containing 2 µL of diluted cDNA, specific primers for *WHI5*, *WHI7*, *MDN1* or *ACT1* were added at a final concentration of 0.5 µM alongside BioRad's SsoAdvanced Universal SYBR Green Supermix. The total reaction volume per well was made up to 10 µL using nuclease free water. The 96-well LightCycler plates were placed in the LightCycler 96 device and run as per the qPCR set-up described in Table 13.

Table 13: qPCR set-up.

Reaction step	Temperature (°C)	Time (s)	Cycles
Pre-incubation/ Polymerase activation	95	30	1
Denaturation	95	10	40
Annealing/Extension	60	30	
Melting	95	60	1

Each biological replicate consisted of an independent RNA extraction. For each biological replicate, C_q values from at least three and up to six wells were averaged to get a mean C_q value. The mean C_q value of the reference gene, which in this case was *ACT1*, was subtracted from the mean C_q value of the gene of interest to obtain the ΔC_q value. The ΔC_q of WT cells was then subtracted from

ΔC_q of the various strains to obtain the $\Delta\Delta C_q$ value for the strains. The relative mRNA concentration for the gene of interest in the strain of interest was calculated using the formula:

$$\text{relative mRNA concentration} = 2^{-(\Delta\Delta Cq)}$$

The relative mRNA concentrations of *WHI5* and *WHI7* obtained in this manner from five biological replicates are plotted as a box plot in Figure. 11 in the Results section. As quality control for the RT-qPCR experiments, the relative mRNA concentration of the housekeeping gene *MDN1* is also plotted for the different strains (Fig. 7). Like *ACT1*, *MDN1* expression is also known to scale with cell size[78,129] and is therefore expected to be constant across different strains. This is in agreement with the observation of WT-like *MDN1* expression levels in all observed strains (Fig. 7).

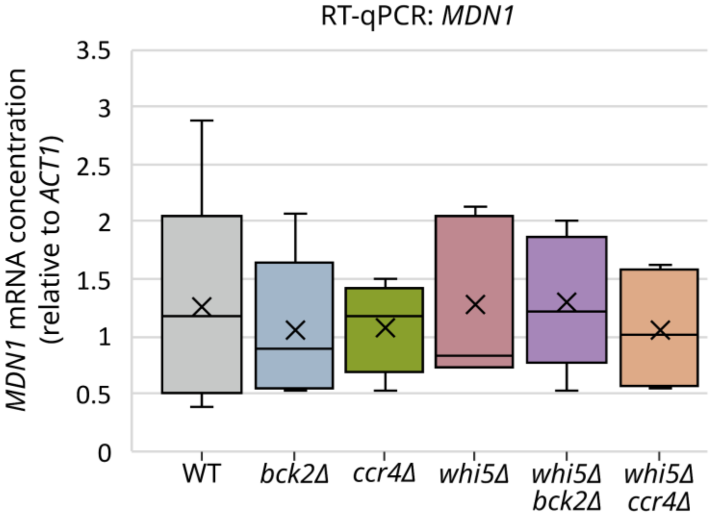

Figure 7: Constant relative mRNA concentrations of *MDN1* across different strains serves as a quality control test for RT-qPCR experiments. The expression of the housekeeping gene *MDN1* relative to *ACT1* is plotted for cells of different strains growing in SCD. The relative mRNA concentration of *MDN1* is observed to be constant across different strains, which is expected as *MDN1* expression scales with cell size, similar to *ACT1*[78,129]. This serves as quality control for the RT-qPCR experiments performed in this study. Each boxplot is based on data from a minimum of four biological replicates (independent RNA extractions). Independent, two-tailed t-tests assuming unequal variances (Welch's t-tests) were used for the statistical comparison of WT to each deletion strain. All p-values were greater than 0.5, indicating that the differences between the deletion strains and WT are non-significant.

2.16. Single molecule fluorescence in situ hybridisation (smFISH):

2.16.1. Sample preparation

Single molecule fluorescence in situ hybridisation was performed using sequence-specific Stellaris® probes and the accompanying protocol for *Saccharomyces cerevisiae* (www.biosearchtech.com/stellarisprotocols) from Biosearch Technologies. For *WHI5* mRNA, the Stellaris® probes contained 37 oligonucleotides, each 18 nucleotides in length and tagged with the Quasar-570® fluorophore. For *SUT509* mRNA, 40 Stellaris® oligos that were 20 nucleotides long and labelled with the Quasar-570® fluorophore were used. Stellaris® probes for *ENO2* mRNA were obtained from our collaborators[1] and consisted of 48 oligonucleotides labelled with the Quasar-670®

fluorophore. For *BCK2* mRNA (Fig. 8), 48 oligonucleotides, each 20 nucleotides in length and tagged with the Quasar-670® fluorophore, were used. Cells were inoculated into 5 mL SCD for *WHI5* and *SUT509* smFISH and into 5 mL SCGE for *ENO2* smFISH. These cultures were incubated at 30°C under shaking conditions (250 rpm) for a minimum of 5 hours. The cells were then diluted into 50 mL medium at an appropriate OD_{600nm} that would allow them to grow overnight and not exceed OD_{600nm} 1 until the next morning. These cultures were incubated overnight at 30°C under shaking conditions (250 rpm). For *BCK2* smFISH (Fig. 8), the cells were inoculated into YPD and allowed to grow at 30°C under shaking conditions (250 rpm) for 4-5 hours before being washed and inoculated into 50 mL of SCD or SCGE at an OD_{600nm} that would allow them to grow overnight and not exceed OD_{600nm} 1 until the next morning. These 50 mL cultures were incubated overnight at 30°C under shaking conditions (250 rpm). The next morning, for all the different smFISH experiments, 45 mL of cells in the OD_{600nm} range 0.1-0.4 were fixed with 5 mL 37% formaldehyde to achieve a final concentration of 3.7% formaldehyde. This fixation was allowed to progress at room temperature for 45 minutes. The cells were then centrifuged at 1600 g for a duration of 4 minutes. The supernatant was discarded and cells were washed twice with ice-cold smFISH fixation buffer (1.2 M sorbitol, 0.1 M K_2HPO_4, pH 7.5). The cells were treated with 1 mL of fixation buffer containing 6.25 µg Zymolyase at 30°C for 55 minutes. The cells were washed two more times with ice-cold fixation buffer, but the centrifugation was performed at a much lower speed (400 g for 6 minutes) to avoid cell deformation and bursting after cell wall digestion with Zymolyase. The cells were resuspended in 70% ethanol and stored minimum overnight or for up to one week at 4°C. Depending on the size of the cell pellet on the previous day, 300-500 µL of cells in 70% ethanol were centrifuged at 400 g for 5 minutes. The cell pellet was resuspended in 100 µL of Stellaris® RNA FISH Hybridisation Buffer which contained 10% v/v formamide and Stellaris® FISH probes at a final concentration of 125 nM. To allow the cells to hybridise to the probes in the dark, the tubes were covered in aluminium foil and placed overnight at 30°C. The next morning, 100 µL of Stellaris® RNA FISH Wash Buffer A containing 10% v/v formamide was added to the cells and they were centrifuged at 400 g for 5 minutes. The cell pellet was washed again with the Wash Buffer A-formamide solution and incubated at 30°C in the dark for 30 minutes. The cells were centrifuged and the cell pellet resuspended in 1 ml of Wash Buffer A-formamide solution containing 5 ng/mL DAPI stain. The cells were incubated in the dark at 30°C for 30 minutes to allow DAPI staining of the nuclei. They were then centrifuged (400 g, 5 minutes) and resuspended in the Stellaris® RNA FISH Wash Buffer B and washed by shaking at 500 rpm for 12 minutes. The tubes were centrifuged again (400 g, 5 minutes) and the cell pellet was resuspended in 20-50 µL of either Vectashield® or ProLong Gold mounting media, depending on availability. 5-10 µL of cells in the mounting medium were pipetted onto clean glass sides and covered with a cover slip. A clean tissue was used to gently press down the cover slip and absorb excess mounting medium from around its edges. The cover slip was fixed to the slide using small strips of tape around all its edges.

2.16.2. Imaging

The smFISH slides were imaged either on the day of preparation or stored in the dark at room temperature and imaged in the next three to four days. They were imaged using a 63x/1.4 NA oil immersion objective and an Axiocam 506 camera on a Zeiss LSM 800 microscope. 20-25 multi-channel Z-slices were acquired at 240 nm intervals per imaging position using the Zen 2.3 software. The cells were imaged in bright field by using a TL LED at an exposure time of 100-140 ms at 6% of the maximum intensity. The FISH probes containing the Quasar-570® fluorophore were imaged using a 530 nm LED with a 5 second exposure time at 50% of maximum intensity. The FISH probes containing the Quasar-670® fluorophore were imaged using a 630 nm LED with a 400 millisecond exposure time at 50% of maximum intensity. The DAPI-stained nuclei were imaged using a 385 nm LED at an exposure time of 130 milliseconds at 30% of the maximum intensity.

2.16.3. Data analysis:

2.16.3.1. SpotMAX development

Some of the smFISH data generated in this work was used for the development and benchmarking of SpotMAX[130], an AI-driven framework that automates spot detection as well as spot quantification. Spot analysis is a commonly performed task in microscopy-based research in cell biology. Despite the widespread need for spot-analysis, there was a lack of a gold standard tool that could not only detect spots but also quantify spot features such as size or intensity in multidimensional data. This lack of a tool that catered to specific biological questions or data types often meant that researchers would have to manually annotate spots, which is time-consuming and subjective. SpotMAX was developed to fill this niche and serve as a generalist standard framework that can integrate various AI workflows while providing a user-friendly interface for in-depth spot characterisation on datasets with up to 5 dimensions (x, y, z, time, channels).

Structurally, SpotMAX consists of four modules. The first and second modules perform semantic segmentation of the reference channel and the spot channel, respectively. This segmentation can either be performed using automatic thresholding or any of the models available in the BioImage.IO model zoo (https://bioimage.io/#/about). Additionally, SpotMAX AI, which consists of neural networks specifically trained for spot segmentation, can be used in the second module. The 3D smFISH data generated in this thesis for the collaboration with Kukhtevich *et al*.[1] was also used in the training of SpotMAX AI. The third SpotMAX module performs spot detection using local peak detection in the spot masks obtained from the second module, which is also where the software gets its name from:

‘spot’ detection by local ‘MAX’ search. The fourth module calculates spot features such as spot size and intensity metrics. The spots can also be validated based on user-selected filters.

The benchmarking of SpotMAX against other state-of-the-art tools required a ground truth dataset. Since the field lacked a high-quality 3D ground truth dataset for spot detection, the SpotMAX team asked expert annotators to annotate spot centres in 3D data. The author of this thesis also contributed to the annotation of this ground truth dataset and provided 3D smFISH images for the same. Since part of this dataset was used for the training of the SpotMAX AI model, only automatic thresholding was used in SpotMAX during benchmarking. Extensive benchmarking revealed that SpotMAX performed better than other state-of-the-art tools as well as non-expert human annotators. In specific cases, it also outperformed expert human annotators. This high precision and modularity of SpotMAX make it a versatile and user-friendly medium for reproducible, standardised spot analysis.

2.16.3.2. Spot detection and validation settings for smFISH spots of *WHI5* mRNA

Cell segmentation masks and cell cycle annotations were generated and corrected in Cell-ACDC and imported into SpotMAX. The smFISH fluorescence spots were counted using the spot detection module in SpotMAX. Spot detection and filtration settings for *WHI5* mRNA spots were adjusted for every replicate in every strain but were in the following range of values. A sigma in the range of 0.3 to 2 voxels was used for the 3D Gaussian filter. Instance segmentation of the spot signal was performed using the ‘threshold_triangle’ automatic thresholding algorithm. Peaks were filtered based on effect size using the ‘effsize_glass_s’ filter. The effect size lower threshold was in the range of 1 to 2.1. Valid spots were determined by an additional filter for spot size with the lower limit ranging between 1.6 to 2 pixels and the upper limit between 4 to 20 pixels.

2.16.3.3. Spot detection and validation settings for smFISH spots of *ENO2* and *SUT509* mRNA

Like for *WHI5* smFISH, cell segmentation and cell cycle annotations were performed in Cell-ACDC and the masks and pedigrees were imported into SpotMAX. A 3D Gaussian filter with a sigma of 0.75 voxels was applied and followed by the application of a ‘Difference of Gaussians’ filter. ENO2 spots were filtered using the ‘Yen’ thresholding algorithm and SUT509 spots using the ‘Triangle’ thresholding algorithm. Overlapping spots and spots with a mean signal lower than that of the cellular background were also discarded from the analysis. For *SUT509* smFISH, approximately 9% of cells were saturated with the signal from smFISH probes and were therefore also excluded from the analysis.

2.16.3.4. Spot detection and validation settings for smFISH spots of *BCK2* mRNA

Cell segmentation and cell cycle annotations were performed in Cell-ACDC and the masks and pedigrees were imported into SpotMAX. A 3D Gaussian filter with a sigma of 0.75 voxels was applied. The spots were filtered using the ‘Triangle’ thresholding algorithm. Peaks were filtered based on effect size using the ‘effsize_glass_s’ filter. The effect size lower threshold was 1.8. Valid spots were determined by an additional filter for spot size in the range of 2.10 to 10.5 pixels. The settings were constant for all strains and in both growth media.

2.16.3.5. Calculation of spot concentrations and further categorisation based on the cell cycle stage

The initial cell cycle annotations performed in Cell-ACDC categorised cells into G1 if they were unbudded, and S/G2/M if they were budded. After spot detection, S/G2/M cells were further categorised into S or G2/M phase based on the ratio of bud volume to mother volume. In the *WHI5* smFISH experiments, if the bud volume-to-mother volume ratio was lower than 0.3, cells were categorised into S phase. If it was greater than or equal to 0.3, cells were categorised into G2/M phase. In the *SUT509* and *ENO2* smFISH experiments, this ratio threshold was set at 0.2. Spot concentrations were calculated for every cell by dividing the number of spots detected per cell by the cell volume (fL).

2.16.4. Quality control for smFISH

WHI5 smFISH results from this study reproduced the average of 1-2 *WHI5* mRNA per cell previously observed in literature[72,78]. Additionally, *WHI5* mRNA expression was found to be size independent in WT and *bck2Δ* cells (Fig. 8), i.e., was constant in cells of different sizes, with the slope of the regression line being close to 0. This was also in agreement with previous studies[78]. As a negative control, *WHI5* expression in *whi5Δ* cells was studied and these cells were found to have 0.07-0.09 *WHI5* mRNA spots on average (Fig. 8, Fig. 12). As a positive control for size-dependent expression, smFISH was also performed on *BCK2* mRNA in two media: SCD and SCGE (Fig. 8). Unlike *WHI5*, *BCK2* expression scaled with cell size, i.e., bigger cells had more *BCK2* mRNA in both SCD and SCGE (Fig. 8). The slopes of the regression lines were around 0.03 in SCD and 0.02 in SCGE. As negative controls for *BCK2* smFISH, *bck2Δ* cells showed a negligible number of RNA spots (Fig. 8). Taken together, these control experiments and consistencies with literature ensured the quality of the smFISH pipeline used in this study.

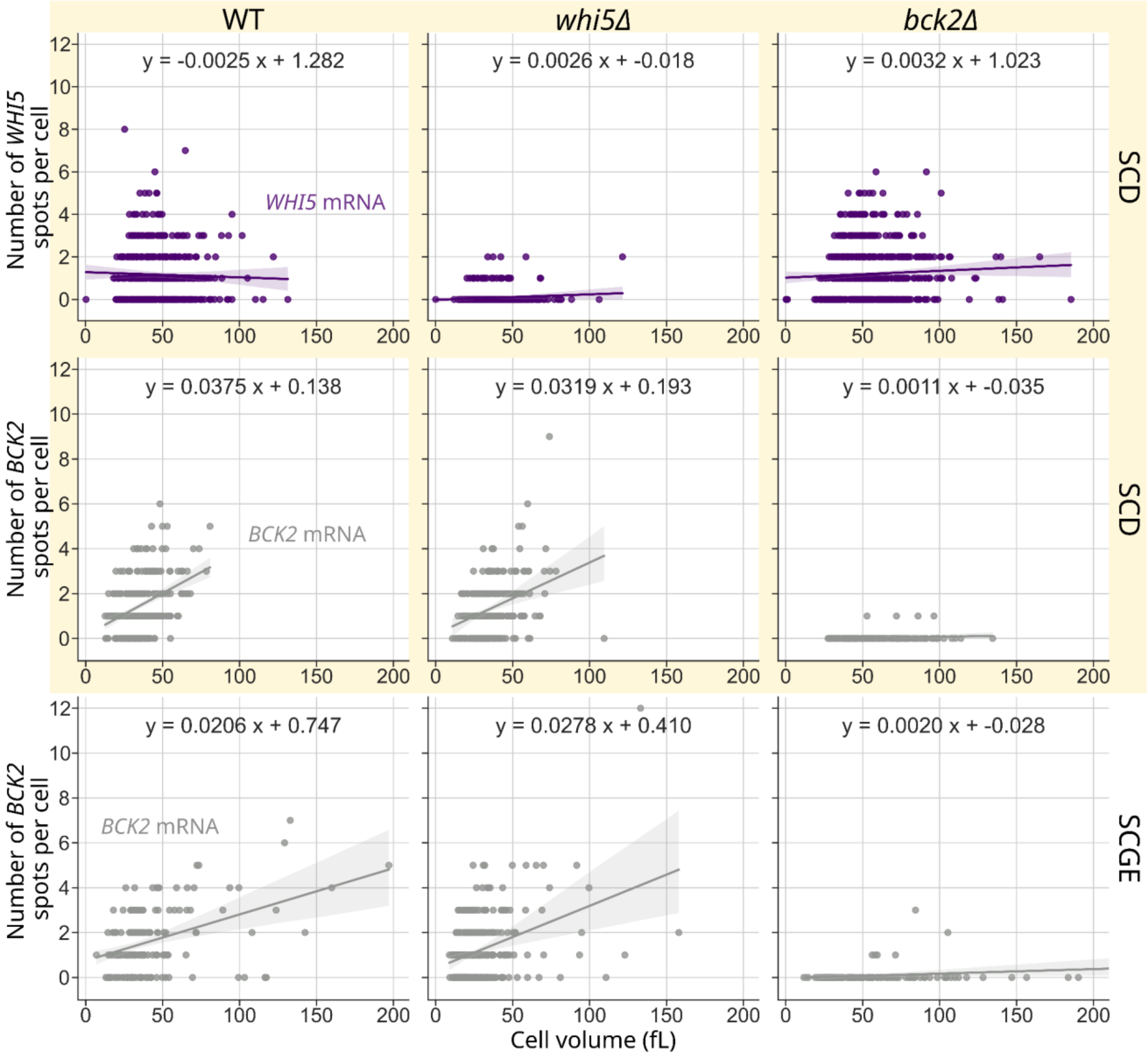

Figure 8: In agreement with previous studies, *WHI5* expression is size-independent and *BCK2* expression is size-dependent. The number of mRNA spots per cell, as observed through smFISH, are plotted against cell volume (fL) for *WHI5* mRNA (purple, top row) and *BCK2* mRNA (grey, bottom two rows). The three columns show these results for three different strains (L-R): WT, *whi5Δ* and *bck2Δ*. Cells in the top two rows (yellow shaded area) were grown in SCD and those in the last row were grown in SCGE. The equations for the regression lines are printed in each panel. Shaded areas around the regression lines show 95% confidence intervals. The number of *WHI5* spots per cell was constant for cells of varying sizes, indicating size-independent expression (top row, WT and *bck2Δ*). On the contrary, the number of *BCK2* spots per cell increased with cell size, indicating size-dependent expression (bottom two rows, WT and *whi5Δ*). Appropriate negative controls (*whi5Δ* for *WHI5* smFISH and *bck2Δ* for *BCK2* smFISH) showed an average number of spots per cell close to 0. The data for *WHI5* smFISH (top row) is pooled from two independent experimental replicates. The data for *BCK2* smFISH (bottom two rows) consists of one replicate each in two different growth media. To maintain consistency and comparability in x-axes limits among all the panels in the figure, the x-axis in the *bck2Δ* SCGE panel (bottom right corner) has been cut short to exclude some outlier cells.

2.17. Bulk nutrient switch experiments using the Coulter-counter

WT and *whi5Δbck2Δ* cells were inoculated into 3 mL YPD medium and incubated at 30°C under shaking conditions (250 rpm) for a minimum duration of 4 hours. 1 mL of this culture was centrifuged at 4000 rpm for 1 minute at room temperature. The supernatant was discarded and cells were resuspended in 1 mL SCD medium. The cells were centrifuged once more at the same settings and resuspended into 1 mL of SCD medium. The washed cells were inoculated into 50 mL of SCD medium at a starting OD_{600nm} of 0.0001. These cultures were allowed to grow overnight at 30°C under shaking conditions (250 rpm). After a minimum of 17 hours of growth to ensure that cells were growing exponentially in SCD medium, cells were washed with SCGE medium and inoculated into 50 mL of SCGE medium at a starting OD_{600nm} of 0.01. The cultures were incubated at 30°C under shaking conditions (250 rpm). The time point of this inoculation was called the time at which the nutrient-switch was performed. Starting from this time point of inoculation and up until 28.5 hours later, Coulter-counter and OD_{600nm} measurements were performed at 1-1.5 hour intervals. Two additional measurements were performed at 48 and 72 hours after the nutrient switch respectively. Because these cultures were started at an OD_{600nm} of 0.01, even as the cells grew, the OD_{600nm} remained below 1 for the first 30 hours. For the two measurements at 48 and 72 hours after the nutrient switch, the OD_{600nm} was maintained below 1 through appropriate dilutions of the cultures after they reached OD_{600nm} 0.1. The complete time course of observations was achieved through three independent experiments of two replicates each, which is why some of the overlapping time points have four data points while others have only two. The CV was calculated from the Coulter-counter dataset at every time point using the following formula:

Coefficient of Variation (CV) of cell volume = Standard deviation in cell volume / Mean cell volume

A statistical comparison between the two strains over the various time points was performed using the mixed ANOVA test. The time course was divided into three ten-hour intervals and the remaining two timepoints were grouped together (Fig. 18). A mixed ANOVA test was performed for each time interval with time as the ‘within-subjects’ factor and strain as the ‘between-subjects’ factor. Since both the factors did not interact significantly with each other, the effects of each factor could be safely interpreted independently. The p-values for the between-subjects factor, the strain, were used for statistical annotations in Figure 18.

2.18. Live-cell microscopy:

2.18.1. Culture conditions

Yeast cells were grown in 3 mL of YPD medium for a minimum of 5 hours at 30°C under shaking conditions (250 rpm). 1 mL of the culture was then centrifuged at 4000 rpm for 1 minute at room temperature and resuspended in either SCD or SCGE medium. The cells were centrifuged at the same settings again and resuspended in the same growth medium as the last step. These washed cells were inoculated into 50 mL of the growth medium that they were washed with at a low starting OD_{600nm}. The starting OD_{600nm} was calculated in a manner to allow the cells to grow for at least 16 hours without crossing OD_{600nm} 1. After a minimum of 16 hours of growth at 30°C under shaking conditions (250 rpm), cells were diluted to OD_{600nm} 0.1, sonicated at 10% power for 4 seconds and stored on ice before being loaded into the microfluidic device for live cell microscopy.

2.18.2. The live-cell microscopy set-up

For live-cell microscopy, a Nikon Eclipse Ti-E microscope was used in combination with a custom microfluidic device which is described extensively in the work from Kukhtevich *et al.*[1]. A master mould for the microfluidic device was created using photolithography and then polydimethylsiloxane (PDMS) was poured into the mould along with a curing agent and allowed to crosslink. The resulting replica of the master mould in PDMS was separated from the master mould and inlets and outlets for tubings were punched into this replica. The replica was then sealed with a coverslip and connected via tubings to the flow controller, before being fixed in the microscopy set-up.

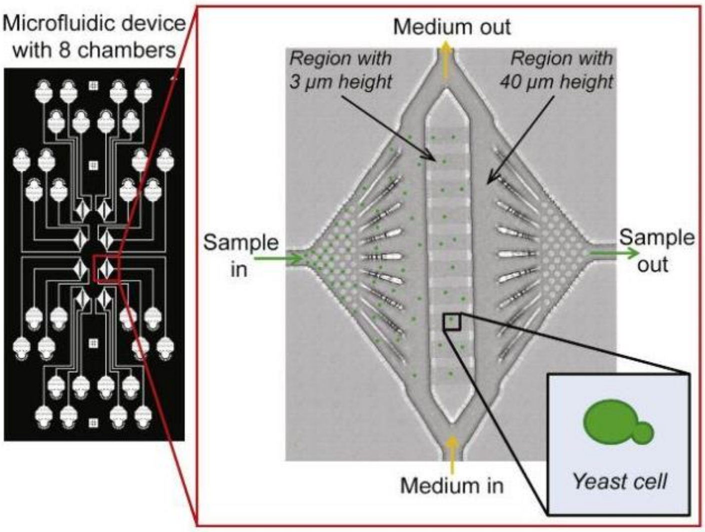

Figure 9: Illustration of the microfluidic device taken from Kukhtevich *et al.*[1]. The eight diamond-shaped structures in the centre of the microfluidic device in the illustration on the left are the cell culture chambers. Lines show channels connecting each of these chambers to an individual media inlet, media outlet, sample inlet and sample outlet port. The red square shows a magnified image of a single cell culture chamber. Yellow arrows show the media inlet and outlet channels and green arrows show the sample inlet and outlet channels. The height in the central region of the cell culture chamber is only 3 µm, allowing cells to be trapped in this region. The surrounding region has a contrasting height of 40 µm.

The resulting microfluidic device consisted of eight cell culture chambers which could be used for simultaneously imaging cells from eight different strains (Fig. 9). The central region of the chambers was only 3 μm in height and could therefore trap yeast cells and force them to grow in the XY focal plane of the microscope. The tubing connections to the flow controller allowed entry of fresh medium into the chamber at customisable flow rates. The tubing connections also enabled the exit of waste medium from the chambers. The channels of medium flow surrounded the chambers of cell growth and the actual exchange of medium occurred through diffusion, minimising disturbance to the cells and allowing for very stable imaging within the chamber. Incubation temperature of the cells in the microfluidic device was maintained at 30°C during the experiment through an objective heater and a custom heatable insertion.

The flow controller used in this set-up was connected to filtered SCD or SCGE media during steady state experiments and to both media during nutrient switch experiments. The medium was pumped at a constant rate of 20 μL/minute through the microfluidic set-up. For steady state experiments, the same growth medium was pumped through the device for the entirety of the experiment. For nutrient switch experiments, SCD was used for the first two hours of the experiment and SCGE was used for the next 25 hours of the experiment. The flow controller could be programmed to automatically switch the medium at the planned time point of the nutrient switch. The time taken for a complete change of media in the microfluidic system and device after the nutrient switch in the controller was calculated to be roughly 30 minutes.

The epifluorescence microscopy set-up that was used for the imaging of live cells in the microfluidic device consisted of the Nikon Eclipse Ti-E microscope along with the NIS-Elements software, the SPECTRA X light engine for illumination and the Andor iXon Ultra 888 camera. During live cell imaging, phase contrast and fluorescence images were acquired at intervals of 3 minutes through a plan-apo λ 100×/1.45 Na Ph3 oil immersion objective. An additional magnification of 1.5x was applied. For the phase contrast channel, images were acquired with an exposure time of 100 ms. For the mScarlet-I fluorescence channel, an exposure time of 200 ms was used to illuminate with the SPECTRA X light engine at 555 nm and 10% power (26 mW). For the mCitrine channel, exposure time was 300 ms and illumination was performed at 508 nm at 40% power (24.8 mW). These imaging settings were consistent across all live-cell imaging experiments in this thesis.

To maximise the number of cell cycles imaged before the cells crowded the field of view, only imaging positions with 1 or 2 cells at the start of the experiment were selected. This meant that at the time of the nutrient switch, most positions had only undergone one doubling and had 2 to 4 cells. While this enabled the collection of data from multiple generations after the nutrient switch, it reduced cell numbers in the populations that faced the switch. Repeated categorisation of these populations for the downstream analysis of the nutrient switch led to the low numbers of cells observed in some cell categories. Wherever possible, more replicates of the live-cell imaging experiments were performed to strengthen the cell numbers.

2.18.3. Data analysis for live-cell microscopy

The ‘videos’ of cell growth generated from live-cell microscopy were analysed using the open-source image analysis software, Cell-ACDC[122]. In the data preparation module of Cell-ACDC, the images from different frames of a single position were aligned to correct for minor movements in the microscopy set-up. They were also cropped to a region of interest to avoid loss of time due to unnecessary segmentation. Automated cell segmentation and cell tracking were performed using the YeaZ[123] neural network within the Cell-ACDC framework. The generated cell masks and bud-mother annotations were manually corrected in the Cell-ACDC GUI. The most common error in the segmentation was a failure of the neural network to detect very small buds, which, if left uncorrected, would bias the dataset towards longer G1 and shorter S/G2/M phases. Additionally, manual annotation was key for identification and labelling of dead cells. This manually corrected dataset could be exported with a wide range of cell-mask- and fluorescence-intensity-associated metrics calculated by Cell-ACDC for downstream analysis.

2.18.3.1. Calculation of cell volume metrics

For Figure 13 and Figure 15, mean cell volumes and CVs of cell volume were calculated from live-cell imaging data. To obtain a mean cell volume that was representative of the cell sizes in the population, cell numbers were maximised by pooling together all cells in the last frame of every imaging position. The mean cell volume and CV of cell volume were calculated from this pooled population after the exclusion of dead cells. For the CV of cell volume in Figure 15, the heights of the bar plot are the values of CV obtained from the pooled data. The •, ■, and x symbols denote values of the CV of cell volume obtained if the pooled data is split based on the two underlying experimental replicates. For statistical comparison of the CVs of cell volume between strains, bootstrapping was performed for a random resampling of positions from each strain in 10,000 iterations with replacement. For the combination of positions obtained in every iteration, the CV of cell volume was calculated on cells pooled from the last frame of each position. The vector of the resulting CV distributions of one strain was subtracted from the vector of the CV distributions of the other to generate a difference vector. The 95%, 99% and 99.9% confidence intervals were calculated for this difference vector. If a given confidence interval contained 0, the CV distributions of the two strains were interpreted to overlap at the given confidence level, indicating that the strains were not significantly different.

2.18.3.2. Quantification of cell cycle properties

The Cell-ACDC output data already contained cell cycle stage-based categorisation. The cell cycle annotations of buds to mothers automatically assigned both buds and mothers to the S/G2/M phase and unbudded cells to the G1 phase of the cell cycle. For this thesis, the Cell-ACDC output data was analysed in Jupyter Notebook using multiple functions from the Cell-ACDC downstream analysis notebook, such as cca_functions.calculate_downstream_data, cca_functions.calculate_per_phase_quantities and cca_functions.calculate_relatives_data. These functions were useful for calculating cell cycle properties such as phase lengths, volume changes per phase and for retrieving relatives' data for each cell (Fig. 14). Additional properties such as growth rates, cell volumes at specific points in the cell cycle and mother-bud pedigrees could then be obtained based on these initial calculations. All cell cycles were labelled as complete or incomplete. Incomplete cell cycles were cell cycles during which the cell died or which were interrupted by the start or the end of the experiment. Unless otherwise specified, only complete cell cycles were used for the analyses in this work.

To confirm that cells in the steady state live cell microscopy experiment were indeed growing exponentially during the experiment, the average cell cycle durations during the experiment were compared with the known exponential phase doubling times obtained from bulk experiments in literature[131]. The cell cycle duration is the time taken for one complete cell cycle from birth until division and should be correlated with the doubling time of population. Bulk measurements show

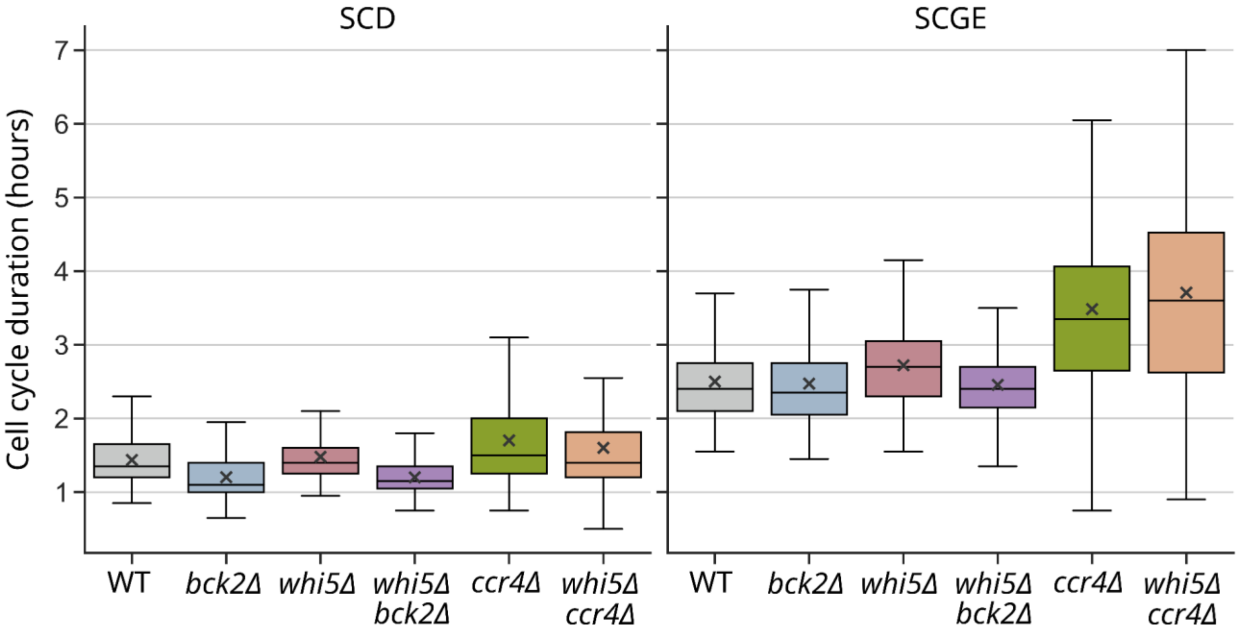

Figure 10: Cell cycle durations in live-cell microscopy in SCD and SCGE media are correlated with doubling times obtained from bulk experiments in literature. The cell cycle durations (hours) of complete cell cycles pooled from two independent experimental replicates each of live cell microscopy in SCD (left) and SCGE (right) are plotted as boxplots for the different strains of interest. WT cells and the *bck2Δ*, *whi5Δ* and

whi5Δbck2Δ appear to be growing with the expected cell cycle duration of roughly 1.5 hours in SCD and 2.5 hours in SCGE, which indicates exponential growth. Cells belonging to *ccr4Δ* and *whi5Δccr4Δ* strains have slightly longer cell cycle durations in SCD, but are much more delayed in completing their cell cycles in SCGE. Due to this elongated cell cycle duration and increased cell death observed in these strains, *ccr4Δ* and *whi5Δccr4Δ* cells growing in SCGE were excluded from analysis in this study.

that for cells growing exponentially in SCD, the doubling time is roughly 1.5 hours and for cells growing exponentially in SCGE, it is roughly 2.5 hours[131]. To mimic a bulk measurement, all complete cell cycles from the live-cell microscopy experiment were pooled and their cell cycle durations (in hours) are plotted in Figure 10. This data represents two independent replicates in each growth medium. WT cells appear to be growing with the minimum cell cycle duration during the course of the experiment, which is around 1.5 hours for SCD and 2.5 hours for SCGE (Fig. 10). This indicates that they are likely in the exponential phase of growth during the experiment. Except for the *ccr4Δ* and *whi5Δccr4Δ* strains, the deletion strains appear to have cell cycle durations similar to those of WT. In SCD, *ccr4Δ* and *whi5Δccr4Δ* cells take around half an hour longer than WT, but in SCGE, these delays are exaggerated, with these strains needing almost an hour more to complete their cell cycles (Fig. 10). Due to this slow growth and an increased frequency of cell deaths, *ccr4Δ* and *whi5Δccr4Δ* cells in SCGE were excluded from the analysis.

2.18.3.3. Further cell cycle categorisation based on fluorescence reporters

As shown in Figure 24 in Results, fluorescent cell cycle markers were used to resolve the specific cell cycle stage of a cell. Using Cell-ACDC's segmentation module, nuclear masks were obtained from the fluorescently labelled histone Htb2 signal by using simple thresholding. Upon subtraction of these nuclear masks from the cell masks generated by the YeaZ neural network, masks for the cytoplasm were obtained, allowing fluorescence analysis to be performed in three separate compartments: the whole cell, the nucleus and the cytoplasm. The fluorescence metrics in the Cell-ACDC output data were obtained for all three kinds of masks for two different cell cycle reporters: Whi5-WIQ-mCitrine and Htb2-mScarlet-I. Comparison of the signals from these two reporters between cell compartments allowed further resolution of the cell's current cell cycle stage.

The mean pixel intensity is the sum of all pixel intensities in a mask divided by the mask area in pixels. Mothers and buds, however, are classified as individual cells in the Cell-ACDC output. To obtain the mean pixel intensity for the combined mother-bud system, pixel intensities of all the pixels in the mother and bud masks were summed and divided by the sum of the number of pixels in the mother and bud masks. The cytoplasm-adjusted mean pixel intensity, for example for Whi5-WIQ-mCitrine in Figure 24, was calculated by subtracting the mean pixel intensity of the cytoplasm mask from the mean pixel intensity of the nuclear mask. This adjustment helped correct for

autofluorescence within the cell. Htb2-mScarlet-I amount was background adjusted within Cell-ACDC by the manual definition of a ‘background region’ in the data preparation module.
For identifying the frame at which *Start* occurs in G1, cytoplasm-adjusted nuclear mean pixel intensity of Whi5-WIQ-mCitrine was plotted against time in frames for each cell in the cell category of interest. The frame at which the nuclear mean pixel intensity of Whi5-WIQ-mCitrine started decreasing in G1 was identified manually and labelled as ‘Whi5_export_start_frame’. Similarly, the frame at which nuclear mean pixel intensity of Whi5-WIQ-mCitrine stopped decreasing was identified manually as the ‘Whi5_export_end_frame’. For both of these frames, the nuclear mean pixel intensity of Whi5-WIQ-mCitrine was acquired (Whi5_intensity_export_start, Whi5_intensity_export_end). The difference between the two intensities was calculated and divided by 2. This value was added to the Whi5_intensity_export_end to ascertain the nuclear mean pixel intensity when 50% of Whi5 had been exported from the nucleus (Whi5_intensity_50%_export). After calculating the Whi5_intensity_50%_export, the nuclear mean pixel intensity of Whi5-WIQ-mCitrine at every G1 frame starting from Whi5_export_start_frame was compared to this value. The earliest frame at which the nuclear mean pixel intensity of Whi5-WIQ-mCitrine was lower than that Whi5_intensity_50%_export was assigned as the first post-*Start* frame. All G1 frames after this frame were assigned to the post-*Start* category and all G1 frames before this frame were assigned to the pre-*Start* category.

The nuclear mean pixel intensity of Whi5-WIQ-mCitrine was also used to identify the first frame of telophase in mitosis. To do this, the nuclear mean pixel intensity of Whi5-WIQ-mCitrine was plotted against time in frames for each cell of interest. The first frame showing nuclear re-import of Whi5 was manually identified and assigned as the first frame of the cell in telophase. This frame and all following frames in the cell cycle were categorised as post-anaphasic.

Lastly, the start of anaphase was assigned by examining the trends in the background-adjusted Htb2-mScarlet-I amount in the bud. The amount of Htb2-mScarlet-I when plotted against time in frames showed a sudden and strong increase when the dividing nucleus entered the bud. This typically occurs during anaphase. Therefore, the frame at which the Htb2-mScarlet-I amount in the bud started increasing was manually labelled for each cell as the start of anaphase. All frames between this frame and the first post-anaphasic frame were categorised as anaphasic. The remaining S/G2/M frames starting from bud emergence and up until anaphase were assigned to the pre-anaphasic category which encompassed S-phase, G2-phase, prophase and metaphase.

2.19. Statistical analyses

A confidence interval comparison was performed for comparing CVs of cell volume between strains in the live-cell microscopy data (Fig. 15) and a mixed ANOVA test was used for comparing mean cell volumes and CVs of cell volume between strains in the bulk nutrient switch experiment (Fig. 18). Additionally, Wilcoxon rank sum tests were used for the comparison of *ENO2* and *SUT509* mRNA abundance between strains (Fig. 32). All remaining statistical analyses were performed using independent two-tailed t-tests with the assumption of unequal variances (Welch's). P-values below 0.001 were denoted by '***'. p-values below 0.01 and greater than or equal to 0.001 were denoted by '**'. p-values below 0.05 and greater than or equal to 0.01 were denoted by '*'. p-values greater than or equal to 0.05 were denoted by 'ns' for non-significant.

3. Results

3.1. *WHI5* mRNA is not degraded by Ccr4.

Multiple regulators of cell size at the G1/S transition have been identified (Fig. 4B). While Bck2 has been shown to promote the G1/S transition largely independently of Whi5 and Cln3, work from Manukyan *et al.*[106] proposes an interaction between Bck2 and Whi5 via the cytoplasmic deadenylase Ccr4. They observed an increase in the stability of *WHI5* mRNA in a *GALpr-WHI5 ccr4Δ* strain after a switch from galactose to glucose medium. To better understand the interactions within the G1/S regulatory network, this study attempted to reproduce these results in a strain with endogenous *WHI5* and in steady-state growth conditions. Two orthogonal RNA quantification techniques - RT-qPCR and single molecule fluorescence in situ hybridisation (smFISH) - were used to measure *WHI5* mRNA abundance in the *ccr4Δ* and *bck2Δ* mutants. RT-qPCR revealed that neither a deletion of *CCR4* nor that of *BCK2* leads to a significant increase in *WHI5* transcript abundance (Fig. 11A).

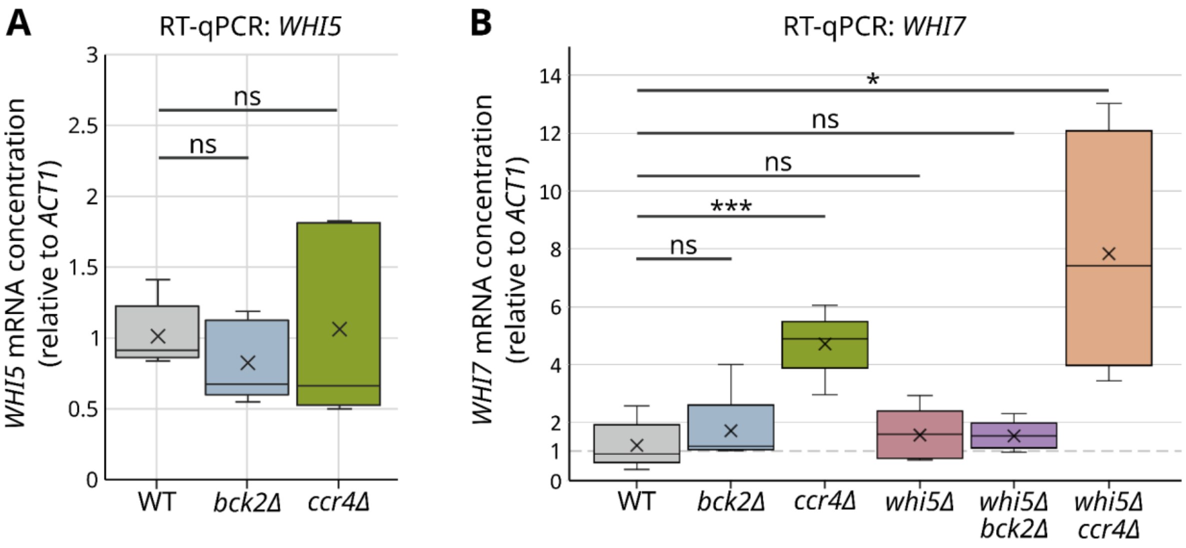

Figure 11: *ccr4Δ* and *bck2Δ* strains do not show increased *WHI5* transcript abundance. *The WHI7* transcript is strongly upregulated in *ccr4Δ* and *whi5Δccr4Δ* cells. mRNA concentration of *WHI5* (**A**) and *WHI7* (**B**) relative to *ACT1* in cells grown in SCD (synthetic complete medium with 2% glucose), as determined from five independent RT-qPCR experiments for **A** and a minimum of four independent RT-qPCR experiments for **B**. x symbol denotes the mean. Independent two-tailed t-tests with the assumption of unequal variances (Welch's t-tests) were used for statistical analysis.

To confirm these RT-qPCR results, smFISH was also performed for *WHI5* transcripts (Fig. 12A-B). A *whi5Δ* control was included to ensure that the smFISH probes were not binding *WHI7*, the paralogue of *WHI5* (Fig. 12B). Cells were categorised into the G1-phase if they did not have a bud and into the S/G2/M-phase if they had a bud. Further cell-cycle categorisation was performed based on the ratio of bud volume to mother volume. If this ratio was greater than 0.3, cells were categorised into the G2/M-phase and if it was less than 0.3, they were categorised into the S-phase. In agreement with previous studies[72,78], *WHI5* transcription was observed to peak during late G1 and S-phase, with an average of 1-2 transcripts per cell (Fig. 12B). Like the RT-qPCR results, smFISH results also showed no significant increase in *WHI5* transcript abundance in *ccr4Δ* and *bck2Δ* cells (Fig. 12B). The negative control (*whi5Δ*, Fig. 12B) had on average 0.07-0.09 spots in the different cell cycle stages, confirming that the smFISH probes used in this study were *WHI5*-specific.

Given that *WHI5* and its paralogue *WHI7* share some sequence similarity, it is possible that Manukyan *et al*.[106] detected both *WHI5* and *WHI7* transcripts in their northern blot. If that had been the case, an upregulation of *WHI7* would be expected in the *ccr4Δ* deletion to explain the increased signal they observed[106]. The next step, therefore, was to test whether *WHI7* is upregulated in the *ccr4Δ* mutant and whether *WHI7* is overexpressed in the absence of *WHI5* as a form of compensation.

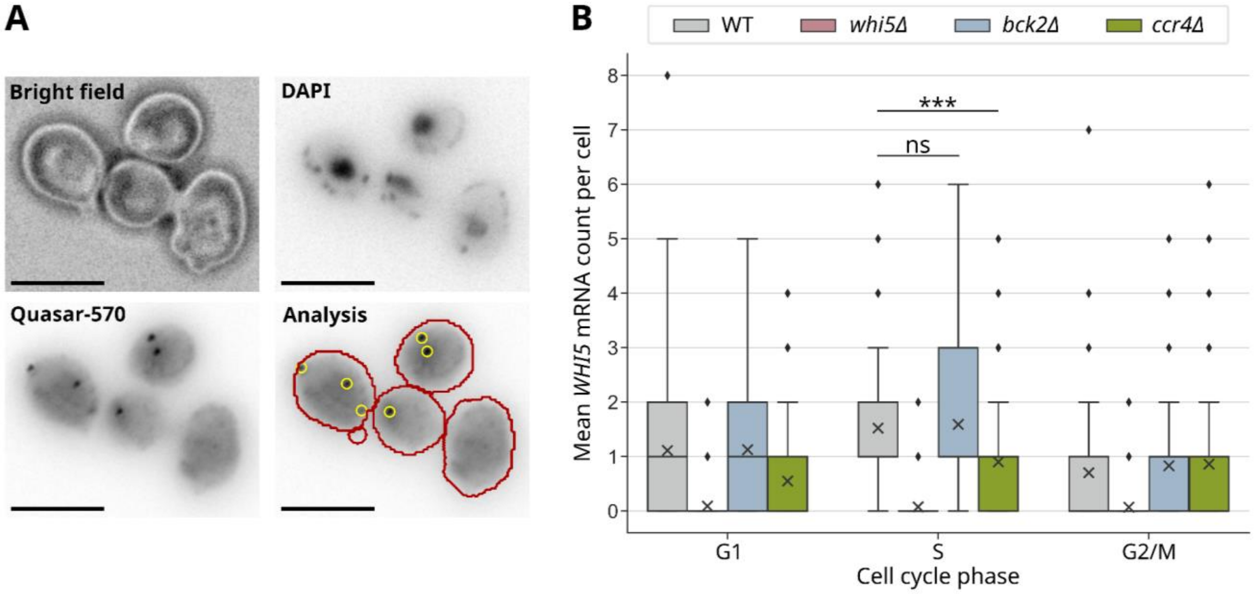

Figure 12: *WHI5* expression peaks during late G1 and S-phase. No increase in *WHI5* mRNA amount is observed in *ccr4Δ* or *bck2Δ* cells. (**A**) Representative WT smFISH images: bright field; nuclear DNA stained with DAPI; *WHI5* mRNA stained with Quasar-570 labelled smFISH probes; the spots detected using Spotmax[130] outlined in yellow and cell contours in red. Scale bars represent 5 µm. (**B**) Mean *WHI5* mRNA count per cell plotted for cells in different cell cycle phases pooled from two independent smFISH experiments performed in SCD. Number of cells in G1-phase: n_{WT} = 98, $n_{whi5\Delta}$ = 121, $n_{bck2\Delta}$ = 196, $n_{ccr4\Delta}$ = 127. Number of cells in S-phase: n_{WT} = 172, $n_{whi5\Delta}$ = 182, $n_{bck2\Delta}$ = 211, $n_{ccr4\Delta}$ = 83. Number of cells in G2/M-phase: n_{WT} = 125, $n_{whi5\Delta}$ = 143, $n_{bck2\Delta}$ = 178, $n_{ccr4\Delta}$ = 130. x symbol shows the mean. Independent two-tailed t-tests with the assumption of unequal variances (Welch's t-tests) were used for statistical analysis.

3.2. Whi7 does not compensate for Whi5.

To ascertain whether the expression of the *WHI5* paralogue *WHI7* is upregulated in a *whi5Δ* strain, RT-qPCR was performed on *WHI7* mRNA. *WHI7* transcription was not upregulated in the *whi5Δ* strain (Fig. 11B), indicating that Whi7 likely does not compensate for Whi5. However, *WHI7* transcripts were strongly upregulated in *ccr4Δ* and *whi5Δccr4Δ* cells (Fig. 11B). Whi7 protein levels are known to be upregulated during conditions of cell wall stress[102], when it becomes the more important G1/S inhibitor and serves as a cell-cycle-brake (section 1.7). *ccr4Δ* and *whi5Δccr4Δ* cells were observed to be slow-growing and overgrown in size, making cell wall stress a possible explanation for the increased *WHI7* mRNA concentration observed in these cells. This upregulation of *WHI7* mRNA in the *ccr4Δ* mutant and the potential off-target binding of *WHI5* northern-blot probes to *WHI7* transcripts could together explain the increased stability of *WHI5* that Manukyan *et al*.[106] detected in the *ccr4Δ* strain. To further test for a genetic interaction between Ccr4 and Whi5, cell volumes of *ccr4Δ, whi5Δccr4Δ* and WT cells were compared in bulk populations and at the single-cell level.

3.3. Ccr4 acts independently of Whi5.

One way of testing for a genetic interaction between Ccr4 and Whi5 would be to compare the cell volume of *whi5Δccr4Δ* and *ccr4Δ* cells. If the *whi5Δccr4Δ* double mutant rescues the large cell size of the *ccr4Δ* single mutant, it would indicate that Whi5 indeed lies downstream of Ccr4 in the size control network, as suggested by Manukyan *et al*.[106]. To perform such a comparison, cell volumes of *ccr4Δ* and *whi5Δccr4Δ* cells were recorded at the single-cell level using time-lapse live-cell microscopy (Fig. 13A-C) and in bulk using Coulter-counter measurements (Fig. 13D).

For the time-lapse microscopy, which was also used for multiple subsequent experiments in this study, steady-state cultures of the strains of interest were grown in two different growth media (SCD and SCGE) and transferred to a custom microfluidic device[1] (see Methods section 2.18.2.) in a time-lapse microscopy setup (Fig. 13A). SCD (synthetic complete medium with 2% glucose), is a fermentable medium as it contains glucose as a carbon source whereas SCGE (Synthetic complete medium with 2% glycerol and 1% ethanol) is a respiratory medium as it contains glycerol and ethanol as carbon sources. Traditionally, SCD is referred to as a ‘rich carbon’ medium as it allows shorter doubling times or faster cell growth as compared to SCGE, which is traditionally referred to as a ‘poor carbon’ medium. These ‘rich carbon’ or ‘poor carbon’ labels for growth media can be misleading as the two media require very different metabolic states in cells - fermentation vs respiration - and the ‘quality’ of their carbon sources therefore is not directly comparable. The author takes this opportunity to clarify that while the terms ‘rich carbon’ and ‘poor carbon’ are used often in this study to describe growth media in a simpler way, they are only intended to reflect the faster or slower growth that these media facilitate.

Coming back to the time-lapse microscopy: the steady-state cells grown in either growth medium and loaded into the microfluidics device were imaged at three-minute intervals for up to 16 hours. The resulting videos of cell growth were analysed using the Cell-ACDC pipeline[122]. Cells were segmented and tracked using YeaZ[123] and the cell masks and tracking were manually corrected. Mother-bud pedigrees were also assigned in the Cell-ACDC GUI in a semi-automated manner, resulting in a fully annotated manually corrected dataset containing over thirteen thousand complete cell cycles (Fig. 13A).

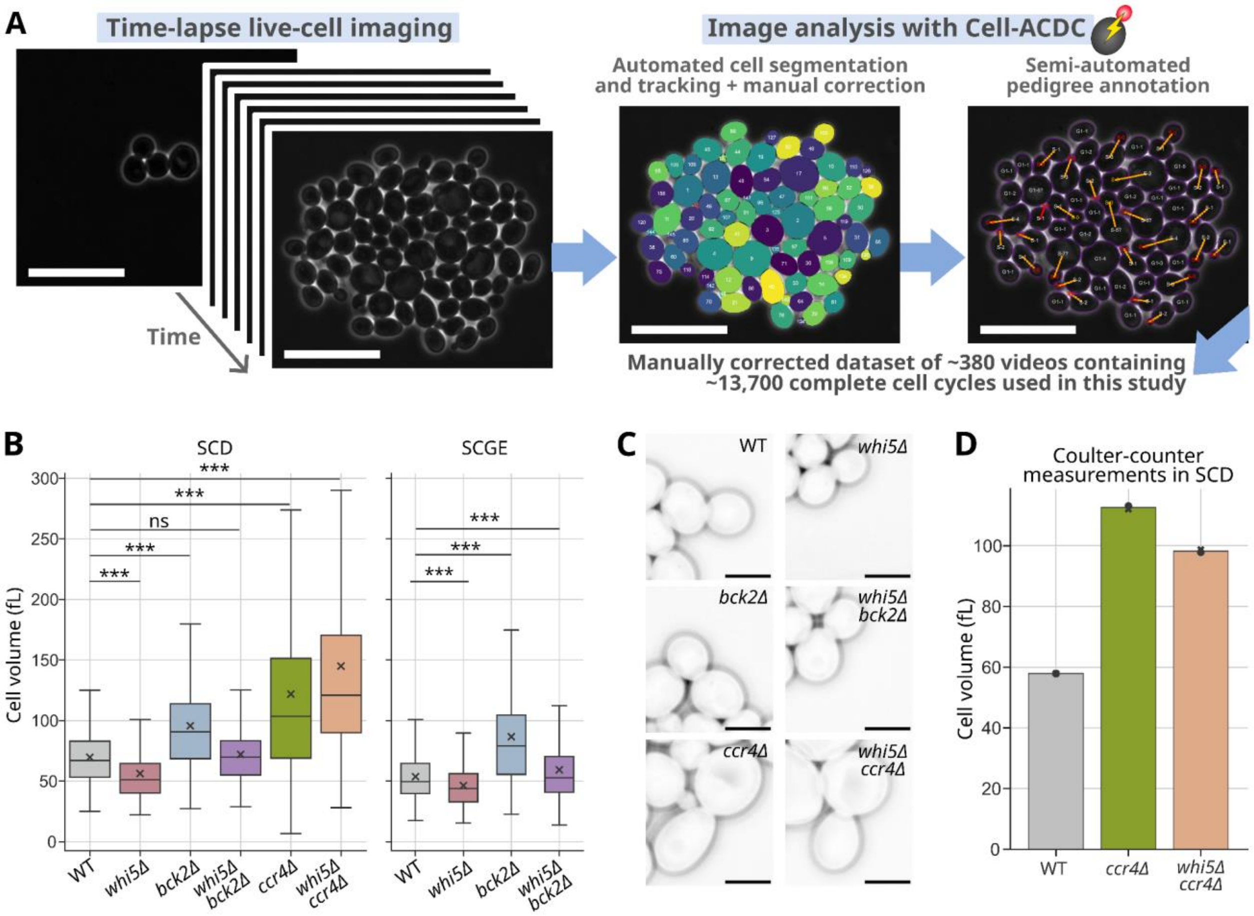

Figure 13: *whi5Δccr4Δ* does not rescue the large cell size of the *ccr4Δ* single deletion. *whi5Δbck2Δ* is strikingly similar to WT in size. (**A**) Live-cell imaging analysis pipeline for the data generated in this study. (**B**) Cell volume distributions of the different strains obtained from steady-state live-cell microscopy in SCD and SCGE are shown as boxplots. For each strain, all living cells in the last frame of each imaging position of two independent experiments were pooled. x symbol shows the mean cell volume of the distribution. Cell numbers (n) for SCD: n_{WT} = 382, $n_{whi5\Delta}$ = 370, $n_{bck2\Delta}$ = 376, $n_{whi5\Delta bck2\Delta}$ = 463, $n_{ccr4\Delta}$ = 241, $n_{whi5\Delta ccr4\Delta}$ = 280. Cell numbers for SCGE: n_{WT} = 533, $n_{whi5\Delta}$ = 370, $n_{bck2\Delta}$ = 429, $n_{whi5\Delta bck2\Delta}$ = 409. *ccr4Δ* and *whi5Δccr4Δ* data in SCGE was excluded from analysis due to poor growth and high death rate. (**C**) Phase-contrast images from steady-state live-cell microscopy in SCD. Representative daughter cells (generation = 1) from different strains are shown just before division. Scale bars represent 5 µm. (**D**) Coulter-counter measurements of cell volume are plotted for cells growing in steady state in SCD. Data is pooled from two replicates. Independent two-tailed t-tests with the assumption of unequal variances (Welch's t-tests) were used for statistical analyses.

The data obtained from this time-lapse live-cell microscopy (Fig. 13B) and coulter-counter measurements (Fig. 13D) was used to compare cell volumes between WT, *whi5Δ*, *ccr4Δ* and *whi5Δccr4Δ* cells. Deletion of the G1/S transition inhibitor Whi5 is expected to result in a quicker transition from G1 into S phase and consequently a smaller cell size due to the shorter G1 growth period [39,73,77]. In agreement with this, live-cell microscopy data showed that *whi5Δ* cells are smaller than wild type cells in both growth media (Fig. 13B). Both live-cell microscopy and coulter-counter data revealed that *ccr4Δ* cells are significantly larger than WT cells (Fig. 13B-D). The double deletion in the *whi5Δccr4Δ* mutant does not rescue the large cell size of the *ccr4Δ* single mutant (Fig. 13B-D), indicating that the large cell size phenotype of the *ccr4Δ* mutant does not stem solely from a modulation of Whi5. This data indicates that Ccr4 affects cell size through pathways other than those involving Whi5. These results, together with the results on *WHI5* transcript abundance (Fig. 11, Fig. 12), are not consistent with *WHI5* transcripts being destabilised by Ccr4, as proposed by Manukyan *et al*.[106]. Instead, the results from this study strongly indicate that Whi5 is not downstream of Ccr4 and the two proteins affect cell size via independent pathways.

3.4. Bck2 acts independently of Whi5

The time-lapse microscopy experiments described in Fig. 13A also provided insight into whether there is a genetic interaction between *WHI5* and *BCK2*. They allowed comparison between cell volumes of *WHI5* and *BCK2* single and double mutants growing in SCD and SCGE (Fig. 13B). Based on what was known from literature, *whi5Δ* cells were expected to be smaller than WT cells whereas *bck2Δ* cells were expected to be bigger[73,76,77,132]. This was because the deletion of the G1/S transition inhibitor Whi5 shortens G1 duration and thereby reduces the amount the cell grows during G1. On the contrary, deletion of a G1/S transition activator such as Bck2 keeps the cell longer in G1, allowing more time for growth and a larger cell size. Indeed, results from this work showed that *whi5Δ* and *bck2Δ* cells are respectively smaller and bigger than wild type cells (Fig. 13B). Interestingly, the volume of *whi5Δbck2Δ* cells is strikingly similar to that of wild type cells (Fig. 13B), which had also previously been observed in bulk populations[77]. These cell volume phenotypes of the different mutants are consistent between both growth media (Fig. 13B). Judging from just the cell volume comparison, it appears that an additional deletion of *WHI5* partially rescues the large size of *bck2Δ* cells, indicating that Whi5 may act downstream of Bck2 in cell size homeostasis. However, the next analysis, which was a comparison of cell cycle properties including cell volume changes, clarified that the effects of Whi5 and Bck2 are additive and that Whi5 and Bck2 likely affect cell size homeostasis independently of each other.

A

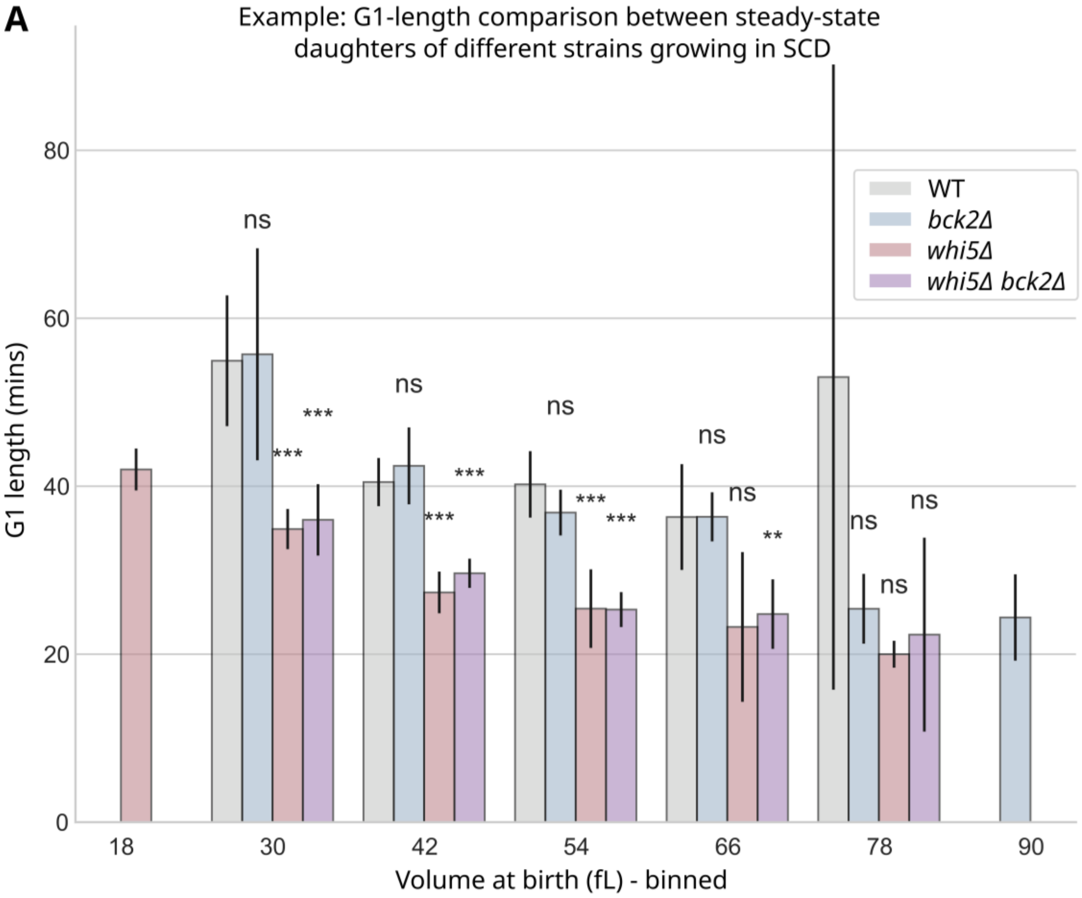

B

Daughters

SCD (glucose media)

Property \ Strain	*whi5Δ*	*bck2Δ*	*whi5Δ bck2Δ*
G1 length	↓	≈	↓
G1 Δvol	↓	≈	↓
S/G2/M length	≈	↓	↓
S/G2/M Δvol	≈	≈	≈
Total Δvol	↓	≈/↑	≈

SCGE (glycerol-ethanol media)

Property \ Strain	*whi5Δ*	*bck2Δ*	*whi5Δ bck2Δ*
G1 length	↓	≈/↑	≈
G1 Δvol	↓	↑	≈
S/G2/M length	↑	↓	≈
S/G2/M Δvol	≈	≈	≈
Total Δvol	↓	↑	≈

Mothers

SCD (glucose media)

Property \ Strain	*whi5Δ*	*bck2Δ*	*whi5Δ bck2Δ*
G1 length	≈	≈	≈
G1 Δvol	≈	≈	≈
S/G2/M length	≈	≈/↓	↓
S/G2/M Δvol	≈	≈	≈
Total Δvol	≈	≈/↑	≈

SCGE (glycerol-ethanol media)

Property \ Strain	*whi5Δ*	*bck2Δ*	*whi5Δ bck2Δ*
G1 length	≈	↑	≈
G1 Δvol	≈	↑	↑
S/G2/M length	↑	↓	≈
S/G2/M Δvol	≈	↑	≈
Total Δvol	≈	↑	≈

↑ Significant increase in majority of size bins w.r.t. WT
↓ Significant decrease in majority of size bins w.r.t. WT
≈ No significant change in majority of size bins w.r.t. WT
/ Num. of size bins equally split between two phenotypes

Figure 14: Since cell cycle phenotypes of *whi5Δ* and *bck2Δ* are additive in *whi5Δbck2Δ*, Bck2 must act independently of Whi5. (**A**) An example of cell cycle property comparison between strains. Here, the G1 length (minutes) is compared between daughter cells (generation = 1) of different strains. Cells with complete G1 phases were pooled from a minimum of two independent experiments and were binned by their cell volumes at birth. The bin size is 12 fL (x-axis values ± 6 fL). Only bins that contained at least three cells were

included in the analysis. The mean G1 length for each strain in each bin is plotted. Only size bins containing both WT and the strain of interest were included in the analysis. Error bars show standard error. Independent two-tailed t-tests assuming unequal variances (Welch's t-tests) were used for statistical analyses. Such individual plots were made for multiple cell cycle properties of both mother (generation >1) and daughter cells growing in two different media: SCD and SCGE. Whether or not a significant difference in each cell cycle property was observed between WT and the strain of interest in the majority of size bins is recorded in (**B**). In (**B**), the two columns of tables refer to the two growth media tested and the two rows of tables refer to daughter and mother cell populations. 'Δvol' refers to the change in cell volume during a given cell cycle phase. 'Total Δvol' represents the change in cell volume over the course of the entire cell cycle. Bud emergence marks the start of S/G2/M phase and cell division marks the start of G1 phase.

The cell volume similarity between *whi5Δbck2Δ* and WT cells raised the question of whether the underlying cell cycle properties, such as the cell cycle phase durations and phase-specific volume changes, were also similar between the double mutant and WT. The time-lapse imaging set-up enabled resolution and comparison of cell cycle properties between different strains. Figure 14A shows how this analysis was performed for one example cell cycle property: G1 length. Daughter cells, i.e, cells which were in their first cell cycle, were divided into various size bins based upon their cell volume at birth. The G1-lengths were then compared between different strains in each size bin. Whether or not a strain showed a significant difference in the cell cycle property with respect to wild type in the majority of size bins was recorded in the tabular form shown in Figure 14B. This analysis was repeated for multiple cell cycle properties for both daughter and mother cells (generation > 1) in the two different growth media (Fig. 14B). The cell cycle properties included cell cycle phase lengths ('G1 length', 'S/G2/M length'), phase-specific changes in cell volumes ('G1 Δvol', 'S/G2/M Δvol') and the change in cell volume over the entire cell cycle, i.e., from birth to division ('Total Δvol'). *WHI5* and *BCK2* single deletions affected multiple cell cycle properties (Fig. 14B). For example, *whi5Δ* daughters indeed had shorter G1 lengths, as is expected from the deletion of a G1/S inhibitor. However, since this reduction in G1 length was only observed in *whi5Δ* daughters, it appears that Whi5's regulation of G1 length is much stronger in daughter cells than mother cells. This differential effect of the *whi5Δ* deletion on daughter G1 lengths could also stem from the much longer G1s observed in daughter cells as compared to mother cells[133], which might make it easier to resolve differences between strains. The deletion of *BCK2* led to an increase in G1 length, as is expected from the deletion of a G1/S activator. This effect, however, was only observable in SCGE medium, likely also due to the longer G1 lengths in SCGE allowing for better resolution of differences between strains. These observations emphasized that the effects of the deletions on cell cycle properties were dependent on the growth medium and cell type (mother vs daughter).

The single deletions of *whi5Δ* and *bck2Δ* also led to an altered 'Total Δvol' property, explaining why cells of these strains ended up smaller and bigger than wild type, respectively (Fig. 14B). In the *whi5Δbck2Δ* double mutant, the opposing size-phenotypes of the two deletions appeared to cancel each other out to result in cells that resemble wild type cells in size. In 'Total Δvol' as well as in other cell cycle properties, the effects of both single deletions appeared to be additive in the double deletion, indicating that Whi5 and Bck2 act in independent pathways. These results further disputed Manukyan *et al*.[106]'s proposal that Whi5 acts downstream of Bck2 and Ccr4. Moreover, the surprising similarity between the cell volumes of *whi5Δbck2Δ* and WT cells indicated that two important size regulators may be dispensable in the maintenance of WT-like size. Another explanation for this similarity in cell size between *whi5Δbck2Δ* and WT cells was that it was merely the cumulative effect of two deletions with contradictory phenotypes, resulting in a net-zero cell volume phenotype. If this were the case, the loss of the two size regulators should still lead to a loss of size homeostasis efficiency, as assessed by the coefficient of variation of cell volume.

3.5. *whi5Δbck2Δ* has more efficient size homeostasis than *whi5Δ* and *bck2Δ* in glucose medium

The coefficient of variation (CV) of cell volume is the mean-normalised standard deviation of the cell volume distribution, making it a measure of size homeostasis efficiency which is comparable between differently sized strains. The similarity between the cell volumes of *whi5Δbck2Δ* cells and WT raised the question of how efficient size homeostasis is in the *whi5Δbck2Δ* double mutant. The CVs of cell volume were calculated from time-lapse live cell microscopy data (Fig. 15A) and from coulter-counter measurements (Fig. 15B). As was expected given their roles in G1/S size control, *whi5Δ* and *bck2Δ* had an increased CV of cell volume, both for cells growing on SCD and on SCGE medium (Fig. 15A). This indicated that a deletion of *WHI5* or *BCK2* reduced the efficiency of size homeostasis. By that logic, a double deletion of both *WHI5* and *BCK2* was expected to lead to an even stronger disruption of cell size homeostasis. Surprisingly, the CV of cell volume of *whi5Δbck2Δ* cells was not higher than the CVs of *whi5Δ* and *bck2Δ* cells (Fig. 15A). In fact, in SCD, *whi5Δbck2Δ* cells even showed a significantly lower CV than both *Δwhi5* and *Δbck2* (Fig. 15A), similar to wild-type cells. Thus, cell size homeostasis, as evaluated by the CV of cell volume across a steady-state population, was found to be surprisingly robust to the double deletion of *WHI5* and *BCK2*, in particular for cells grown in SCD.

In contrast, deleting *CCR4* resulted in a dramatically increased CV of cell volume for cells grown in SCD, which was not rescued by an additional *WHI5* deletion (Fig. 15A-B). This indicated the rare occurrence of a drastically impaired size-homeostasis mechanism. However, since *ccr4Δ* cells grow very poorly, especially in SCGE, it is unlikely that this reduced size homeostasis is a result of disrupted G1/S size control alone. To gain insight into how G1/S size homeostasis efficiency is affected by deletions of different G1/S size homeostasis proteins, the relationship between G1 length and cell volume at birth was studied next.

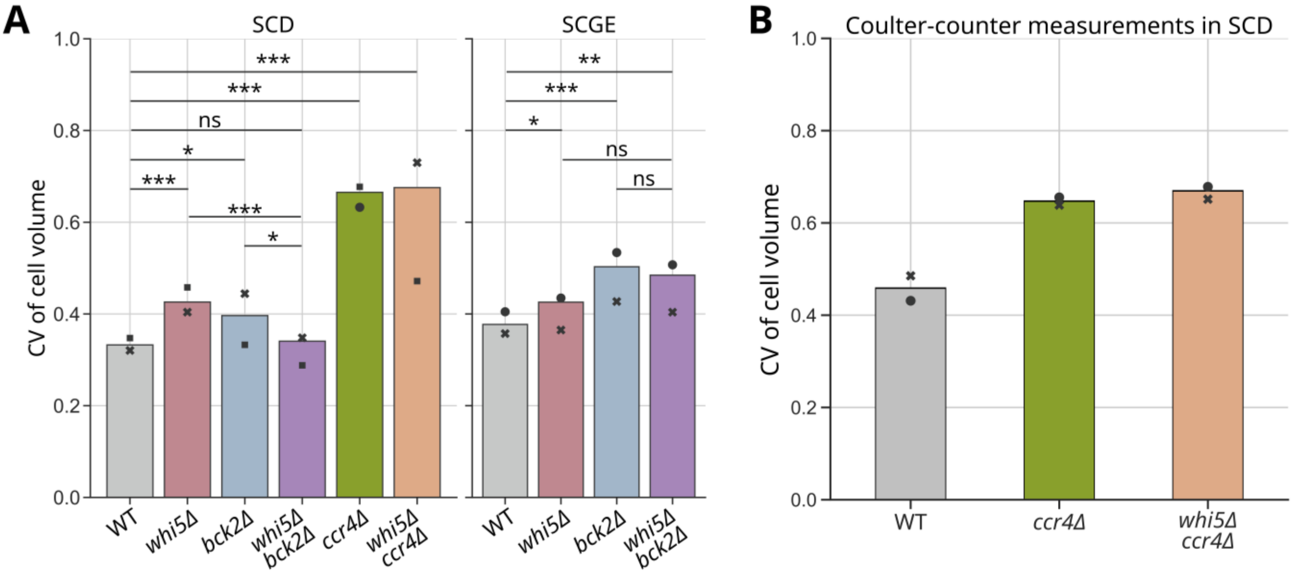

Figure 15: *whi5Δbck2Δ* has more efficient size homeostasis than *whi5Δ* and *bck2Δ* in glucose medium. (**A**) The live cell microscopy dataset described in Figure. 13B was used for calculating the coefficient of variation (CV) of cell volume, as a measure of size homeostasis efficiency. For each strain, all living cells in the last frame of each imaging position of two independent experiments were pooled and the resulting CV of cell volume is represented by the bar heights. •, ■, and x symbols are used to show the CVs of cell volume calculated from only the cells of independent experimental replicates. In **A,** statistical comparison between the strains was performed by comparing overlaps between 10000 bootstrap samples (details in Methods section 2.18.3.1). (**B**) The coulter-counter dataset used in Fig. 13D was also used to calculate the CV of cell volume for WT, *ccr4Δ* and *whi5Δccr4Δ* cells. Cells were pooled from two replicates, shown here by • and x symbols.

3.6. *ccr4Δ* and *whi5Δccr4Δ* cells show disrupted size homeostasis at the G1/S transition.

The principle underlying G1/S cell size homeostasis is that G1 duration is dependent on the cell volume at the beginning of G1. Cells born bigger undergo shorter G1 phases and cells born smaller undergo longer G1 phases to reduce cell size variation in the population at the end of G1[50,134]. Thus, one way of observing G1/S size homeostasis is by plotting G1 duration against cell volume at birth (Fig. 16A). A more negative slope of the resulting regression line means longer G1 durations for cells that were born smaller and therefore indicates stronger size homeostasis. Alternatively, a slope close to 0 indicates a birth-volume-independent G1 duration and therefore an absence of size homeostasis. While WT, *whi5Δ*, *bck2Δ* and *whi5Δbck2Δ* daughter cells have strongly negative slopes and therefore, intact size homeostasis, *ccr4Δ* and *whi5Δccr4Δ* cells show a strong disruption in size homeostasis (Fig. 16A). This is also reflected in the weaker correlation between G1 duration and birth volume in *ccr4Δ* and *whi5Δccr4Δ* cells, represented by the Pearson correlation coefficient (r). In fact, the G1 duration in *ccr4Δ* and *whi5Δccr4Δ* cells appears to be largely cell-volume-independent. This is in agreement with the dramatically lower size homeostasis efficiency observed in these strains when the CV of cell volume was analysed (Fig. 15).

Another standard method used in the field to assess the strength of size homeostasis is a slight modification of the G1-length-birth-volume comparison performed in Figure. 16A. This method, described by Di Talia *et al.*[70], calculates the dependence of a growth-rate-adjusted G1 duration on cell volume at birth via linear regression. According to this method, the growth rate, α, of exponentially growing daughter cells was calculated as the slope of the natural logarithm of cell volume (in [fL]) plotted against time. For each cell that underwent a complete cell cycle, αG1, the growth-rate adjusted G1 duration, was calculated by multiplying G1 duration and α. This growth-rate-adjusted G1 duration (αG1) was then plotted against the natural logarithm of birth volume and a linear regression was performed (Fig. 16B). Similar to Fig. 16A, a negative slope of the resulting regression line indicated that G1 duration was indeed strongly dependent on birth volume, and indicated strong G1/S cell size homeostasis. Conversely, a slope closer to 0 indicated a birth size-independent G1 duration and therefore weaker G1/S cell size homeostasis. Surprisingly, using this method to assess G1/S size homeostasis strength revealed a very different result for *ccr4Δ* and *whi5Δccr4Δ* cells (Fig. 16B). If just G1 duration was considered, these strains showed disrupted size homeostasis (Fig. 16A). However, if growth-rate adjusted G1 duration was considered (Fig. 16B), these strains appeared to have intact size homeostasis, but much lower correlation between αG1 and birth volume than the other strains. This indicated that for the *ccr4Δ* and *whi5Δccr4Δ* strains, the difference between G1 duration and αG1 was coming from differences in α, the growth rate.

To test whether the divergence between G1 duration and αG1 for the *ccr4Δ* and *whi5Δccr4Δ* strains was α-dependent, αG1 was plotted against G1 duration and the growth rate (α) of each cell was represented through the color of the data points (Fig. 16C). For WT, *bck2Δ* and *whi5Δbck2Δ* daughter cells, αG1 and G1 duration were found to be strongly correlated, as is expected if both growth rate and G1 duration are cell-volume-dependent (Fig. 16C). For the *ccr4Δ* and *whi5Δccr4Δ* strains, however, the correlation between αG1 and G1 duration appeared weaker as many cells showed a much lower αG1:G1 duration ratio than expected (Fig. 16C). The color of these data points confirmed that their lower αG1 values stemmed from lower α values (Fig. 16C). As a part of the Ccr4-Not complex, Ccr4 is known to regulate the production, nuclear export, translation and degradation of many mRNAs[104,105] and its deletion therefore can have widespread effects on cell function. It is possible that the absence of Ccr4 leads to sick cells with reduced growth rates, which may give a false impression of intact size homeostasis (Fig. 16B). The very large cell size (Fig. 13), very low size homeostasis efficiency (CV of cell volume analysis, Fig. 15) and the size-independent G1 duration of *ccr4Δ* and *whi5Δccr4Δ* cells (Fig. 16A), however, still indicate a strong disruption of size homeostasis in these strains. Since cell size homeostasis efficiency is very robust to deletions of size regulators[73], the *ccr4Δ* and *whi5Δccr4Δ* mutants serve as rare examples of inefficient size homeostasis systems.

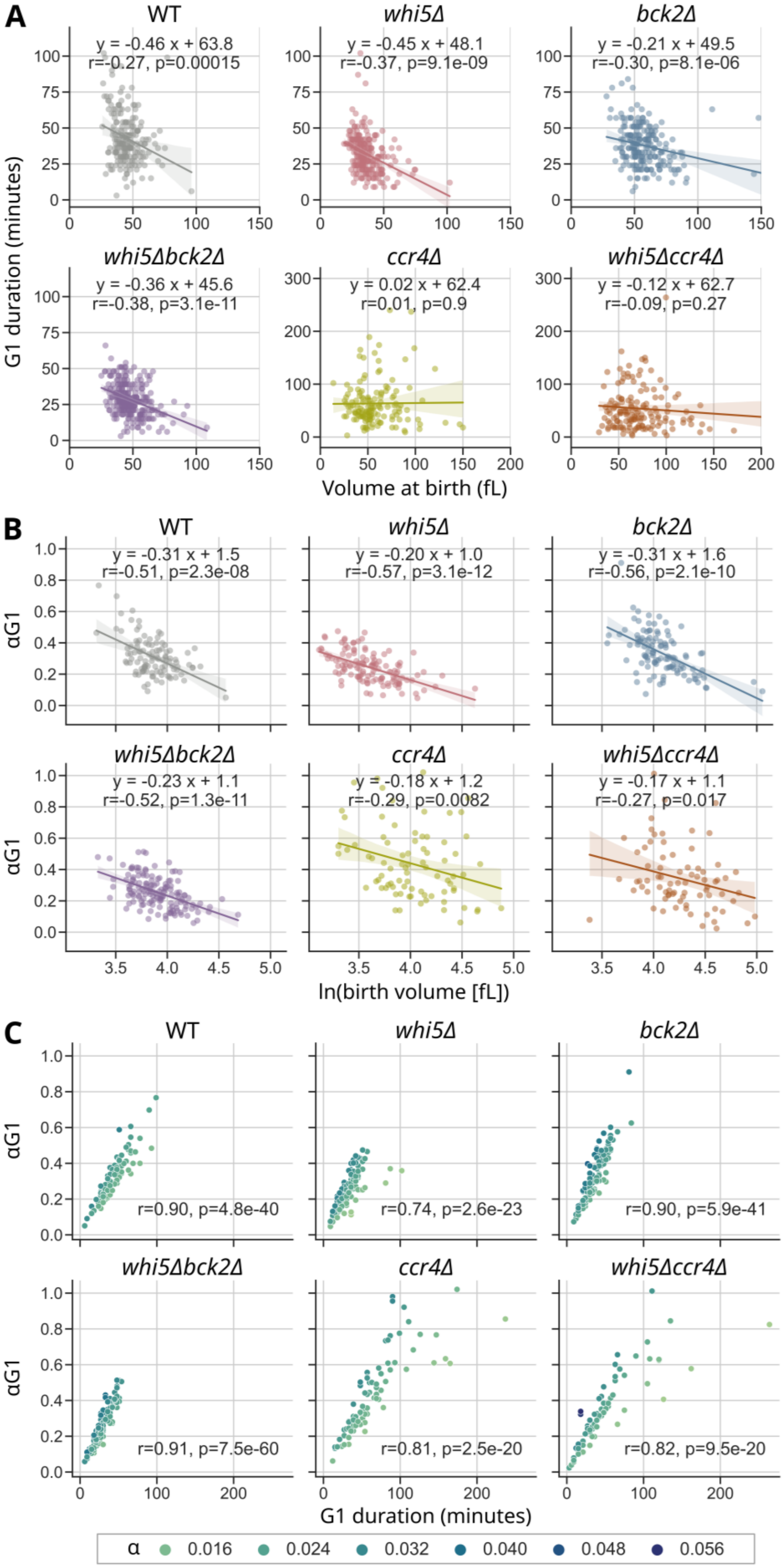

Figure 16: *ccr4Δ* and *whi5Δccr4Δ* cells show disrupted size homeostasis at the G1/S transition. (**A**) The live cell microscopy dataset used in Fig. 13B is used for plotting G1 duration (minutes) against volume at birth

(fL) for daughter cells growing in steady-state conditions in SCD. Daughter cells from two independent experimental replicates that went through a complete G1 phase during the course of the experiment were pooled. Linear regression was performed on the resulting scatter plot and the equation for the resulting line is provided on each panel. Shaded areas show 95% confidence intervals. Pearson correlation coefficient (r) and p-value for testing non-correlation (p) are also displayed on each panel. Note: the axes are different for *ccr4Δ* and *whi5Δccr4Δ* panels. The x-axes have been cut short in the *bck2Δ* and *whi5Δccr4Δ* panels to exclude outliers and maintain uniformity. (**B**) The strength of size homeostasis at the G1/S transition in different cell categories is assessed here as per the method described by Di Talia *et al*.[70]. The growth rate for exponentially growing cells, α, is the slope of the natural logarithm (in [fL]) of cell volume plotted against time. It is calculated for all complete cell cycles of daughter cells collected from two independent experimental replicates. For each cell, G1 length is multiplied by α to obtain a growth rate adjusted G1-duration, αG1. Here, αG1 is plotted against the natural logarithm of birth volume and a linear regression is performed. The equation for the resulting regression line is printed on each panel. Shaded areas show 95% confidence intervals. Pearson correlation coefficient (r) and p-value for testing non-correlation (p) are also displayed on each panel. (**C**) αG1 is plotted against G1 duration (minutes). The data points are color-coded to represent the value of α (see legend), with a lighter color representing a lower value of α and a darker color representing a higher value of α. Pearson correlation coefficient (r) and p-value for testing non-correlation (p) are also displayed on each panel.

3.7. Population-level similarities in cell volume and CV of cell volume between WT and *whi5Δbck2Δ* cells in SCD can be reproduced when individual cell populations or cell cycle transitions are studied.

In the cell volume and CV of cell volume analyses in figures 13B and 15A, all living cells in the last frames of all positions of a strain were pooled to maximise cell number. This masked the effects of cell cycle stage and cell generation number on cell volume and its variability. It is well known from literature that both cell volume and CV of cell volume differ significantly between daughter cells (generation = 1) and mother cells (generation >1) and between different cell cycle stages[36,135,136]. To disentangle the effects of cell cycle stage and generation number on cell volume and its variability, cell volume and its CV were now plotted separately for daughters and mothers at three different cell cycle stages: birth, bud emergence and division (Fig. 17A-B). As expected, cell volume continued to increase as the cell cycle progressed for all strains in both growth media (Fig. 17A-B). The CV of cell volume largely decreased as the cell cycle progressed (Fig. 17C-D). This decrease in CV of cell volume over the course of the cell cycle was also anticipated, as size homeostasis mechanisms reduce variability in cell volume[36]. Within each strain, mother cells were clearly larger than daughter cells at birth (Fig. 17A-B). *whi5Δ* and *bck2Δ* cells were respectively smaller and larger than wild type cells in all conditions and *ccr4Δ* and *whi5Δccr4Δ* cells were bigger than wild type in all conditions (Fig. 17A-B). In SCGE, both *whi5Δbck2Δ* mothers and daughters were slightly but significantly larger than their wild type counterparts (Fig. 17B). The CVs of cell volume of *whi5Δbck2Δ* mothers and daughters also appeared to be higher than those of wild type mothers and daughters in SCGE (Fig. 17D). In SCD, however, the cell volumes and CVs of cell volume were largely similar between WT cells and *whi5Δbck2Δ* cells, across cell cycle stages and for both daughters and mothers. This confirmed that the similarity in cell volume and CV of cell volume observed between WT and *whi5Δbck2Δ* cells in SCD was not an artefact of pooling cells of all cell cycle stages and ages together but was also observable in individual cell populations.

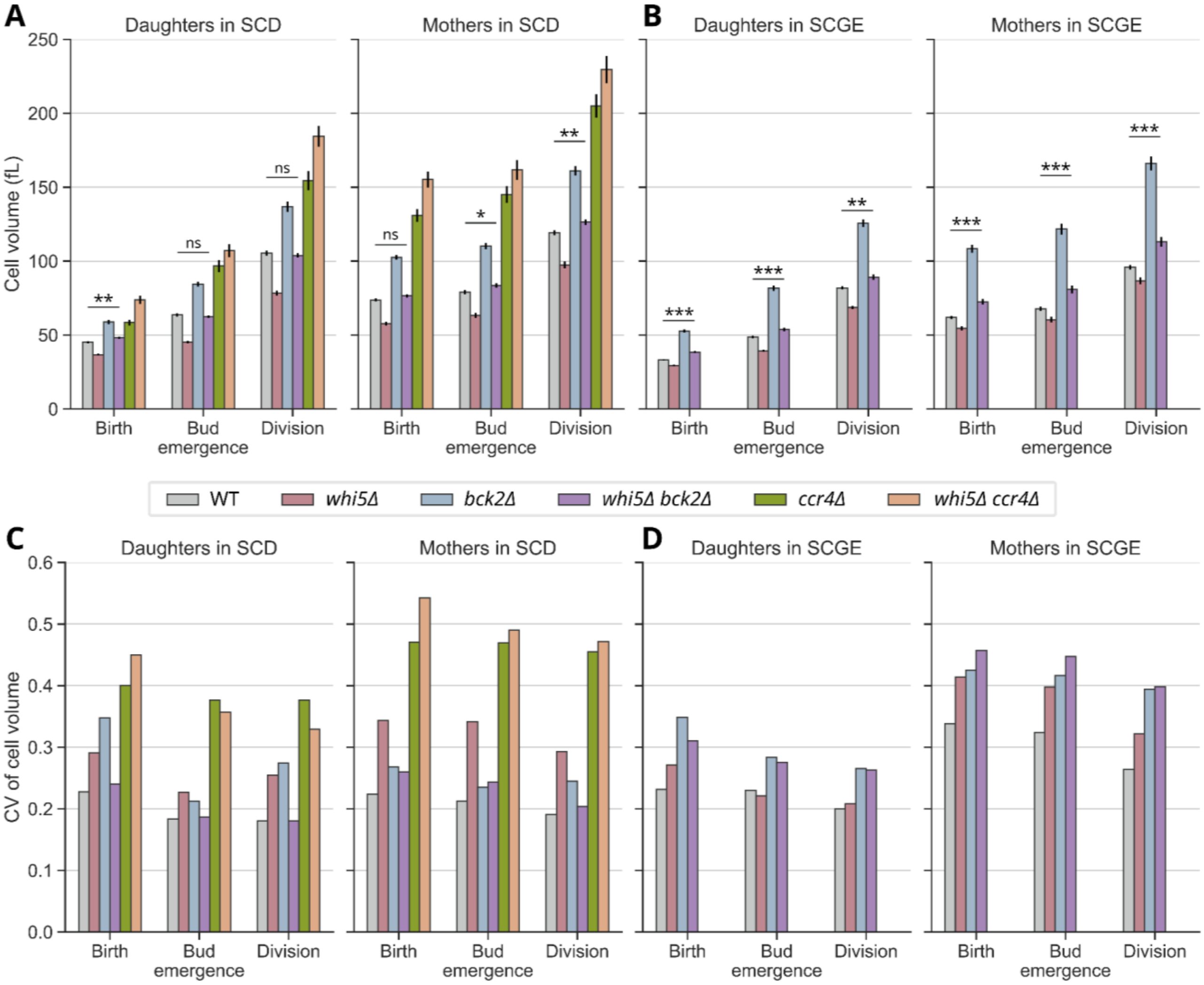

Figure 17: Population-level similarities in cell volume and CV of cell volume between WT and *whi5Δbck2Δ* cells in SCD can be reproduced when individual cell populations or cell cycle stages are studied. Data from a minimum of two independent experiments of live-cell microscopy was pooled and cell volume (fL) at birth, bud emergence and division was plotted for daughter (generation = 1) cells and mothers (generation >1) growing in SCD (**A**) or SCGE (**B**). The CV of cell volume at birth, bud emergence and division was also plotted for daughters and mothers growing in SCD (**C**) and SCGE (**D**). Error bars show standard error. Independent two-tailed t-tests with the assumption of unequal variances (Welch's t-tests) were used for statistical comparisons.

3.8. Following a nutrient switch, *whi5Δbck2Δ* shows a stronger disruption of size homeostasis efficiency than wild type.

Live-cell microscopy data had so far allowed the surprising observation that while individual deletions of *WHI5* and *BCK2*, two major G1/S cell size regulators, led to altered cell volumes and weaker size homeostasis, the absence of both proteins together did not have a stronger size homeostasis phenotype in SCD medium. Since this observation was made in steady-state experiments, and since both Whi5 and Bck2 had previously been connected with nutrient-sensing, there was the possibility that the double deletion of *WHI5* and *BCK2* showed a loss of size homeostasis efficiency in changing nutrient conditions, i.e., after a nutrient switch. To test this, a bulk nutrient switch experiment was performed where exponentially growing cells were shifted from SCD (rich carbon) to SCGE (poor carbon) medium (Fig. 18A). Steady-state populations of cells growing in SCD were washed with and inoculated into SCGE (Fig. 18A) at a starting OD_{600nm} of 0.01. A time course of OD_{600nm} and coulter-counter measurements of cell volume was performed from the time of the nutrient switch up until a new steady-state in the glycerol-ethanol medium was attained (Fig 18B-D). Up until the 30-hour time point, the OD_{600nm} of the cultures was below 1.0. For the two remaining time points after this one, cells were appropriately diluted to maintain their OD_{600nm} below 1.0. The results showed a surprising peak in both cell volume and CV of cell volume between 10 and 20 hours after the nutrient switch (Fig. 18B, D). This initial increase in cell volume was surprising because the medium was switched from rich to poor, ultimately leading to smaller cell volumes after the switch. The sharp increase in CV was surprising because the CV of cell volume is known to be very tightly regulated in steady-

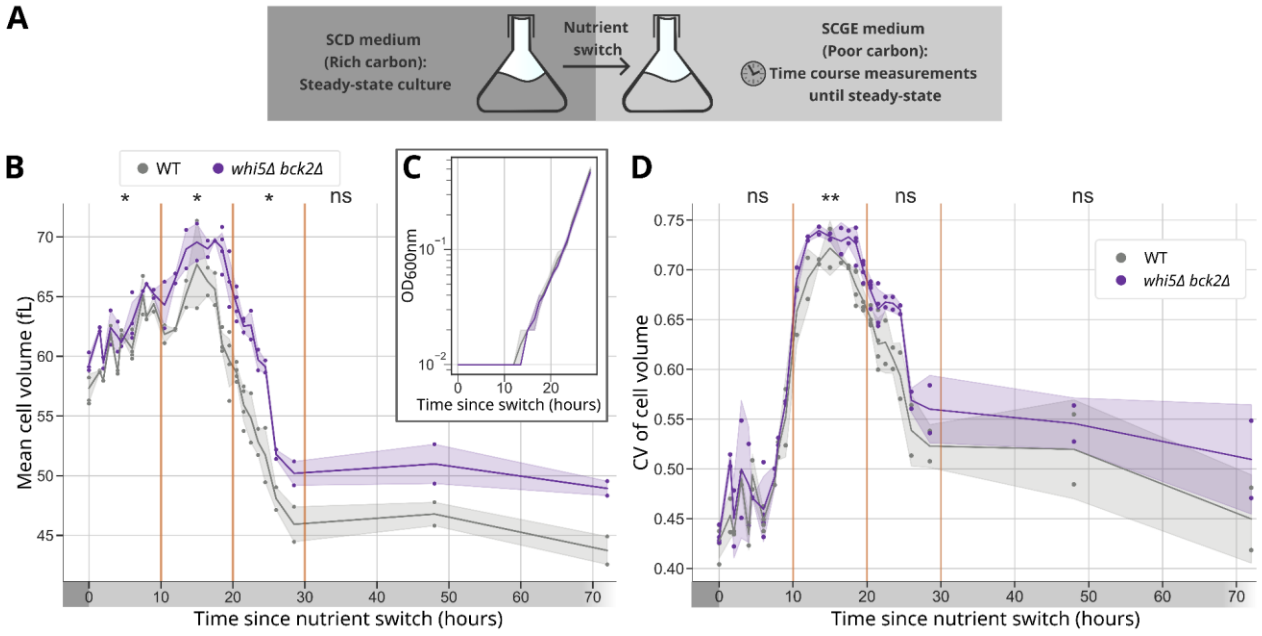

Figure 18: The increase in CV of cell volume observed after a nutrient switch is stronger in whi5Δbck2Δ than wild-type cells. (**A**) Experiment design for the bulk nutrient switch experiment. Cells growing exponentially in SCD were washed with and inoculated into SCGE. A time course of OD_{600nm} and coulter-counter measurements was performed until cells reached steady-state in SCGE. For the measurements taken 48 and 72 hours after the nutrient switch, appropriate dilutions were made when necessary to maintain the OD_{600nm} of the cultures between 0.1 and 1 (see Methods section 2.17. for more details) (**B**) Mean cell volume and OD_{600nm} (**C**, inset) are plotted against time since the nutrient switch (hours). Shaded areas show 95% confidence intervals. Each time point shows data from at least two experiments. (**D**) The CV of cell volume is plotted against time since the nutrient switch (hours). Shaded areas show 95% confidence intervals. Statistical analysis in **B** and **D** was performed by dividing the time course into three ten-hour windows (orange lines). The remaining two time points were grouped together. A mixed ANOVA test was performed for every time interval (see Methods section 2.17. for more details).

state conditions[73]. Moreover, there was no prior knowledge about how the CV of cell volume looks after a nutrient switch. Both mean cell volume (Fig. 18B) and CV of cell volume (Fig. 18D) increased for the first 15 hours after the nutrient switch and this increase was not accompanied by notable cell proliferation (Fig. 18C). Around 15 hours after the switch, OD_{600nm} started to increase (Fig. 18C), and at the same time mean cell volume and CV of cell volume started to decrease (Fig. 18B, D). Interestingly, during the time of maximal cell volume around 10-20 hours post-switch, the CV of cell volume of *whi5Δbck2Δ* cells was significantly higher than that of wild type (Fig. 18D). After the 20 hours post-switch mark, the CV of *whi5Δbck2Δ* appeared to be slightly higher than that of wild type for the remainder of the experiment but the difference was not statistically significant. Thus, while both wild-type and *whi5Δbck2Δ* cells exhibited an increase in cell volume and CV of cell volume post-switch, *whi5Δbck2Δ* had lower size homeostasis efficiency. This suggested that the simultaneous loss of Whi5 and Bck2 has a more prominent effect on size adaptation in changing nutrients as compared to size homeostasis in steady state conditions. These observations raised the questions of what caused the spikes in cell volume and CV of cell volume after a nutrient switch and what led to the higher disruption of size homeostasis efficiency in *whi5Δbck2Δ*. To answer these questions, it was important to obtain single-cell information during the nutrient switch.

3.9. Cell categorisation system for analysis of live-cell imaging coupled to a nutrient switch

In order to understand the spike in cell volume and CV of cell volume observed after the nutrient switch, single-cell information was obtained by performing live-cell microscopy in combination with the nutrient switch. The same custom microfluidic device as used in Figure. 13 and described in detail in section 2.18.2 was loaded with exponential SCD cultures of WT, *whi5Δ*, *bck2Δ* and *whi5Δbck2Δ* cells imaged in the time-lapse microscopy setup at three-minute intervals. For the first two hours, the cells were grown in SCD medium (Fig. 19A). At the two-hour time point, the medium in the microfluidic device was automatically switched to SCGE using the microfluidic flow controller. The cells were then allowed to grow in SCGE for the next 25 hours (Fig. 19A). The videos of cell growth generated in this experiment were analysed using the image analysis pipeline as described in Figure. 13A.

A preliminary qualitative inspection of the nutrient switch videos revealed that while growing in SCD for the first two hours of the experiment, most cells completed at least one cell cycle, resulting in an approximate doubling of cell number. One representative imaging position with WT cells is depicted in Figure 19A. The nutrient switch to SCGE led to a roughly five-hour long cell cycle arrest (WT) during which cells continued to grow in cell volume (Fig. 19A). As cells resumed cell cycle progression after roughly five hours (WT), the cell volume distribution appeared to become increasingly heterogeneous, as it contained both overgrown cells that had faced the cell cycle arrest

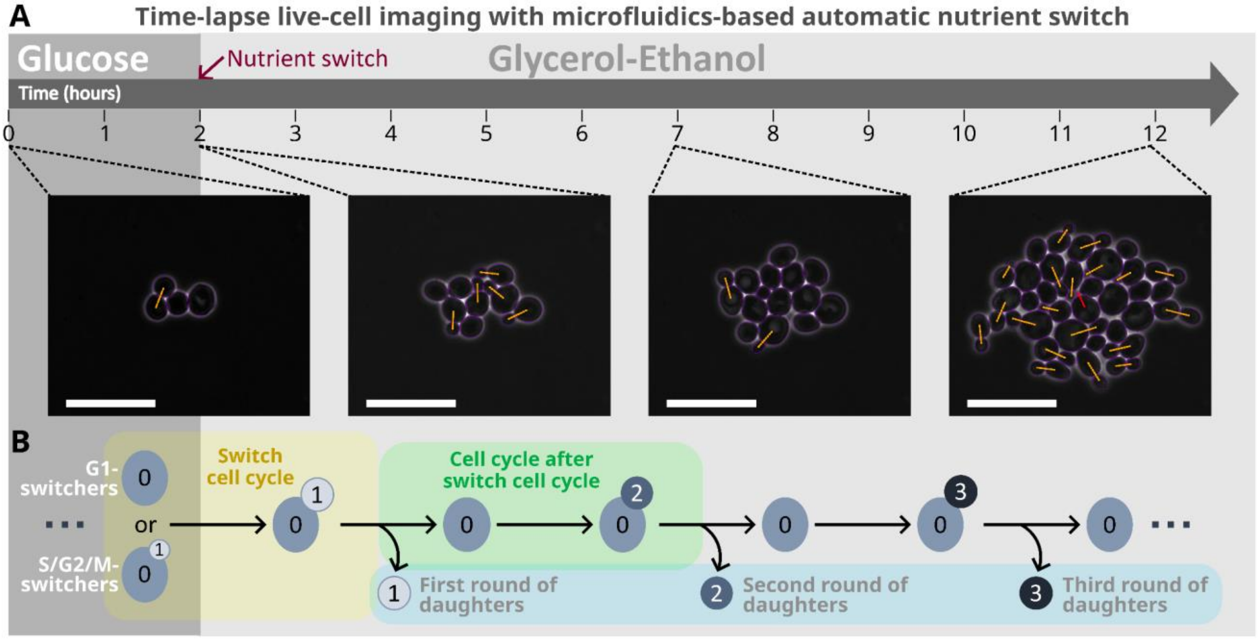

Figure 19: Analysis strategy for live-cell microscopy of the adaptation to the nutrient switch. (**A**) Representative images of WT cells at different time points in the nutrient switch live-cell microscopy experiment. Scale bars represent 20 µm. (**B**) Schematic explanation of cell categories used in the downstream analysis of the nutrient switch live-cell microscopy dataset.

and smaller cells that were born after the arrest (Fig. 19A). Indeed, the cell volume distributions widened and became strikingly bimodal around 7.5 hours after the switch for all strains studied (Fig. 20). This increased heterogeneity in the cell volume distribution was in agreement with the increasing CV of cell volume previously observed in the bulk experiment between 5 and 15 hours after the nutrient switch (Fig. 18D). Thus, it was evident that the cell cycle arrest after the nutrient switch was leading to the increases in cell volume and CV of cell volume observed in the bulk nutrient switch experiment. However, to quantify arrest durations and volume changes after the nutrient switch and to compare them between strains, cells needed to be categorised based on their cell-cycle stages at the time of the nutrient switch or, if they were born after the switch, their generational distance from the time of the switch.

The categorisation of cells based on their history at the time of the nutrient switch was performed in the following manner. Cells that were growing in SCD and faced the nutrient switch to SCGE were categorised as '*switchers*' (Fig. 19B). If *switchers* were budded at the time of the nutrient switch, they were further categorised as '*S/G2/M-switchers'* and if not, they were categorised as '*G1-switchers'*. The ongoing cell cycle of the *switchers* at the time of the nutrient switch was called the '*switch-cell-cycle*' (Fig. 19B, highlighted in yellow). Immediately after the switch, the *switchers* arrested in the '*switch-cell-cycle*'. The *switchers* overcame the arrest and divided at the end of the *switch-cell-cycle* to give rise to the *first round of daughters* (Fig. 19B, highlighted in blue). The *switchers* then entered

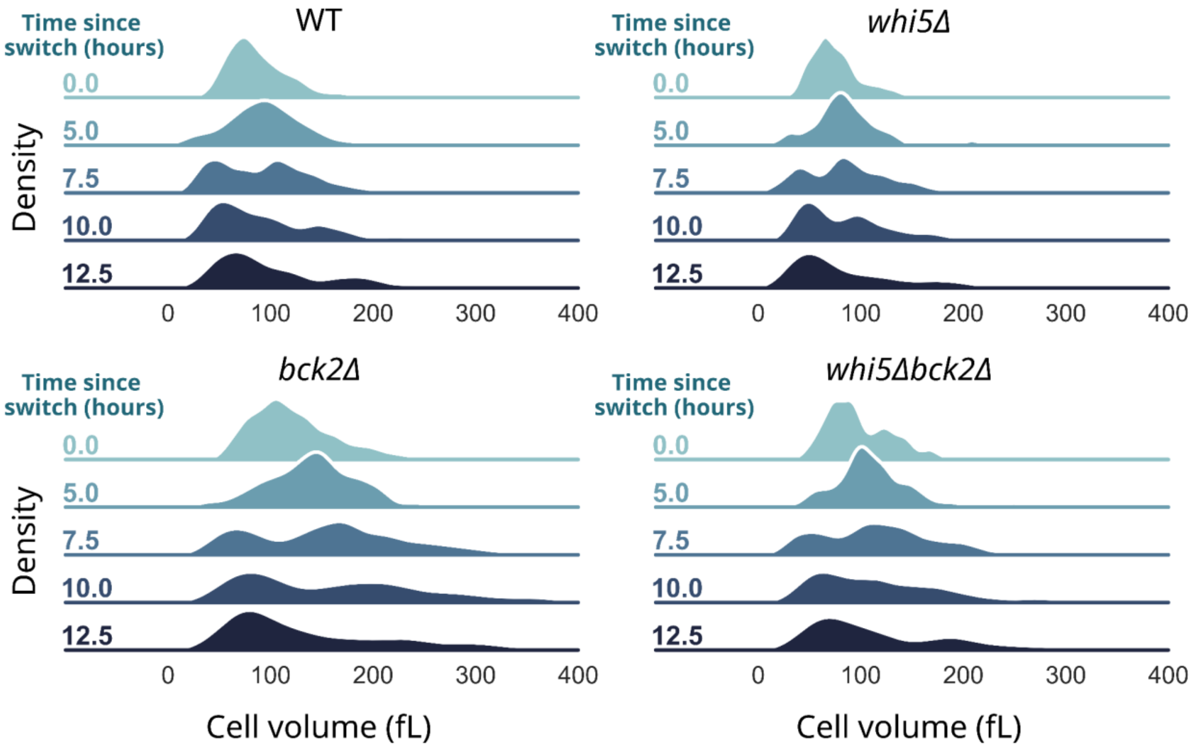

Figure 20: The cell volume distributions become bimodal and heterogeneous around 7.5 hours after the nutrient switch. Kernel density estimation of cell volume distributions was used to compare the shapes of the distributions between different time points after the nutrient switch. Kernel density estimation represents the data using a continuous probability density curve. This probability density is plotted on the y-axis (density) for different time points following the nutrient switch (shown in shades of blue). The x-axis represents cell volume in fL. The kernel density estimates were clipped after 400 fL to exclude very large outliers. Data is normalised in a way that the total area under each curve sums up to 1.

the next cell cycle, labelled as the *cell-cycle-after-switch-cell-cycle* (Fig. 19B, highlighted in green), at the end of which they gave rise to the *second round of daughters* (Fig. 19B, highlighted in blue). The subsequent rounds of daughters were categorised analogously (Fig. 19B, highlighted in blue). Based upon their history, the rounds of daughters were further categorised as *daughters of G1-switchers* or *daughters of S/G2/M switchers*. Importantly, the *first round of daughters of S/G2/M-switchers* was the only cell category apart from the *switchers* themselves that had faced the nutrient switch – as buds of the *S/G2/M-switchers*. Albeit complex, this careful categorisation of cells was crucial for identifying unique phenotypes in response to the nutrient switch in the subsequent analyses. After this cell categorisation, cell cycle phase lengths and cell volume changes could be quantified and compared between the strains within each category of cells.

3.10. The nutrient switch leads to cell cycle arrests in *switchers* and causes stronger cell enlargement in *bck2Δ* cells.

The first category of cells to be analysed were the *G1-* and *S/G2/M-switchers*. Cell cycle phase lengths and cell volumes at the end of those cell cycle phases were plotted for two cell cycles of the

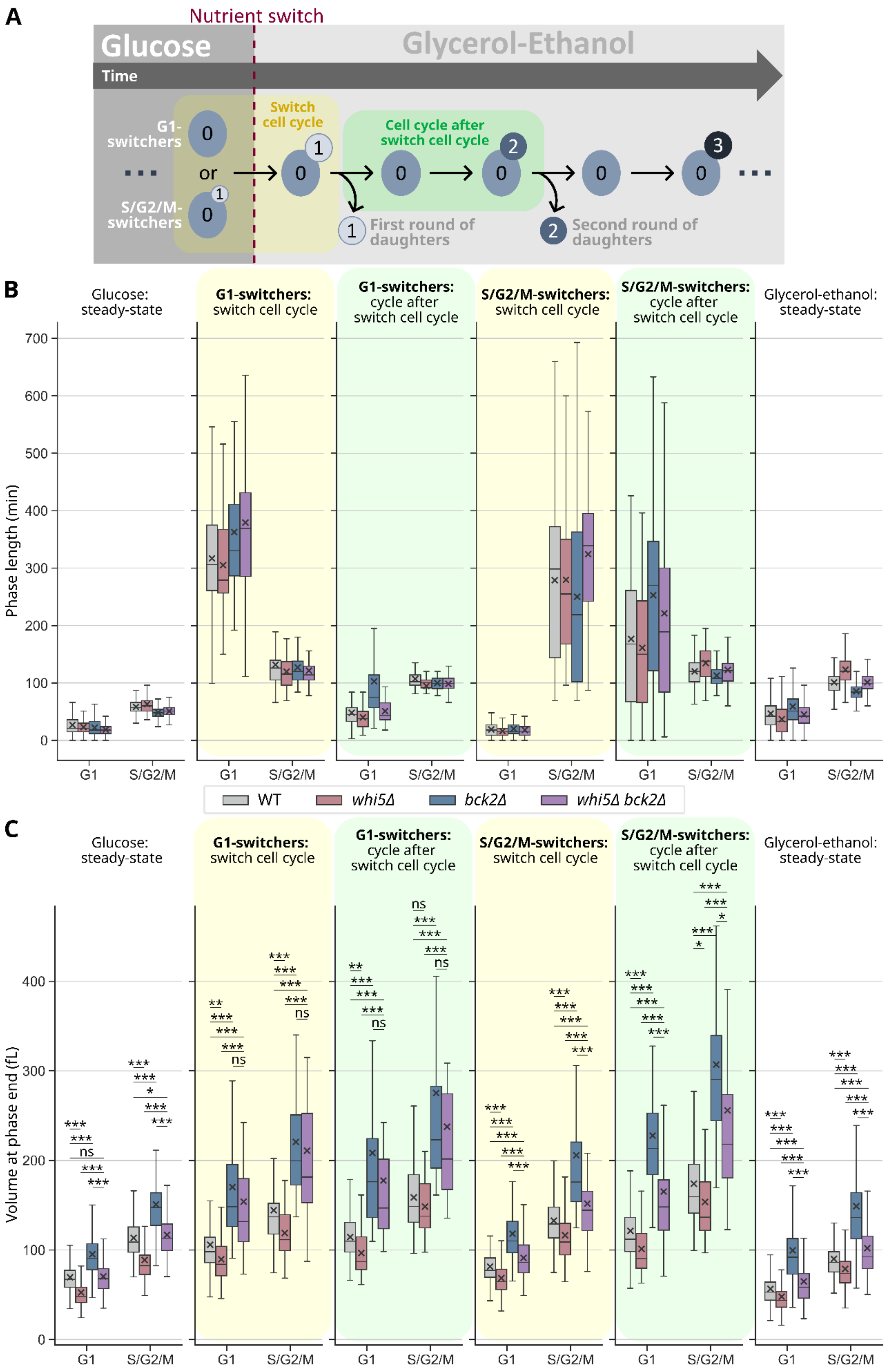
A
Nutrient switch
Glucose
Glycerol-Ethanol
Time
G1-switchers
or
S/G2/M-switchers
Switch cell cycle
Cell cycle after switch cell cycle
First round of daughters
Second round of daughters
0
1
2
3
B
Glucose: steady-state
G1-switchers: switch cell cycle
G1-switchers: cycle after switch cell cycle
S/G2/M-switchers: switch cell cycle
S/G2/M-switchers: cycle after switch cell cycle
Glycerol-ethanol: steady-state
Phase length (min)
0
100
200
300
400
500
600
700
G1
S/G2/M
WT
whi5Δ
bck2Δ
whi5Δ bck2Δ
C
Glucose: steady-state
G1-switchers: switch cell cycle
G1-switchers: cycle after switch cell cycle
S/G2/M-switchers: switch cell cycle
S/G2/M-switchers: cycle after switch cell cycle
Glycerol-ethanol: steady-state
Volume at phase end (fL)
0
100
200
300
400
G1
S/G2/M

Figure 21: The nutrient switch leads to cell cycle arrests in *switchers* and leads to stronger cell enlargement in *bck2Δ* cells. (**A**) Schematic explanation for cell categories analysed in this figure. (**B**) Phase lengths are plotted for *switchers' switch cell cycles* (yellow) and *cell cycles after switch-cell-cycle* (green). x symbol represents the mean phase length of the population. The outermost left and right panels show steady-state phase lengths for SCD and SCGE, respectively. Complete cell cycles were pooled from two independent steady-state experiments for each growth medium. The number of cells in each box in the steady-state panels is between 450 and 950. For the nutrient switch panels (yellow and green), cells were pooled from three independent experiments. For *G1-switchers' switch cell cycle* G1 phase (yellow, left), n_{WT} = 144, $n_{whi5\Delta}$ = 59, $n_{bck2\Delta}$ = 67, $n_{whi5\Delta bck2\Delta}$ = 50. For *G1-switchers' switch cell cycle* S/G2/M phase (yellow, left), n_{WT} = 132, $n_{whi5\Delta}$ = 46, $n_{bck2\Delta}$ = 56, $n_{whi5\Delta bck2\Delta}$ = 42. For *S/G2/M-switchers' switch cell cycle* G1 phase (yellow, right), n_{WT} = 239, $n_{whi5\Delta}$ = 107, $n_{bck2\Delta}$ = 116, $n_{whi5\Delta bck2\Delta}$ = 115. For *S/G2/M-switchers' switch cell cycle* S/G2/M phase (yellow, right), n_{WT} = 197, $n_{whi5\Delta}$ = 66, $n_{bck2\Delta}$ = 66, $n_{whi5\Delta bck2\Delta}$ = 94. For *G1-switchers' cell cycle after switch-cell-cycle* G1 phase (green, left), n_{WT} = 120, $n_{whi5\Delta}$ = 34, $n_{bck2\Delta}$ = 49, $n_{whi5\Delta bck2\Delta}$ = 34. For *G1-switchers' cell cycle after switch-cell-cycle* S/G2/M phase (green, left), n_{WT} = 91, $n_{whi5\Delta}$ = 14, $n_{bck2\Delta}$ = 39, $n_{whi5\Delta bck2\Delta}$ = 26. For *S/G2/M-switchers' cell cycle after switch-cell-cycle* G1 phase (green, right), n_{WT} = 164, $n_{whi5\Delta}$ = 47, $n_{bck2\Delta}$ = 51, $n_{whi5\Delta bck2\Delta}$ = 61. For *S/G2/M-switchers' cell cycle after switch-cell-cycle* S/G2/M phase (green, right), n_{WT} = 138, $n_{whi5\Delta}$ = 45, $n_{bck2\Delta}$ = 29, $n_{whi5\Delta bck2\Delta}$ = 46. Strain order in each panel (L-R): WT, *whi5Δ*, *bck2Δ*, *whi5Δbck2Δ*. (**C**) This dataset is also used to plot cell volume at the end of the respective cell cycle phases (fL). Cell volume at the end of G1 is the cell volume at the last frame before bud emergence. Cell volume at the end of S/G2/M is a sum of mother and bud volume at the last frame before division. Strain order in each panel (L-R): WT, *whi5Δ*, *bck2Δ*, *whi5Δbck2Δ*. Independent two-tailed t-tests with the assumption of unequal variances (Welch's t-tests) were used for statistical analyses.

switchers: the *switch-cell-cycle* (Fig. 21A, highlighted in yellow) and the *cell-cycle-after-switch-cell-cycle* (Fig. 21A, highlighted in green). For comparison of cell cycle properties during the lag phase after the nutrient switch to those from the log phase in steady-state, the same cell cycle properties from the steady-state dataset were plotted on the left and right of the nutrient switch data (Fig. 21B-C). Both the *G1-switchers* and the *S/G2/M-switchers* arrested in the cell cycle phase that was ongoing at the time of the nutrient switch. This is evident from the elongated G1 phase of the *G1-switchers* and the elongated S/G2/M-phase of the *S/G2/M-switchers* in the *switch cycle* (Fig. 21B, yellow). For the *G1-switchers*, the next phase after the arrest, which was the S/G2/M-phase of the *switch cycle* (Fig. 21B, yellow) was not very different in length from the S/G2/M-phases observed in exponential growth in SCGE (Fig. 21B, extreme right panel). Similarly, the phase lengths in the next cell cycle of *G1-switchers* (*cell-cycle-after-switch-cell-cycle*, Fig. 21B, left green) largely resembled exponential growth in SCGE. Conversely, *S/G2/M-switchers* experienced another arrest in the strongly elongated G1 phase of their next cell cycles before undergoing a relatively unperturbed S/G2/M-phase (Fig. 21B, *cell-cycle-after-switch-cell-cycle*, right green). This observation indicated that while *G1-switchers* only underwent the single G1-arrest in the *switch-cycle*, *S/G2/M-switchers* arrested twice: once in the S/G2/M-phase of the *switch cycle* and then again in the G1-phase of the *cell-cycle-after-switch-cell-cycle*. Thus, the *S/G2/M-switchers* exhibited memory of the nutrient-switch in the cell cycle following the *switch-cell-cycle*. Moreover, of the four strains studied, two strains appeared to have longer G1-arrests than others: *bck2Δ and whi5Δbck2Δ* (Fig. 21B), indicating that Bck2 is involved in exit from these G1-arrests.

A consequential question was how these cell cycle arrests affected cell volume. To address this question, cell volume at the end of these cell cycle phases was plotted in Figure 21C. In *G1-switchers*, the G1 arrest immediately after the nutrient switch led to an increased cell volume at the end of G1 in all the strains (Fig. 21C, left yellow). Despite being relatively short, the following G1 slightly increased cell volume further (Fig. 21C, left green). At the end of the G1 arrest of the *G1-switchers*, strains with *BCK2* deletions exhibited stronger cellular enlargement as compared to WT and *whi5Δ* (Fig. 21C, left yellow). This could be a result of the longer G1 arrests that these strains experienced (Fig. 21B, left yellow). Moreover, this single G1 arrest was sufficient to lead to a cell volume difference between WT *G1-switchers* and *whi5Δbck2Δ G1-switchers*, which had in steady state looked very similar in cell volume at G1 end (Fig. 21B, extreme left panel). For *S/G2/M-switchers*, the S/G2/M arrest in the *switch-cell-cycle* led to increased cell volumes for all strains (Fig. 21C, right yellow) which were further increased by the G1 arrest in the *cell-cycle-after-switch-cell-cycle* (Fig. 21C, right green). Also for the *S/G2/M-switchers*, the G1-arrest in the *cell-cycle-after-switch-cell-cycle* led to a prominent cell volume difference between WT and *whi5Δbck2Δ* cells (Fig. 21C, right green). *whi5Δbck2Δ* cells resembled *bck2Δ* cells rather than WT cells after the G1-arrests. Like *bck2Δ* cells, they underwent longer G1 arrests and ended up with bigger cell volumes, which indicates an increased importance of Bck2 in G1 exit after a nutrient switch. The post-switch cell cycle arrests and consequential increase in cell volumes for WT and *whi5Δbck2Δ* cells were also consistent with the increase in mean cell volume and the arrests observed in the bulk nutrient switch experiments (Fig. 18).

3.11. Nutrient switch-facing buds also arrest in their first G1 and *bck2Δ* mutants undergo stronger cell enlargement during these arrests.

So far, it was evident that among the *switchers*, strains that had a *BCK2* deletion underwent longer G1 arrests and more cellular overgrowth after the nutrient switch. Apart from the *switchers*, there was one other category of cells that also faced the nutrient-switch: the *first round of daughters of S/G2/M-switchers* (Fig. 22A, highlighted in blue, cell number 1) that were present as buds of *S/G2/M-switchers* at the time of the nutrient switch. The *first round of daughters of G1-switchers,* on the other hand, only started budding after the nutrient switch. It was therefore important to check whether the *first round of daughters of S/G2/M-switchers* also experienced cell cycle arrests after the nutrient switch and if so, whether the arrest and overgrowth phenotypes for this category of cells were also stronger in strains with *BCK2* deletions.

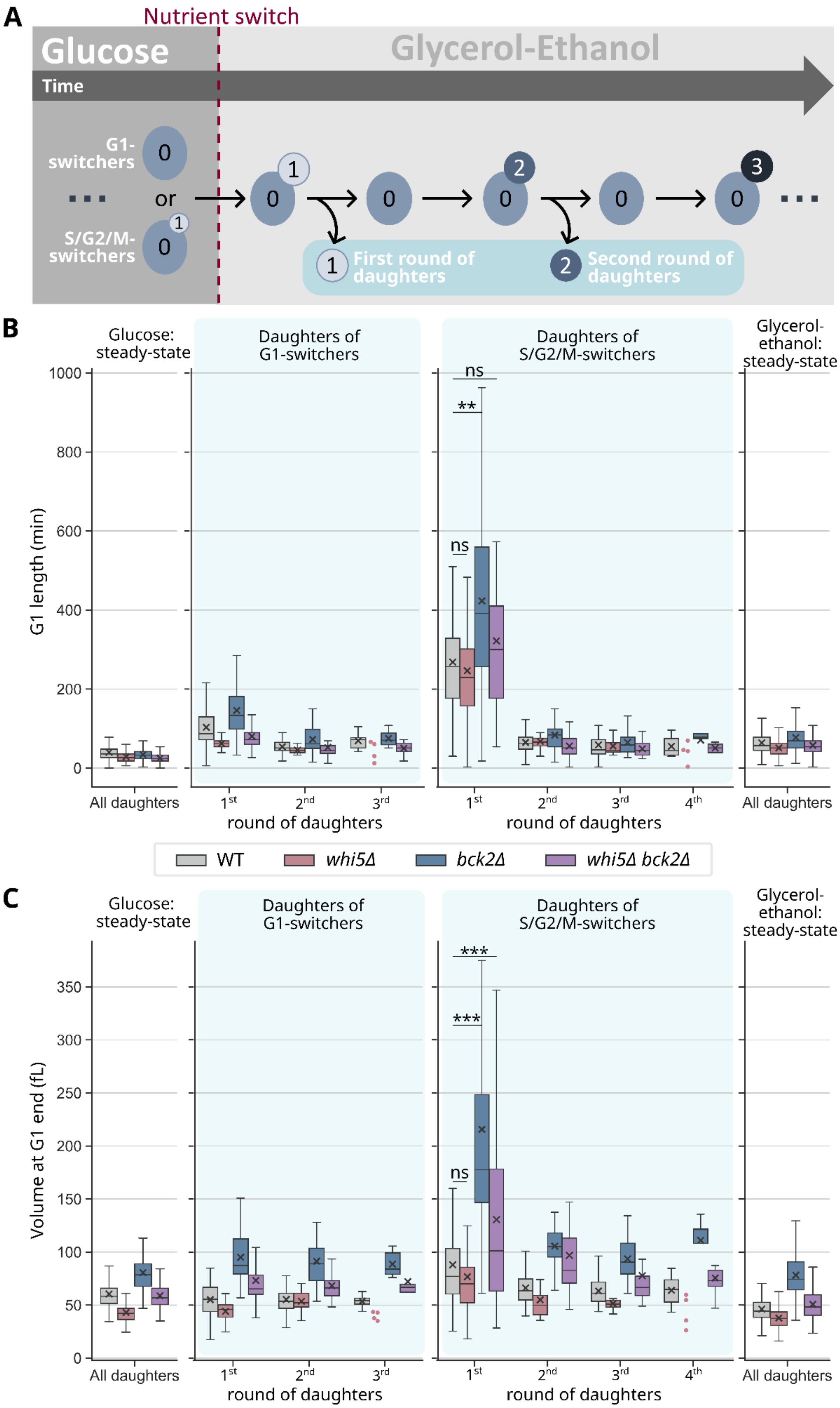
A
Nutrient switch
Glucose
Glycerol-Ethanol
Time
G1-switchers
or
S/G2/M-switchers
0
1
2
3
First round of daughters
Second round of daughters
B
Glucose: steady-state
Daughters of G1-switchers
Daughters of S/G2/M-switchers
Glycerol-ethanol: steady-state
G1 length (min)
1000
800
600
400
200
0
ns
**
ns
All daughters
1st
2nd
3rd
4th
round of daughters
WT
whi5Δ
bck2Δ
whi5Δ bck2Δ
C
Volume at G1 end (fL)
350
300
250
200
150
100
50
0
***
***
ns

Figure 22: Nutrient-switch-facing buds arrest in their first G1, leading to stronger enlargement in *bck2Δ* cells. (**A**) A schematic explanation for cell populations analysed in this figure. (**B**) G1 lengths are plotted for the *rounds of daughters* (blue) of *G1-switchers* and *S/G2/M-switchers*. x symbol represents the mean phase length of the population. The outermost left and right panels show steady-state phase lengths for SCD and SCGE, respectively. Complete cell cycles of daughter cells were pooled from two independent steady-state experiments for each growth medium. The number of cells in each box in the steady-state panels is between 198 and 330. For the nutrient switch panels (blue), cells were pooled from three independent experiments. For the *first round of daughters of G1-switchers*, n_{WT} = 103, $n_{whi5\Delta}$ = 21, $n_{bck2\Delta}$ = 48, $n_{whi5\Delta bck2\Delta}$ = 33. For the *first round of daughters of S/G2/M-switchers*, n_{WT} = 123, $n_{whi5\Delta}$ = 40, $n_{bck2\Delta}$ = 34, $n_{whi5\Delta bck2\Delta}$ = 50. The following *rounds of daughters* had fewer cells than the first *round*. For categories that include less than 5 cells, the individual data points are shown as a scatter. Strain order in each panel (L-R): WT, *whi5Δ*, *bck2Δ*, *whi5Δbck2Δ*. (**C**) The same dataset was also used to determine cell volume at the end of the G1 (fL). Strain order in each panel (L-R): WT, *whi5Δ*, *bck2Δ*, *whi5Δbck2Δ*. Independent two-tailed t-tests with the assumption of unequal variances (Welch's t-tests) were used for statistical analyses.

Indeed, the *first round of daughters of S/G2/M-switchers* experienced an arrest during their first G1, which is evident from the 3- to 4-fold longer G1 duration (Fig. 22B). Conversely, daughters born in the next rounds and those of *G1-switchers* showed G1 durations more similar to steady-state growth on SCGE (Fig. 22B), indicating that this G1 arrest was unique to the cells that were present at the time of the nutrient switch, i.e., the *first round of daughters of S/G2/M-switchers*. Like for the *switchers*, the duration of the G1 arrest in the *first round of daughters of S/G2/M-switchers* was longer in *bck2Δ* mutant strains as compared to the others (Fig. 22B). Consequently, cells of all strains in this category were bigger at G1 end but significantly stronger enlargement was observed in *bck2Δ* and *whi5Δbck2Δ* cells as compared to the other strains (Fig. 22C). Taken together with the results from Figure 21, this data indicated that cells that faced the switch in S/G2/M, either as mother or bud, carried the memory of the switch into the next cell cycle and the next G1 was prolonged. To better understand the effect of these arrests on size homeostasis efficiency and to overcome the hurdle of cell numbers being too low for a robust CV calculation, the dependence of G1 duration on birth volume was assessed for the various *rounds of daughters of S/G2/M-switchers*.

3.12. The *first daughters of S/G2/M-switchers* have disrupted cell size homeostasis at the G1/S transition (WT).

To assess the strength of size homeostasis at the G1/S transition in the *rounds of daughters of S/G2/M switchers*, the dependence of the growth-rate adjusted G1 duration on cell volume at birth was calculated through linear regression (Fig. 23), as described in detail in section 3.6[70]. As a reference, this linear regression was also performed for daughter cells from steady state data in SCD and SCGE (Fig. 23). The slopes were obtained from the equations for the resulting regression lines. Steady-state daughters of all strains had negative slopes and therefore intact size homeostasis in both growth media (Fig. 23). For WT and *whi5Δbck2Δ* cells, the *first round of daughters of S/G2/M switchers*, which was known to arrest during G1 (Fig. 22), exhibited a slope close to 0, indicating disrupted G1/S size homeostasis. This strong disruption of G1/S size homeostasis was only observed in the *first round of daughters* and the following *rounds of daughters* showed a more recovered homeostasis strength. In contrast, for *whi5Δ* and *bck2Δ* cells, G1/S size homeostasis got stronger in the *first round of daughters of S/G2/M-switchers*, before returning to slopes closer to steady-state slopes over the following *rounds of daughters*. These increases in the size homeostasis strengths of *first daughters* of *whi5Δ* and *bck2Δ* strains are difficult to confirm or interpret given the low cell numbers in each category. However, at least for WT cells, it was clear that the G1 arrest observed in the *first round of daughters of S/G2/M switchers* led to a disruption of G1/S size homeostasis. This disrupted G1/S size homeostasis supports the increased CV of cell volume that was observed after the nutrient switch in the bulk experiment (Fig.18).

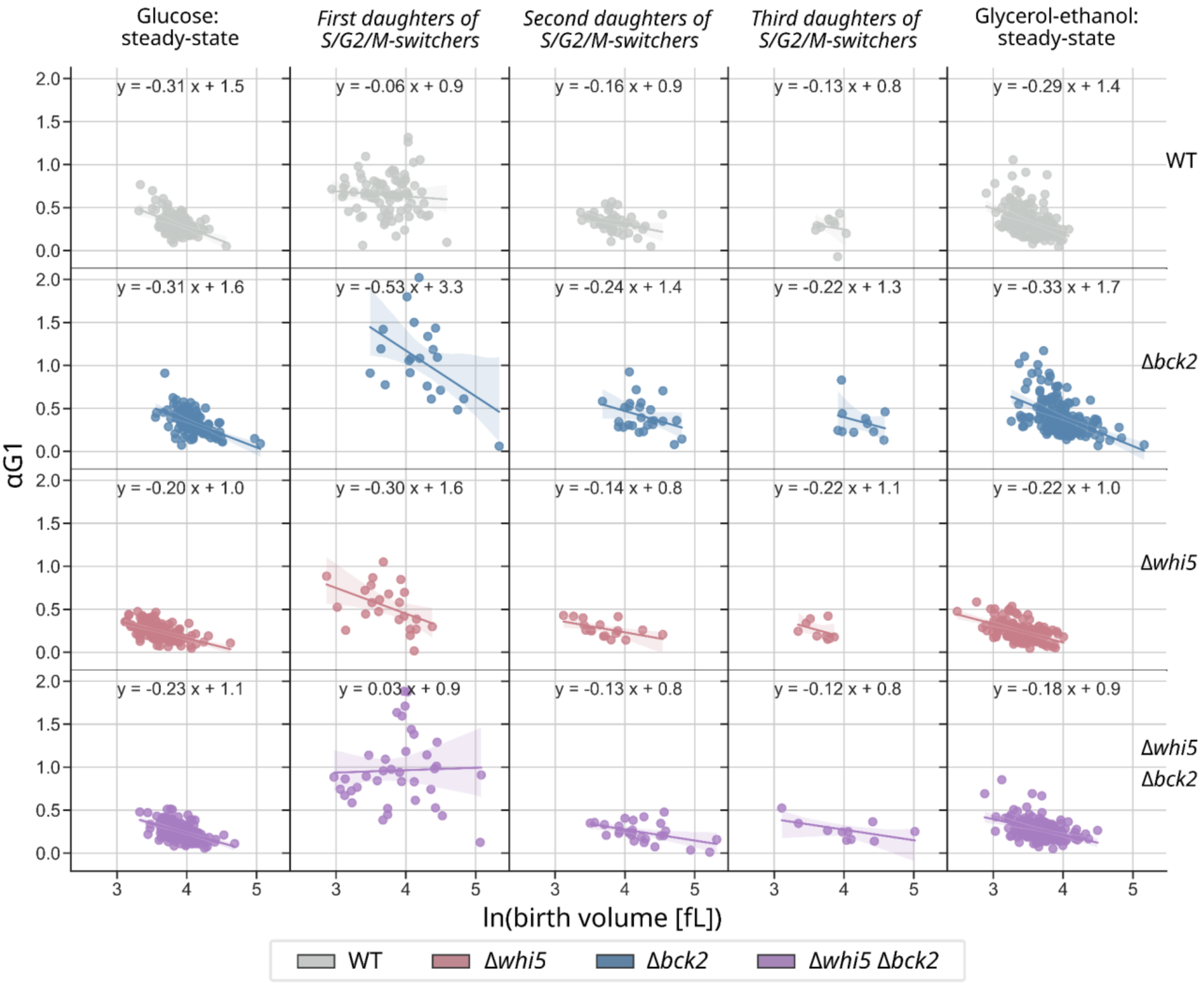

Figure 23: WT *first daughters of S/G2/M switchers* have weaker cell size homeostasis at the G1/S transition. The strength of size homeostasis at the G1/S transition in different cell categories is assessed as per the method described by Di Talia et al.[70]. The growth rate for exponentially growing cells, α, is the slope of the natural logarithm (in [fL]) of cell volume plotted against time. For each cell, G1 length is multiplied by α to obtain a growth rate adjusted G1-duration, αG1. αG1 is plotted against the natural logarithm of birth volume and a linear regression is performed. A more negative slope of the resulting regression line indicates stronger cell size homeostasis, whereas a slope closer to 0 indicates weaker cell size homeostasis. Shaded areas show 95% confidence intervals. The outermost left and outermost right panels show steady-state daughters growing in SCD and SCGE respectively and the three panels in the middle show the *rounds of daughters of S/G2/M*

switchers. The *first daughters of S/G2/M switchers* were pooled from three independent nutrient switch experiments. Steady-state daughters were pooled from two independent experiments.

3.13. *First daughters of S/G2/M switchers* arrest in pre-start G1

To further characterise the G1 arrest observed in the *first daughters of S/G2/M switchers*, and in particular to ascertain at what point in G1 these cells arrest, a cell cycle reporter strain was constructed that allowed the resolution of the cell cycle into more specific cell cycle phases than just G1 and S/G2/M. An mCitrine-tagged mutant *WHI5* allele, *WHI5-WIQ*, was integrated into the *URA3* locus while the endogenous *WHI5* gene remained unmodified. The Whi5-WIQ protein is a loss-of-function mutant that does not bind SBF[137] i.e., it cannot inhibit the G1/S transition. However, it retains its ability to localise to the nucleus in a cell-cycle-dependent manner, which could be visualised with the mCitrine tag (Fig. 24). Additionally, the histone Htb2 was tagged with the fluorescent protein mScarlet-I in the same strain (Fig. 24). The deletions of interest (*Δwhi5*, *Δbck2*, and *Δwhi5Δbck2*) were introduced into this cell cycle-reporter strain and the live-cell microscopy experiment with the nutrient switch was performed. Having a fluorescently tagged histone (Htb2) signal allowed visualisation of the nucleus and thereby enabled the segmentation of a nuclear mask. Subtracting the nuclear mask from the cellular mask resulted in a cytoplasmic mask. Thus, Whi5-WIQ-mCitrine and Htb2-mScarlet-I fluorescence could be quantified in three compartments: the nucleus, the cytoplasm and the whole cell. This compartmentalisation of the two fluorescence signals was then used to identify the specific cell cycle phase of the cell.

Whi5 is known to localise in the nucleus between telophase and *Start*, while CDK activity is low[90]. If the nuclear concentration of Whi5-WIQ-mCitrine is plotted against time relative to bud emergence for one example cell (Fig. 24, yellow trace), Whi5-WIQ indeed appears to be nuclear at the beginning of G1. At *Start*, Whi5-WIQ is rapidly exported from the nucleus. Thus, *Start* was annotated as the frame at which 50% of Whi5-WIQ was exported from the nucleus[83] (Fig. 24). The annotation of *Start* split G1 into pre-*Start* and post-*Start* G1. The trace of the Htb2-mScarlet-I amount in the bud (Fig. 24, red trace) was used to determine when the dividing nucleus entered the bud, which occurs during anaphase in mitosis[138]. The time of entry of the dividing nucleus into the bud was labelled as the start of anaphase. The time between bud emergence and the start of anaphase was labelled as pre-anaphasic (Fig. 24). The end of anaphase was annotated by using the nuclear Whi5-WIQ-mCitrine concentration. The frame at which the nuclear concentration of Whi5-WIQ-mCitrine began to increase towards the end of the cell-cycle indicated the nuclear re-import of Whi5-WIQ and was annotated as the start of telophase[90]. (Fig. 24, yellow trace). This frame and all subsequent frames were labelled as post-anaphasic (Fig. 24). More details on the method used for cell cycle phase categorisation are available in section 2.18.3.3.

This cell cycle phase classification was applied to the G1 phases of the *first round of daughters of S/G2/M-switchers* as these cells had previously been shown to undergo long G1 arrests in their first cell cycles (Fig. 22). The first cell cycles of these cells were aligned at bud emergence and the pre-

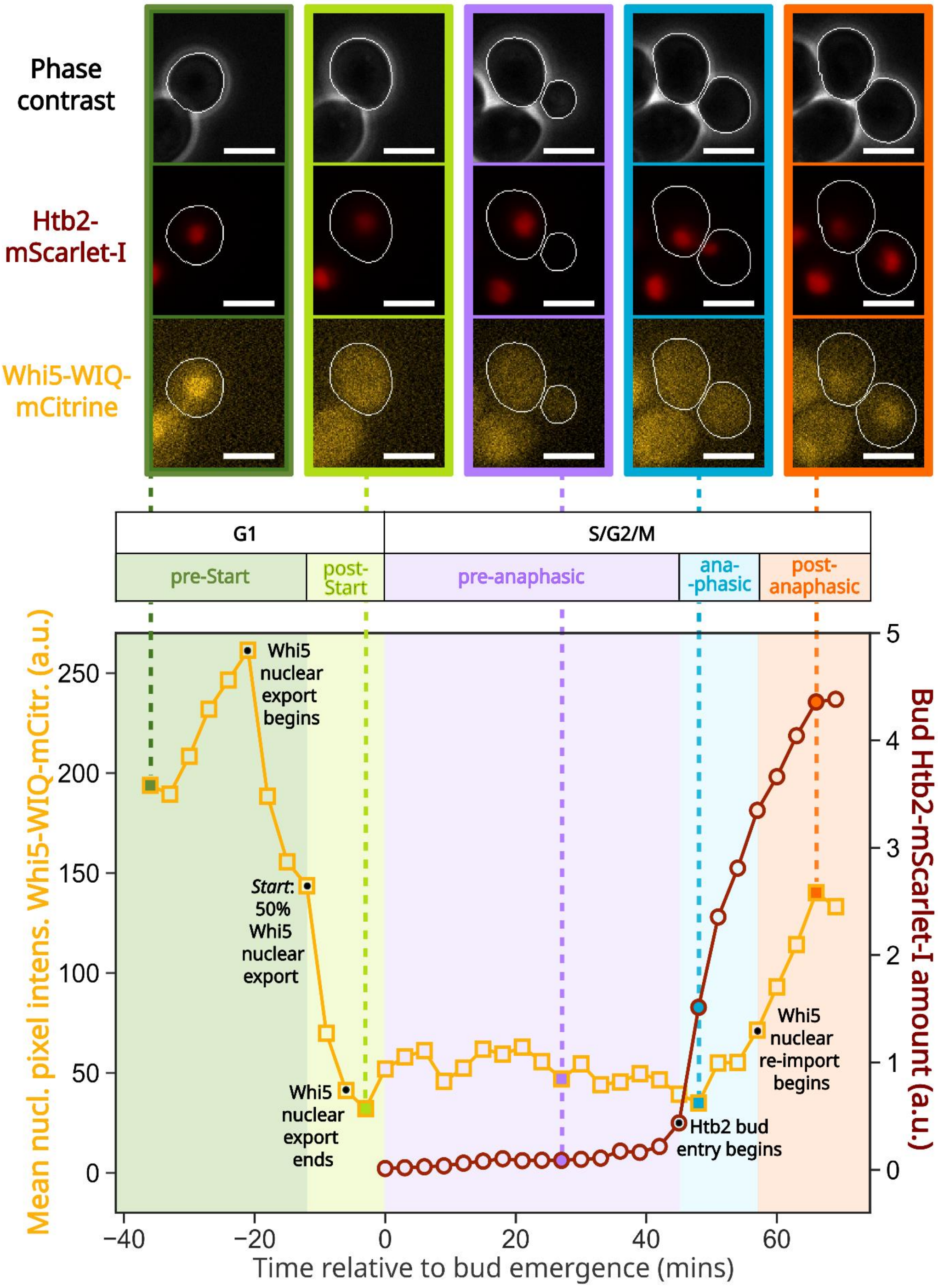

Figure 24: Cell cycle categorisation using a cell cycle reporter strain. (**A**) An example of cell cycle phase resolution for a steady-state (SCD) wild type cell based on two fluorescent signals: mean nuclear pixel intensity of Whi5-WIQ-mCitrine (yellow trace, a.u.) and bud Htb2-mScarlet-I amount (red trace, a.u.), both plotted against time relative to bud emergence. Black dots indicate events that were used for cell cycle categorisation. 50% Whi5-WIQ-mCitrine nuclear exit is annotated as *Start*. Entry of Htb2-mScarlet-I into the bud is labelled as the start of anaphase. Re-import of Whi5-WIQ-mCitrine into the nucleus marks the end of anaphase. Dotted lines connect example images to the time-point at which they were acquired. Example images show cells in phase contrast (grey), histone Htb2 tagged with mScarlet-I (red) and Whi5-WIQ tagged with mCitrine (yellow). Cell contours generated with YeaZ in the Cell-ACDC pipeline are shown in white. Scale bars represent 4 µm.

Start G1, post-*Start* G1 and S/G2/M phases were plotted (Fig. 25A). The G1 arrest observed in the *first round of daughters of S/G2/M-switchers* was found to occur predominantly in pre-Start G1 (Fig 25A, dark green areas, Fig. 25B), whereas post-*Start* G1 durations appeared much shorter (Fig 25A, light green areas, Fig. 25B). Quantification of pre- and post-*Start* durations revealed that pre-Start G1 durations were longer for *bck2Δ* and *whi5Δbck2Δ* cells as compared to wild type and *whi5Δ* cells (Fig. 25B). These longer pre-*Start* arrests in the *bck2Δ* and *whi5Δbck2Δ* strains emphasize the importance of Bck2 in *Start* induction after a change in nutrient conditions. Furthermore, the fluorescent cell cycle reporters could be used to study whether the duration of the G1 arrest of the *first daughters of S/G2/M-switchers* depended on the specific cell cycle stage of their mothers, the *S/G2/M-switchers*, at the time of the nutrient switch.

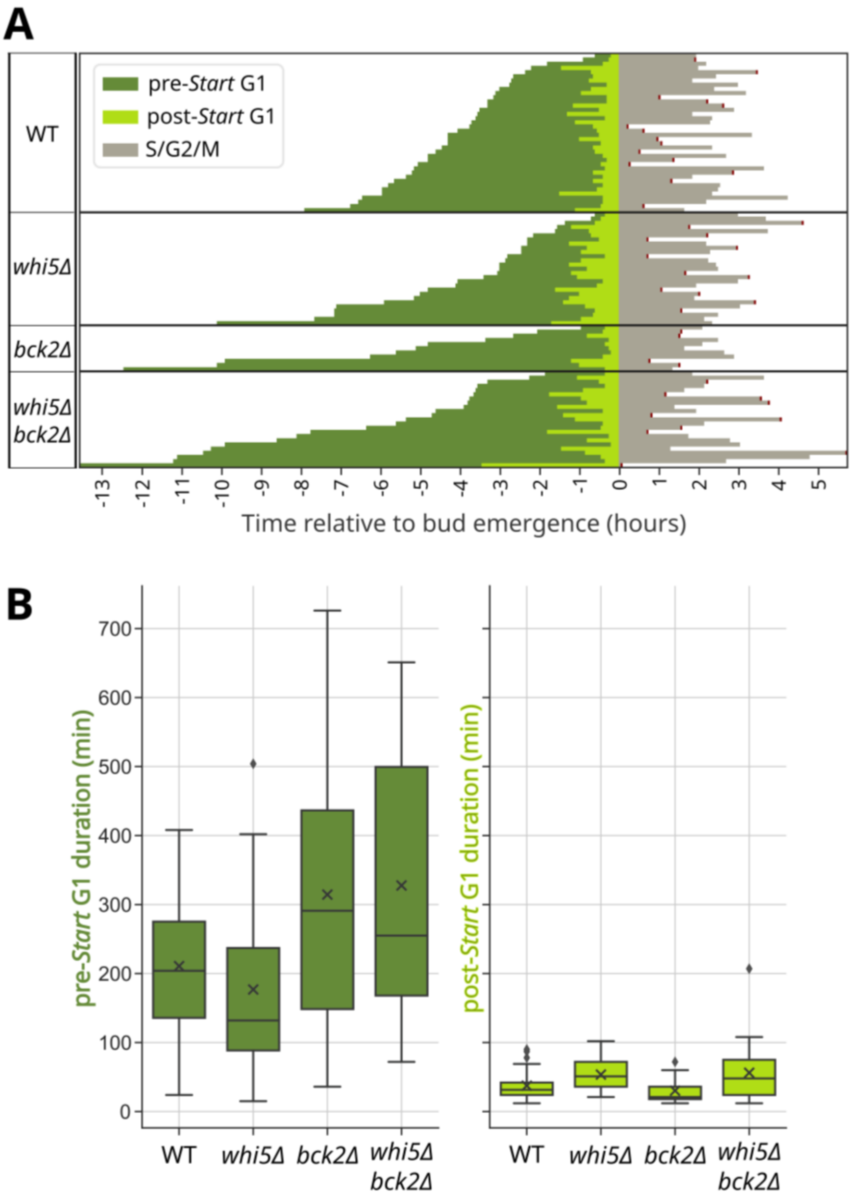

Figure 25: *First daughters* of *S/G2/M-switchers* arrest mainly in pre-*Start* G1. (**A**) Cell cycles of *first daughters of S/G2/M-switchers* with complete G1 phases were resolved into pre-*Start* G1 (dark green), post-*Start* G1 (light green) and S/G2/M (grey). A categorical heatmap shows cell cycle phases of single cells plotted against time relative to bud emergence. Each row represents a single cell. Incomplete S/G2/M phases are capped with red ends. Black horizontal lines separate cells of different strains. (**B**) A quantification of pre-*Start* and post-*Start* G1 durations is shown here as a box-plot. x symbol shows the mean phase duration of the

population. Data was pooled from two independent experiments of live-cell microscopy coupled to a nutrient switch. $n_{WT} = 38$, $n_{whi5\Delta} = 27$, $n_{bck2\Delta} = 11$, $n_{whi5\Delta bck2\Delta} = 23$.

3.14. Among the *first daughters of S/G2/M switchers*, the strongest arrest phenotypes were observed for *bck2Δ* cells whose mothers were post-anaphasic at the time of the nutrient switch.

The long G1 arrests observed in the *first round of daughters of S/G2/M-switchers* raised the question of whether the severity of these arrests was dependent on the specific cell cycle phase of the mother *S/G2/M-switcher* at the time of the nutrient switch. To address this question, the *first round of daughters of S/G2/M-switchers* were categorised based on whether the mother was pre-anaphasic, anaphasic or post-anaphasic at the time of nutrient switch. The specific cell cycle categorisation needed for this analysis was performed manually for one cell category of interest - the *first round of daughters of S/G2/M-switchers*. However, data from the cell cycle reporter strains is available for cell cycle categorisation of other cell categories in the future. The corresponding G1-lengths for the *first round of daughters of S/G2/M-switchers* categorised based on the mother's cell cycle stage at the time of nutrient switch are plotted in Figure 26A. Calculation of the length of a cell cycle phase requires that the phase ends during the course of the experiment. Therefore, Figure 26A only shows the G1 lengths of *first daughters of S/G2/M-switchers* that completed G1 before the end of the experiment. A significant portion of the *first daughters of S/G2/M-switchers* did not complete G1 during the experiment i.e., remained arrested in G1 until the end of the experiment (Fig. 26B). This dramatic arrest phenotype was observed in the majority of *bck2Δ* and *whi5Δbck2Δ first daughters* (Fig. 26B). Of the portion that did complete G1 (Fig. 26A), the longest G1 lengths and therefore the strongest arrests were observed for the *whi5Δbck2Δ* cells whose mothers were post-anaphasic at the time of nutrient switch (Fig. 26A). Strikingly, none of the *bck2Δ* cells whose mothers were post-anaphasic at the time of nutrient switch completed G1 during the experiment (Fig. 26A). All of these daughters stayed arrested in G1 until the end of the experiment (Fig. 26A-B). Additionally, it was checked that these differences in the fractions of cells that complete G1 during the experiment are not an artefact of differences in the duration of experiments analysed for each strain. Altogether, this data suggests that Bck2 has a nutrient switch-specific function after anaphase which affects the induction of *Start* in the next generation. Bastajian *et al*.[80] have previously proposed such a role for Bck2, where it may be involved in integrating environmental information into the cell cycle progression decision at multiple cell cycle-phase transitions, including M/G1. They showed that Bck2 promotes cell cycle progression through *Start* by promoting the expression of Cln3, Swi4 and Cln2[80]. The G1/S activator Cln3 is a short-lived protein and known to be depleted after a switch from a rich to a poor carbon source[89]. Moreover, a double deletion of *cln3Δ* and *bck2Δ* is lethal due to permanent G1 arrest[95]. Given this information, one possible explanation for the extended G1 arrests observed in Bck2 deletion mutants could be a post-switch Cln3 depletion, which, coupled with the absence of Bck2, temporarily mimics a *cln3Δbck2Δ* phenotype.

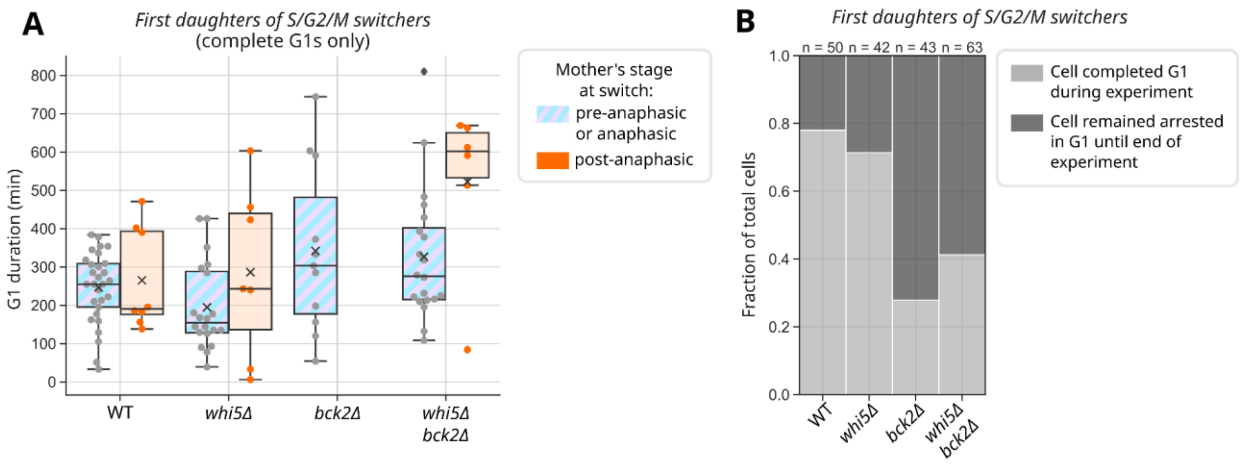

Figure 26: In *bck2Δ* mutants, the strongest arrest phenotypes are observed in first daughters whose mothers faced the nutrient switch after anaphase. (**A**) The *first daughters of S/G2/M-switchers* are further categorised based on their mothers' cell cycle phase at the time of nutrient switch: pre-anaphasic or anaphasic (purple and blue striped) or post-anaphasic (orange). The x symbol shows the mean phase duration of the population. (**B**) The fraction of *first daughters of S/G2/M-switchers* that complete G1 during the experiment (light-grey) and those that stay arrested in G1 until the end of the experiment (cells with incomplete G1 phases, dark-grey) are plotted. Incomplete G1 phases are G1 phases interrupted by the end of imaging in the experiment and not by death or exclusion of cells from the analysis.

3.15. Whi5 is reimported into the nucleus upon nutrient switch

An advantage of having the mCitrine tagged Whi5-WIQ protein was the ability to visualise if the nutrient switch affected Whi5 cellular localisation. Irvali *et al.*[108] have shown that unfavourable nutrient conditions can cause post-*Start* cells to re-import Whi5 into the nucleus, indicating that cells prefer to be in a pre-*Start* like state during depleted nutrient conditions. In agreement with this, our results show that the *first round of daughters of S/G2/M-switchers* also arrest in pre-Start G1 (Fig. 25A-B). However, since the *first round of daughters of S/G2/M-switchers* do not face the nutrient switch during their first G1, it is important to study the *switch-cell-cycles* of the *switchers* to observe the effect of the nutrient switch on Whi5-WIQ localisation. Hence, the nuclear Whi5-WIQ-mCitrine concentration during the *switch-cell-cycles* of both populations of *switchers* is depicted as a heatmap (Fig. 27). Each row in the heatmap is a unique complete cell cycle during which the nutrient switch occurred. The time points in the cell cycles have been recalculated relative to the time of the nutrient switch (time point 0) and have been scaled between -1 and 1. Since the pre-switch and post-switch durations of the experiment were very different, the density of time points after the switch is much higher than that of the time points before the switch. Moreover, since cell cycle durations varied between cells but were scaled between -1 and 1, the resolution on the x-axis varies from cell to cell.

For the *G1-switchers*, varying concentrations of Whi5-WIQ were observed in the nucleus before the switch for most cells, indicating that the cells had progressed to different extents through G1. Most cells showed some amount of Whi5-WIQ signal in the nucleus and were therefore likely pre-*Start* at the time of the switch. Some cells showed almost no Whi5-WIQ in the nucleus at the time of the switch and were likely post-*Start*. Regardless of the specific G1 phase at the time of the nutrient switch, all *G1-switchers* re-imported Whi5-WIQ into the nucleus immediately after the switch. After the switch they eventually passed *Start* when Whi5-WIQ almost entirely exited the nucleus. Whi5-WIQ re-entered the nucleus just before the end of the cell-cycle in telophase, as expected. *bck2Δ G1-switchers* appeared to have delayed G1 exit and S-phase entry as compared to the other strains,

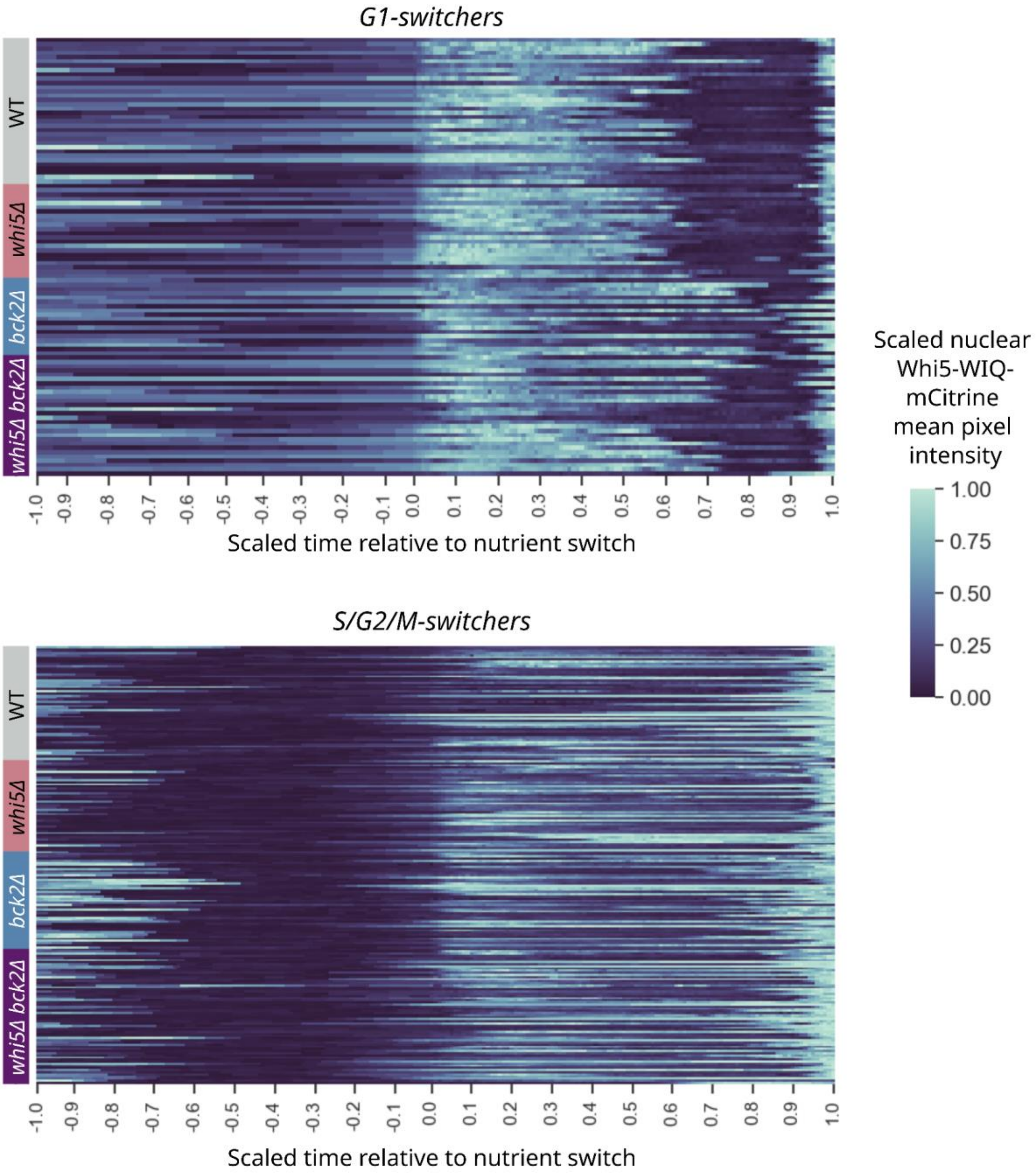

Figure 27: *Switchers* re-import Whi5-WIQ-mCitrine into the nucleus after the nutrient switch. Whi5-WIQ-mCitrine mean pixel intensity in the nucleus was scaled between 0 and 1 for every *switcher* that completed its *switch cell cycle*. For each of these cells, the time spent in the cell cycle relative to the nutrient switch was

calculated and scaled between -1and 1, with 0 being the time of the nutrient switch. The scaled nuclear Whi5-WIQ-mCitrine mean pixel intensity was plotted against the scaled time relative to the nutrient switch for G1-switchers (top) and S/G2/M-switchers (bottom). Each row represents a unique cell. Coloured bars on the left indicate which strain the cells belong to.

supporting the theory that Bck2's role in *Start* induction becomes more important after the nutrient switch. *S/G2/M-switchers* showed presence of nuclear Whi5-WIQ during early G1 and a complete Whi5-WIQ nuclear exit before the nutrient switch, indicating that the cells were past the G1/S transition at the time of the switch. Similar to *G1-switchers*, they also partially re-imported Whi5-WIQ into the nucleus immediately after the switch. Like *G1-switchers*, *S/G2/M-switchers* showed a peak in nuclear Whi5-WIQ concentration at the end of the *switch-cell-cycle*, likely corresponding to Whi5-WIQ re-entry into the nucleus during telophase. Altogether, these data suggest that the nuclear localisation of Whi5 is indeed nutrient dependent, and the regulation of this localisation is likely downstream of nutrient sensing machinery. These results confirm that a shift from rich to poor growth media leads to a re-entry of Whi5 into the nucleus in most cells.

3.16. The size phenotypes of *whi5Δ*, *bck2Δ* and *cln3Δ* are additive.

Given that Bck2 and Cln3 both activate the G1/S transition, and that one hypothesis for the strong post-switch G1 arrests in *bck2Δ* cells is the depletion of Cln3, understanding Bck2's post-switch role required a characterisation of the *CLN3* deletion in steady-state and changing nutrients. It is known from bulk studies that the *bck2Δ* and *cln3Δ* deletions lead to increased cell volumes in steady-state

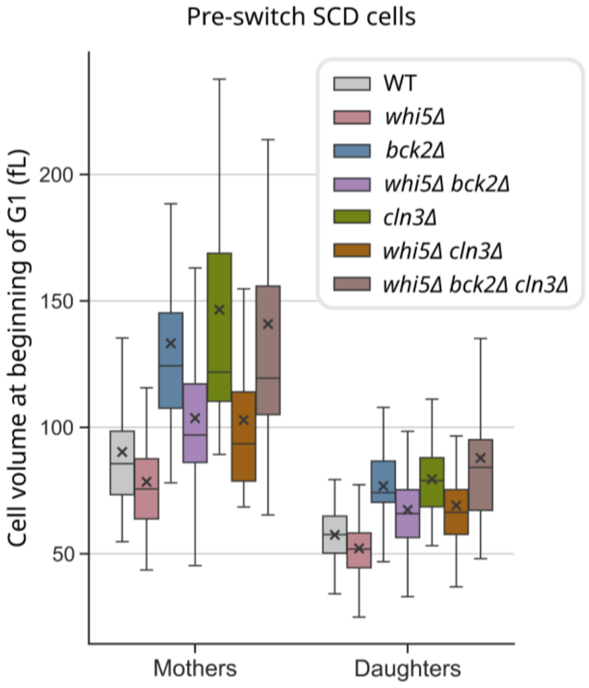

Figure 28: The size phenotypes of *whi5Δ*, *bck2Δ* and *cln3Δ* are additive. Cell volume at the first frame of G1 is plotted for daughter (generation = 1) and mother (generation>1) cells of different strains growing exponentially before the nutrient switch. Steady-state pre-switch cells are pooled from at least two independent experiments of live cell microscopy coupled to the nutrient switch. x symbol represents the mean cell volume (fL) at the beginning of G1. For daughters, n_{WT} = 164, $n_{whi5\Delta}$ = 82, $n_{bck2\Delta}$ = 73, $n_{whi5\Delta bck2\Delta}$ = 77, $n_{cln3\Delta}$ = 44, $n_{whi5\Delta cln3\Delta}$ = 55, $n_{whi5\Delta bck2\Delta cln3\Delta}$ = 37. For mothers, n_{WT} = 209, $n_{whi5\Delta}$ = 87, $n_{bck2\Delta}$ = 95, $n_{whi5\Delta bck2\Delta}$ = 95, $n_{cln3\Delta}$ = 48, $n_{whi5\Delta cln3\Delta}$ = 61, $n_{whi5\Delta bck2\Delta cln3\Delta}$ = 34. Strain order (L-R): WT, *whi5Δ*, *bck2Δ*, *whi5Δbck2Δ*, *cln3Δ*, *whi5Δcln3Δ*, *whi5Δbck2Δcln3Δ*.

conditions[77]. This study's live-cell microscopy experiments could reproduce these results at the single-cell level. During steady-state growth in SCD, *cln3Δ* cells were indeed larger than wild-type cells, similar to *bck2Δ* (Fig. 28). As expected[77], an additional deletion of *WHI5* partially rescued the large cell phenotypes of both *bck2Δ* and *cln3Δ* (Fig. 28). While the *bck2Δcln3Δ* double deletion is inviable, an additional deletion of *WHI5* is known to rescue this lethality[77]. The hence viable *whi5Δbck2Δcln3Δ* triple deletion is similar to the *bck2Δ* and *cln3Δ* single deletions in size (Fig. 28), highlighting that the effects of the Whi5, Bck2 and Cln3 deletions are additive. The next task was the characterisation of the *cln3Δ*, *whi5Δcln3Δ* and *whi5Δbck2Δcln3Δ* phenotypes after a nutrient switch. If the nutrient switch indeed leads to a Cln3 depletion as described by Sommer *et al*.[89], Cln3 would be expected to be dispensable for cell size adaptation after the switch. By that logic, a *CLN3* deletion would not be expected to cause as strong an arrest phenotype as *bck2Δ*.

3.17. Bck2 plays a more important role than Cln3 in cell size adaptation following a nutrient switch.

A nutrient switch experiment with *cln3Δ, whi5Δcln3Δ* and *whi5Δbck2Δcln3Δ* strains revealed that during the adaptation to the nutrient switch, *cln3Δ* cells did not have as strong a phenotype as *bck2Δ* cells. The G1 duration of the *first daughters of cln3Δ S/G2/M switchers* was not as elongated as that

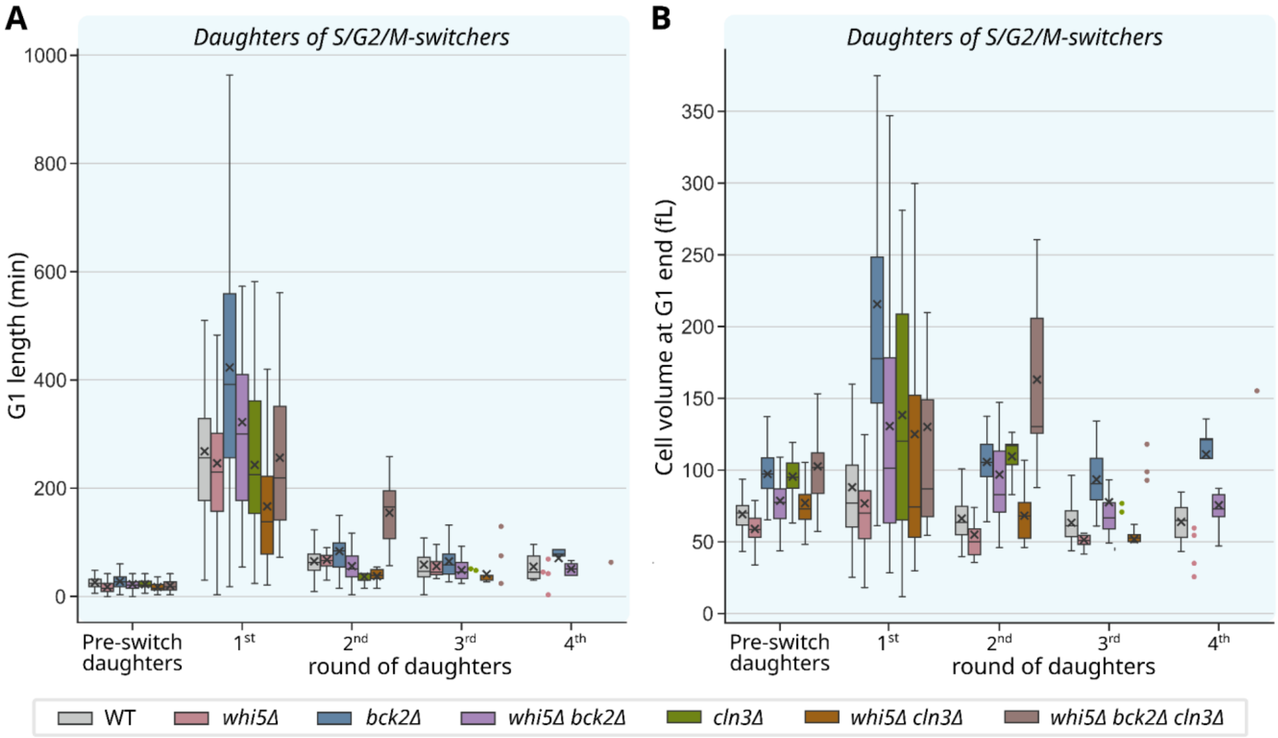

Figure 29: *bck2Δ* cells undergo a longer G1 arrest and stronger enlargement than *cln3Δ* cells after a nutrient switch. (**A**) G1 lengths and (**B**) cell volumes at the end of G1 are plotted for the *rounds of daughters* of *S/G2/M-switchers*. The x symbol shows the mean. Pre-switch daughters are daughter cells born during steady-state growth in SCD before the switch. The dataset for wild type, *whi5Δ*, *bck2Δ*, and *whi5Δbck2Δ* is the

same as in Figure 22. For *cln3Δ*, *whi5Δcln3Δ* and *whi5Δ bck2Δcln3Δ*, cells were pooled from two independent experiments. For the *first round of daughters of S/G2/M-switchers*, $n_{cln3\Delta} = 16$, $n_{whi5\Delta cln3\Delta} = 39$, $n_{whi5\Delta bck2\Delta cln3\Delta} = 11$. The following *rounds of daughters* had fewer cells than the first *round*. For cell categories containing less than 5 cells, individual data points are plotted as a scatter. Strain order in each panel (L-R): WT, *whi5Δ*, *bck2Δ*, *whi5Δbck2Δ*, *cln3Δ*, *whi5Δcln3Δ*, *whi5Δbck2Δcln3Δ*.

of the *bck2Δ first daughters* (Fig. 29A). Additionally, at the end of G1, the *first daughters of cln3Δ S/G2/M switchers* were not as overgrown as their *bck2Δ* counterparts (Fig. 29B). While in steady-state, the cell size of the *whi5Δbck2Δcln3Δ* triple deletion resembled that of the *bck2Δ* and *cln3Δ* single deletions (Fig. 28), in the *first daughters of S/G2/M switchers* born after the nutrient switch, cell size of the triple deletion was closer to *whi5Δbck2Δ* instead of *bck2Δ* (Fig. 29B). This observation was in agreement with a potential nutrient switch-associated depletion of Cln3, which would make Bck2 the more critical G1/S transition activator following the nutrient switch. Thus, while Bck2 and Cln3 seemed functionally redundant in steady-state, the dynamic environments used in this experiment revealed a unique nutrient-switch-specific function for Bck2. To test if a depletion of Cln3 indeed leads to the increased importance of Bck2 after the nutrient-switch, a stabilisation of Cln3 was performed next to test whether it could rescue the long post-switch G1 arrests of *bck2Δ* cells.

3.18. FLAG-tag or locus affects the role of Cln3 after a nutrient switch.

Cln3 is a very unstable protein with a half-life on the order of minutes[119]. It is expected to be depleted immediately following a switch from nutrient-rich to nutrient-poor conditions[89]. To test if stabilised Cln3 can rescue the arrest phenotype of Bck2 mutant cells in a nutrient-switch, the Cln3-11A strain used by Schmoller *et al.*[39] was obtained from Mardo Kõivomägi, NIH, USA. This strain has the endogenous *CLN3* gene deleted and a stabilised FLAG-tagged *CLN3-11A* inserted into the *URA3* locus[39]. The *Cln3-11A* gene has ten of its degradation-inducing phosphosites mutated, which stabilises the protein, and an additional alanine substitution (R108A), which makes the protein less active[39,139,140]. MK40, the control strain for this experiment, also has the endogenous *CLN3* deleted and a FLAG-tagged *CLN3* inserted into the *URA3* locus. For this study, the *whi5Δ* and *bck2Δ* deletions were introduced into the MK40 and the Cln3-11A strains. Since MK40 had a non-stabilised, WT *CLN3* in the *URA3* locus, the expected phenotypes of *whi5Δ* and *bck2Δ* deletions in the MK40 background were expected to resemble those of the *whi5Δ* and *bck2Δ* strains in the MMY116-2C background which was otherwise used for this study. This was indeed the case in steady-state growth, where the *whi5Δ* deletion led to smaller cells and the *bck2Δ* deletion led to bigger cells than MK40, as observed in steady state Coulter-counter measurements (Fig. 30C) and in the pre-switch daughters growing in SCD (Fig. 30A-B). Surprisingly, after the nutrient-switch, the phenotypes of *whi5Δ* and *bck2Δ* were flipped in the MK40 background, with *whi5Δ* cells showing a stronger arrest and overgrowth phenotype in the nutrient switch as compared to *bck2Δ* cells (Fig. 30A-B). This contradictory phenotype in the control MK40-derived strains after the nutrient switch was difficult to interpret and was either stemming from the different background of these strains or from the modifications made to the *CLN3* gene. The FLAG-tag or the changed *CLN3* locus in these strains could be affecting the stability of Cln3 or its interactions with other proteins after the nutrient switch.

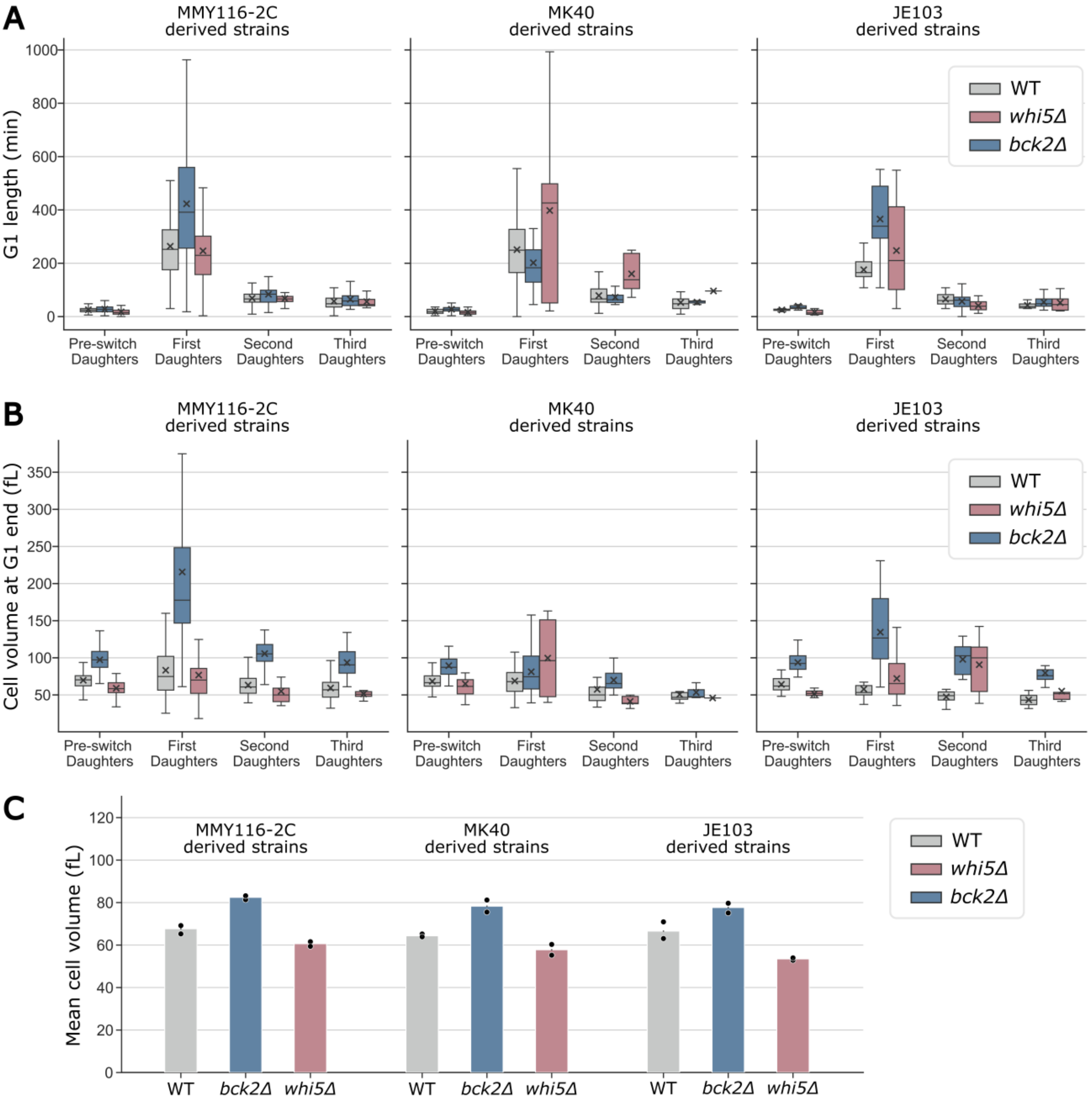

Figure 30: FLAG-tag or locus affects the role of Cln3 after a nutrient switch. (**A**) G1 lengths and (**B**) cell volume at G1 end are plotted for the *rounds of daughters* of *S/G2/M-switchers* originating from three different strains: MMY116-2C (left), MK40 (centre) and JE103 (right). For MMY116-2C- and MK40-derived strains, cells are pooled from a minimum of two independent live-cell microscopy experiments. For JE103-derived strains, data from only one experimental replicate is available. For the *first round of daughters* of *S/G2/M-switchers* of the MMY116-2C background: $n_{\mathrm{WT}} = 123$, $n_{whi5\Delta} = 40$, $n_{bck2\Delta} = 34$. For the *first round of daughters* of *S/G2/M-switchers* of the MK_40 background: $n_{\mathrm{WT}} = 53$, $n_{whi5\Delta} = 5$, $n_{bck2\Delta} = 24$. For the *first round of daughters* of *S/G2/M-switchers* of the JE103 background: $n_{\mathrm{WT}} = 27$, $n_{whi5\Delta} = 14$, $n_{bck2\Delta} = 11$. X denotes the mean. Strain order in each panel (L-R): WT, *bck2Δ*, *whi5Δ*. (**C**) Coulter-counter measurements of cell volume are plotted for cells growing in steady state in SCD. Data is pooled from two experimental replicates. Dot symbol represents the mean cell volume from each individual experimental replicate.

Alternatively, there was the possibility that the strong post-switch arrest phenotype observed in *bck2Δ* cells was specific to the strain used in this study. To test this, the wild type strain from which MK40 was derived, JE103, was obtained. JE103 was the background strain with endogenous *CLN3*. Indeed, upon the introduction of the *whi5Δ* and *bck2Δ* deletions into JE103 and a repetition of the nutrient switch experiment, the phenotypes observed in the strains originating from this study's background strain, MMY116-2C, could be reproduced (Fig. 30A-C). In the JE103 background, the nutrient-switch associated arrest and overgrowth phenotype was indeed stronger in *bck2Δ* cells than *whi5Δ* cells. These results confirmed that the main message of this work was not background-dependent and that the FLAG-tag and locus modifications made to *CLN3* in the MK40 strain somehow affect its role in the nutrient switch. Whether or not the stabilisation of Cln3 can rescue the *bck2Δ* phenotype in a nutrient switch is an exciting question and remains unanswered at the moment. To answer it, the stabilisation of Cln3 must be performed in the endogenous *CLN3* locus without the FLAG-tag. However, these results raise the other important question of how a FLAG-tag or a locus modification might affect Cln3's role. It could either be altering crucial post-switch protein-protein interactions or affecting the post-switch degradation of Cln3. Figuring out the effect of the FLAG-tag or the locus modification on Cln3 could be key to elucidating its role in size adaptation. Given how widely FLAG-tags are used in the field, this would also provide valuable insight into how much they can contribute to observed phenotypes.

3.19. Additional phenotypes of *S/G2/M-switchers* and their *first daughters*: these populations make up the majority of cells that die following a nutrient switch.

To compare cell survival between strains, complete cell cycles and cell cycles during which cells died ('fatal cell cycles') were identified. The fraction of fatal cell cycles for steady-state cells as well as cells from the nutrient switch experiments was plotted (Fig. 31). While the fraction of fatal cell cycles was negligible during steady-state experiments (Fig. 31, first two panels), the nutrient switch led to increased cell death (Fig. 31, third panel). In the nutrient switch, the single deletions, *whi5Δ*, *cln3Δ* and *bck2Δ*, and the triple deletion, *whi5Δbck2Δcln3Δ*, had increased fractions of fatal cell cycles as compared to wild type cells (Fig. 31, third panel). On the contrary, the double deletions (*whi5Δbck2Δ* and *whi5Δcln3Δ*) rescued survival. One potential explanation for this is that the double deletions are closer to wild type in size than the single deletions. Panels four, five and six show the fraction of fatal cycles if specific cell categories are considered: *G1-switchers*, *S/G2/M-switchers* and *first daughters of S/G2/M switchers*. In the last panel, only the fatal cycles during and after the nutrient switch are pooled. This allows the identification of cell categories that have lower survival. *S/G2/M-switchers* and their *first daughters* make up the majority of dying cells (Fig. 31, last panel). Thus, it appears that it is advantageous for cells to face the nutrient switch in G1 as it improves survival. This observation is in agreement with the re-entry of Whi5 into the nucleus upon nutrient switch (Fig. 27), which indicates a cellular preference for a pre-*Start*-like stage in unfavourable nutrient conditions.

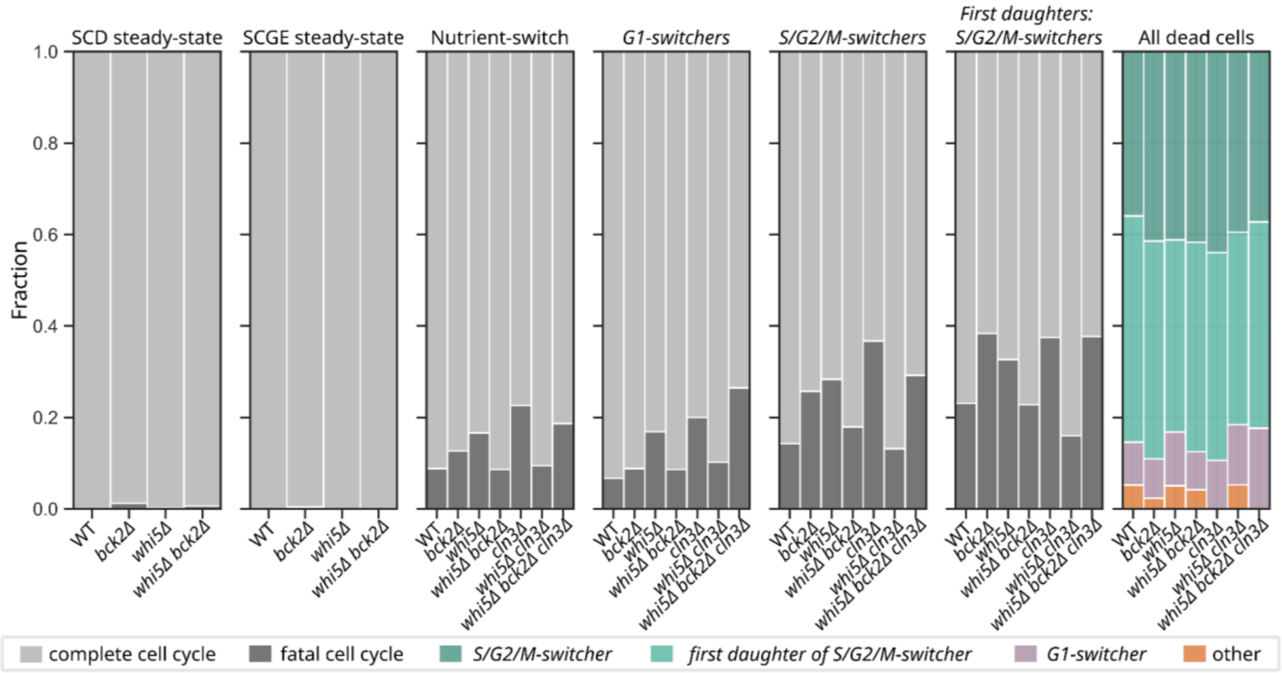

Figure 31: *S/G2/M-switchers* and their *first daughters* make up the majority of dying cells. For cells pooled from a minimum of two independent nutrient switch experiments, all complete cell cycles and cell cycles during which the cells died ('fatal cell cycles') were identified. Of this total, the fraction of fatal cell cycles (dark grey) and the fraction of cell cycles that were completed (light grey) are plotted in a stacked bar plot. The first two panels show the fraction of fatal cycles during steady-state growth in SCD and SCGE. The third panel shows the fraction of fatal cycles during and after the nutrient switch. Panels four, five and six show the fraction of fatal cycles of *G1-switchers*, *S/G2/M-switchers* and *first daughters of S/G2/M switchers* respectively. In the last panel, all fatal cycles during and after the nutrient switch are pooled. The fraction of dead cells belonging to different cell categories is plotted.

3.20. Validating diSpinach tagging: a collaborative project with Kukhtevich *et al.*[1]

In parallel to the main doctoral project, the author of this work used the research group's well-established single molecule fluorescence in-situ hybridisation (smFISH) protocol and downstream analysis software, Spotmax[122,130,131], to validate diSpinach tagging, a novel tool for single-cell RNA visualisation developed by collaborators Kukhtevich *et al*[1]. In this technique, RNAs are tagged with the fluorescent diSpinach aptamer and can be visualised and quantified under the microscope. DiSpinach tagging revealed unique phenotypes for *SUT509* and *ENO2* mRNAs in budding yeast[1]. *SUT509* is a non-coding RNA with previously unknown cell cycle dynamics and *ENO2* RNA encodes the highly expressed enzyme phosphopyruvate hydratase enolase II, involved in glycolysis[141].

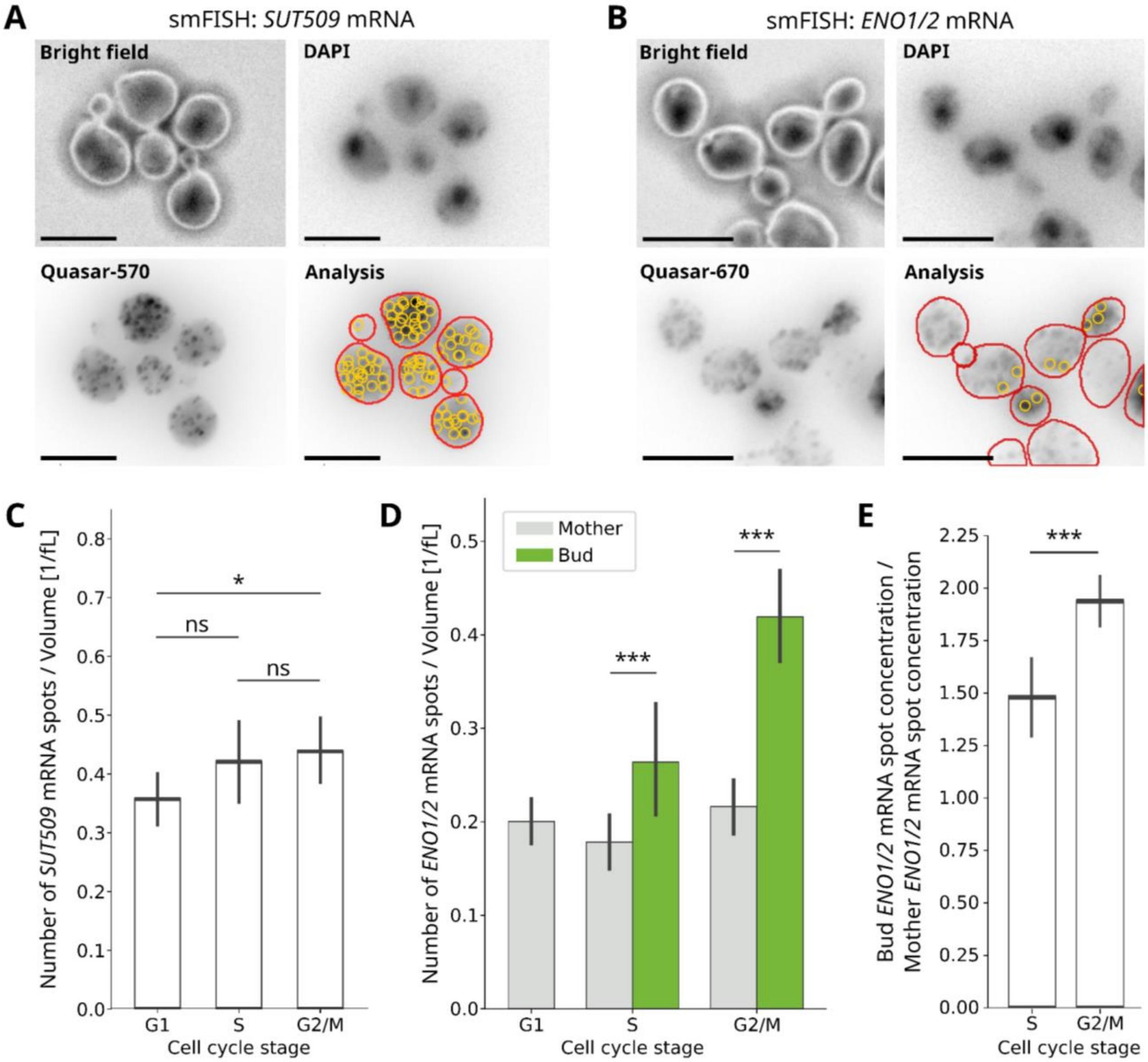

Figure 32: *SUT509* mRNA concentration peaks during G2/M-phase. *ENO1/2* mRNAs are asymmetrically segregated between mother and bud. (**A**) Representative smFISH images: bright field; nuclear DNA stained with DAPI; *SUT509* mRNA stained with Quasar-570 labelled smFISH probes; the spots detected using Spotmax[130] in yellow and cell contours in red. Scale bars represent 5 µm. (**B**) Representative smFISH images: bright field; nuclear DNA stained with DAPI; *ENO1/2* mRNA stained with Quasar-670 labelled smFISH probes; the spots detected using Spotmax[130] in yellow and cell contours in red. Scale bars represent 5 µm. (**C**) Number of *SUT509* mRNA spots detected normalized to cell volume for cells in different cell cycle stages (n_{G1} = 259, n_S = 189, $n_{G2/M}$ = 131). (**D**) Number of *ENO1/2* mRNA spots detected normalized to cell volume for cells in different cell cycle stages (n_{G1} = 574, n_S = 396 mother-bud pairs, $n_{G2/M}$ = 313 mother-bud pairs). (**E**) Ratio of *ENO1/2* mRNA concentrations in the bud and mother in S and G2/M phases. Wilcoxon rank sum tests were used for statistical analyses.

As part of the collaboration with Kukhtevich *et al.*[1], smFISH was used to quantify *SUT509* and *ENO2* mRNAs to test if the results of diSpinach tagging were reproducible with an orthogonal method. DiSpinach tagging showed that the expression of *SUT509-diSpinach* mRNA was cell-cycle dependent and peaked after bud emergence, likely in the G2 phase of the cell cycle. smFISH was used to analyse *SUT509* mRNA concentrations in different cell cycle stages (Fig. 32 A,C) and could reproduce the increased concentration of *SUT509* mRNA in late S and G2/M phases of the cell cycle (Fig. 32C). Since this smFISH was performed in a strain containing the endogenous *SUT509* gene as well as *SUT509-diSpinach* on a plasmid, the smFISH probes are presumed to be binding mRNAs originating from both genes. Additionally, Kukhtevich *et al*[1] showed that the mean *ENO2* mRNA signal in the bud began to exceed that in the mother around 15 minutes before cytokinesis. By the time of cytokinesis, the mean signal in the bud was 1.6 times higher than in the mother. Thus, *ENO2-diSpinach* mRNA was found to be inherited asymmetrically between bud and mother. To confirm this finding, smFISH was performed on endogenous *ENO2* mRNA. However, due to the sequence similarity between *ENO2* and its paralogue *ENO1*, it could not be ruled out that the probes were binding both mRNAs. Additionally, the growth medium of the cells was changed to one with a poorer carbon source (SCGE) to reduce *ENO1/2* expression to levels resolvable by smFISH. Upon analysis of the *ENO1/2* smFISH, strong asymmetric inheritance of *ENO1/2* mRNAs was observed between buds and mothers (Fig. 32B, D-E). While the asymmetric inheritance was already observable in S-phase (Fig. 32D), the strength of the asymmetry was much stronger in G2/M-phase (Fig. 32D-E). Thus, albeit under slightly different conditions that were better suited for smFISH, the phenotype of asymmetric segregation of *ENO1/2-diSpinach* mRNAs observed using the diSpinach tagging technique could be reproduced. These results were published as a validation for the diSpinach tagging technique in the study by *Kukhtevich et al*[1].

4. Discussion

The nutritional quality of the environment is a major regulator of cell size[14,50,72,74]. In nature, wild microorganisms often encounter rapidly changing environments and must accordingly adapt their cell size to the nutritional change. This tuning of the average cell size of the population to the optimum for the new environment is referred to as size adaptation and is an important function of the cellular size control machinery. The other function that the size control machinery fulfils is the maintenance of narrow cell size distributions during steady state conditions, also known as size homeostasis. The current understanding of size control is based almost entirely on steady state studies, i.e. on cells growing in constant environments. Steady-state research has been pivotal for identification of size homeostasis regulators and mechanisms[39,73,76,77,81,82,96], but by design is unable to provide insight into mechanisms of size adaptation. An important goal of this work, therefore, was to use nutrient switch experiments to observe how size adaptation works at the single-cell level and how size homeostasis is reinstated after a nutritional change in the environment. This focus on changing environments helped to reveal a specific function of the poorly understood G1/S activator Bck2. It clarified why the cell evolved two redundant activators, Bck2 and Cln3, for the G1/S transition. While Bck2 and Cln3 appear redundant in steady state conditions, the changing nutrient conditions used in this work revealed that Bck2 becomes the more important G1/S activator in the lag phase following a nutrient switch, likely due to the nutrient-dependent depletion of Cln3. To observe size homeostasis and size adaptation at the single-cell level, this work generated a manually corrected live-cell microscopy dataset of over 13700 complete cell cycles, which could prove valuable for answering other open questions in the size control field, as well as for improving the accuracy of automated image analysis. Moreover, this work developed the conceptual framework to identify and analyse different cell categories with unique phenotypes in a complex nutrient switch dataset.

4.1. *whi5Δbck2Δ* has slower size adaptation as compared to WT

Initially, this work was aimed at better understanding the budding yeast G1/S size homeostasis network and the interactions between its various constituents in steady state conditions. The first set of results from this study helped clarify that Whi5 is not downstream of Bck2 and that the two proteins affect cell size through independent pathways (Fig.13-14). It also confirmed that Ccr4 does not promote degradation of Whi5 mRNA (Fig. 11-12). Moreover, this work showed that Whi7 does not compensate as an upregulated G1/S inhibitor in the absence of Whi5 (Fig. 11). These pieces of information helped create a clearer picture of the G1/S size homeostasis network (Fig. 33). Interestingly, Whi7 was found to be highly overexpressed in the absence of Ccr4, which could link Whi7's function as a cell cycle brake in conditions of cell wall stress to the extremely large cell sizes of the *ccr4Δ* mutant[101–103]. While further investigation of this upregulation of Whi7 in *ccr4Δ* and *whi5Δccr4Δ* cells was beyond the scope of this study, it makes an exciting topic for future work on size homeostasis in conditions of stress.

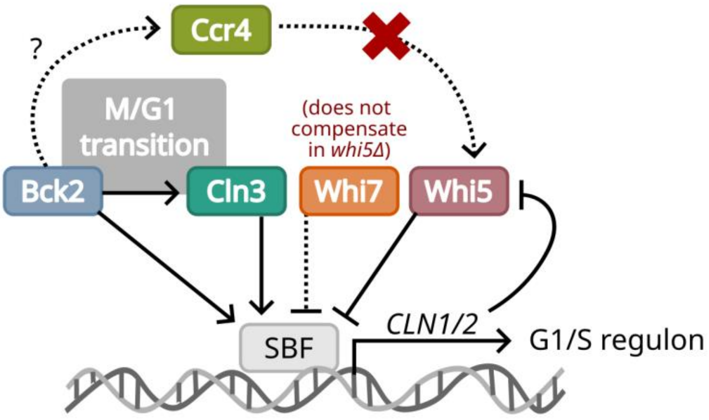

Figure 33: The updated budding yeast G1/S size homeostasis network. Results from this study show that Whi5 and Bck2 affect G1/S transition through independent pathways and Bck2 does not promote degradation of *WHI5* mRNA through Ccr4. This work also shows that Whi7 expression is not upregulated in the *whi5Δ* mutant, indicating that Whi7 does not compensate for the absence of Whi5 in steady-state conditions.

Before this work, bulk methods in steady state research had revealed a robustness of cell size homeostasis efficiency to single deletions of size regulator proteins[73,77]. This robustness indicated the existence of redundant 'backup' pathways that maintained homeostasis when the major size regulators were deleted. This study's steady state live-cell imaging of *whi5Δ, bck2Δ* and *whi5Δbck2Δ* cells confirmed this result at the single-cell level. It showed that while a reduction in size homeostasis efficiency was observed in the *whi5Δ* and *bck2Δ* strains, the size homeostasis efficiency as well as the mean cell size of *whi5Δbck2Δ* were surprisingly similar to those of WT, especially in glucose medium (Fig. 15). These observations steered this study into the direction of investigating whether the simultaneous deletion of two size regulators, *whi5Δ* and *bck2Δ,* had any cost to the cell and, if so, what the phenotype of that cost was.

Since both Bck2 and Whi5 had previously been implicated in linking nutrient availability to cell volume or cell cycle progression[72,80], there was the possibility that they had unique functions in size adaptation and *whi5Δbck2Δ* cells would show differences in cell size homeostasis efficiency as compared to WT under changing nutrient conditions. To test this theory, this work included an initial bulk nutrient switch experiment which revealed that for both WT and *whi5Δbck2Δ* cells, after a switch from rich to poor carbon media, the mean cell volume of the population and CV of cell volume showed a strong initial increase before starting to reduce to what is expected from steady state growth in poor carbon (Fig. 18). For the mean cell volume, this initial increase in cell size was unexpected because a shift to poor nutrients ultimately leads to a reduction in cell size. For the CV of cell volume, a period of high CV could theoretically be explained by a temporary disruption of size homeostasis as the target size of the population is tuned to the new environment. Importantly, *whi5Δbck2Δ* cells showed a stronger increase in the CV of cell volume than WT cells, indicating a slower size adaptation in the double mutant. Thus, through this time course of observations of the CV of cell volume during a nutrient switch, this study provided new insight into size adaptation and found a size homeostasis efficiency phenotype for *whi5Δbck2Δ* cells. To explain the causes for these post-switch trends in cell volume and its CV and to ascertain the reason for the higher CV in *whi5Δbck2Δ* cells, it was necessary to obtain single-cell information from the nutrient-switch through microscopy. In fact, the differences observed between WT and *whi5Δbck2Δ* cells in this bulk experiment led to the discovery of much stronger size phenotypes in specific cell categories through microscopy.

4.2. Bck2 plays a crucial role in size adaptation to changing nutrients

It was clear from studies such as Irvali *et al*.[108] and Leitao *et al*.[74] that a cell's cell cycle stage at the time of a nutrient change affected how the cell and its offspring adapt to the nutrient change. The analysis of the live-cell imaging experiment that is coupled to a nutrient switch, therefore, must account for each cell's temporal distance from the switch and its or its ancestor's cell cycle stage at the time of the switch. Extracting this information from videos of cell growth required multigenerational tracking and cell categorisation. Given that traditional image analysis had already been the bottleneck in live cell imaging studies, this additional analytical task explained why very few studies coupled nutrient switches with live cell imaging. Therein lay a major novelty of this work, as it took advantage of recent developments in deep learning-based image segmentation, tracking and annotation methods as well as of the user-friendly software, Cell-ACDC, to accelerate the execution of these otherwise prohibitively time- and labour-intensive tasks. This approach enabled the generation of an expansive single-cell microscopy dataset to address the questions of how size homeostasis was affected by and reinstated after a nutrient switch at the single cell level.

Live cell imaging through the nutrient switch revealed that the post-switch increases in cell volume and CV of cell volume observed in the bulk nutrient switch experiment (Fig. 18) could be explained by cell cycle arrests resulting from the nutrient switch (Fig. 21-22). These cell cycle arrests of cells that faced the switch led to cellular enlargement which explained the increase in mean cell volume and CV of cell volume observed in the bulk nutrient switch experiment (Fig. 18). Of the four strains tested, the strains with the longest arrest times and strikingly higher cellular overgrowth during these arrests were the strains that had a *BCK2* deletion, i.e., *bck2Δ* and *whi5Δbck2Δ*. *whi5Δbck2Δ* cells, which started off very similarly sized to WT cells while growing in glucose, were significantly bigger than WT cells at the end of the nutrient-switch-induced arrest (Fig. 21). Moreover, after the nutrient switch, the *whi5Δbck2Δ* cells resembled *bck2Δ* cells in their cell volume and arrest duration phenotypes, indicating that Bck2 plays an important role in size adaptation.

The most obvious mechanistic explanation for such a role for Bck2 in size adaptation stems from previous studies on Cln3, which is also the better understood protein between the two. Sommer *et* *al.*[89] showed that Cln3 is depleted soon after a switch from glucose to glycerol-ethanol medium. Moreover, it is known that a double deletion of *CLN3* and *BCK2* leads to a permanent G1 arrest and is thereby lethal[95]. Given this synthetic lethality of Cln3 and Bck2, it is possible that the post-switch Cln3 depletion in the *bck2Δ* mutant temporarily mimics a *cln3Δbck2Δ* state until Cln3 synthesis resumes (Fig. 34), making Bck2 the only available G1/S activator for the time period directly following the switch. This could explain the longer G1 arrests observed in *bck2Δ* mutants after the nutrient switch, as they temporarily lack both G1/S activators. In agreement with this hypothesis, Fig. 29 of this thesis shows that *cln3Δ* cells have a much weaker arrest and overgrowth phenotype than *bck2Δ* cells after a nutrient-switch. A direct test of this model (Fig. 34) would be to check if a stabilisation of Cln3 during the switch could rescue the long arrests observed in *bck2Δ* mutants. Unfortunately, as described in section 3.18, the strains with stabilised Cln3 obtained from collaborators contained a FLAG-tagged *CLN3* in a non-endogenous locus, which affected the phenotypes even in the control strain. Thus, these experiments need to be repeated with the stabilised version of *CLN3* introduced in the endogenous locus without the FLAG tag. In fact, the stabilised *CLN3* is also planned to be under the control of the inducible *MET25* promoter to enable external regulation of its expression in addition to the stabilisation. Having *CLN3* under the control of the *MET25* promoter also ensures removal of potential transcriptional regulation of *CLN3* after the nutrient-switch. These experiments could not be included in this thesis due to time constraints but will be included in the publication linked to this work[142] as they are critical for testing this hypothesis.

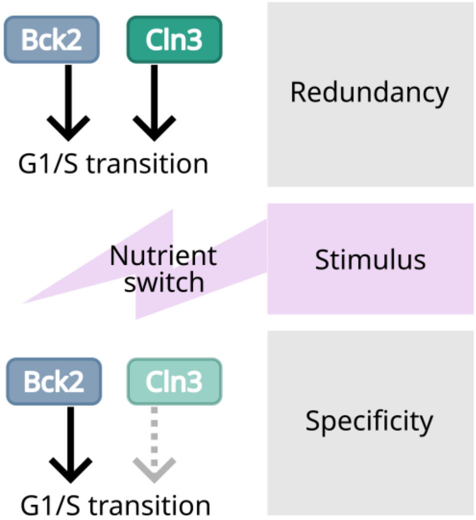

Figure 34: Studying redundant proteins in non-steady-state conditions can reveal unique functions for them. This study hypothesizes that while Bck2 and Cln3's roles in G1/S activation appear phenotypically redundant in steady state conditions, a stimulus such as a nutrient switch can cause a temporary depletion of Cln3, making Bck2 the only available G1/S activator. Such experimental conditions can explain the need for the cell to evolve two redundant activators for the same cell cycle transition and reveal condition-specific functions for them.

While this mechanistic explanation for the *bck2Δ* phenotype after the switch is the most obvious, it is not necessarily the correct or the only explanation, until proven to be so. At the moment, therefore, it is important to keep in mind other possible mechanisms, such as Bck2's parallel role in the cell wall stress response, which could also contribute to its increased importance after the nutrient switch. Bck2 is a part of the cell wall integrity pathway that responds to cell wall damage or heat-shock. Cell wall stress activates the protein kinase C, Pkc1, which in turn activates a cascade of mitogen-activated protein kinases (MAPKs) which eventually lead to expression of cell wall maintenance genes[143]. While the exact molecular mechanism is still unknown, Bck2 is associated with the activation of the last MAP kinase in the cascade, Mpk1[144]. A deletion of Bck2 has been shown to increase sensitivity to cell-wall-affecting drugs such as Congo red and calcofluor white, whereas overexpression of Bck2 can increase drug-resistance as well as rescue the cell-growth defect of *pkc1Δ* and *mpk1Δ* mutants[94,145]. Together with other studies that describe a role for Bck2 in resistance to multiple antifungal drugs[146], this shows that Bck2 is important for the cell's response to cell-wall stress. A recent nutrient-switch study from Shabestary *et al.*[126] analysed budding yeast adaptation to a nitrogen-downshift and found a bimodality in the cell volume distribution of the resulting post-switch population. This bimodality led to an increased CV of cell volume after the nutrient-switch, similar to the increased CV of cell volume observed in the bulk experiments from this study. Shabestary *et al.*[126] also found that the bimodality in cell size is accompanied by two distinct metabolic states: one that favours viability or survival and one that favours growth. The more viable subpopulation was smaller in cell size, showed more active MAPK signalling and transcriptionally resembled low-glucose states. Given Bck2's proposed role in MAP kinase (Mpk1) activation, the large cell size and lower survival of post-switch *bck2Δ* cells, as observed in this work, could also originate from disrupted MAPK signalling and the consequently inadequate stress response. Thus, studying Mpk1 activation and how it is affected by a *BCK2* deletion during the nutrient switch would be important for clarifying Bck2's contribution to size adaptation.

4.3. Budded cells carry a memory of the nutrient switch into their next cell cycle

Cells can either face a nutrient switch in a budded (S/G2/M) or an unbudded (G1) state (Fig. 21A). This work shows that regardless of what cell cycle stage they face the nutrient switch in, they arrest immediately after the switch (Fig. 21B). For the *G1-switchers*, the arrest is limited to the G1 phase that they face the nutrient switch in and the next cell-cycle is largely unaffected (Fig. 21B, Fig. 35). This is not the case for *S/G2/M-switchers*, which surprisingly also arrest in the G1 of the following cell cycle (Fig. 21B, Fig. 35). This arrest in the G1 of a cell cycle that starts after the nutrient switch indicates a mechanism that preserves the memory of the switch (Fig. 35). Additionally, this 'memory' is also observed in the *first daughters of S/G2/M-switchers*, which were buds at the time of the nutrient switch. These cells arrest during the G1 phases of their first cell cycles, which start after the nutrient switch (Fig. 22B, Fig. 35). Moreover, the *S/G2/M-switchers* and the *first daughters of S/G2/M-switchers* are the two cell categories with the lowest survival (Fig. 31) and the biggest cell sizes at the end of the G1 arrests (*bck2Δ* and *whi5Δbck2Δ* cells, Fig. 21C, Fig. 22C). These strong phenotypes raise the question of what mechanism is behind the memory of the nutrient switch in these cell categories.

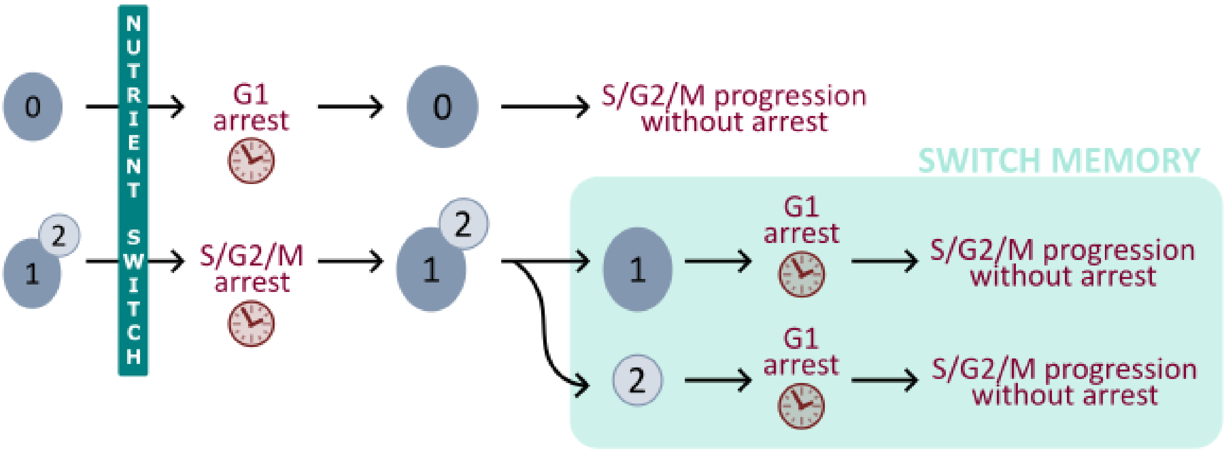

Figure 35: Schematic explanation of the memory of the nutrient switch observed in *S/G2/M-switchers* and the *first daughters of S/G2/M-switchers*. When *G1-switchers* (cell 0) and *S/G2/M-switchers* (cell 1) experience the nutrient-switch, they immediately arrest in the ongoing cell cycle stage. For *G1-switchers*, cell cycle progression continues largely normally after this initial G1 arrest. *S/G2/M-switchers*, on the contrary, also arrest in the G1 phase of their next cell cycle, which starts after the nutrient switch. The *first daughters of S/G2/M-switchers* (cell 2), which were buds at the time of the nutrient switch, also experience a similar G1 arrest in their first cell cycles that start after the nutrient switch. These G1 arrests of *S/G2/M-switchers* and their *first daughters* that occur in cell cycles that start after the nutrient indicate a memory of the nutrient switch (shaded area).

Work from Min *et al*.[147] indicates that in human epithelial cells, protein translation rates during the cell cycle of a mother cell can regulate the availability of a protein in the cell cycle of its daughter cell. In this manner, the abundance of one or more proteins in the current cell cycle can reveal information about the translation rate or the duration of the previous cell cycle. A similar mechanism was proposed by Qu *et al*.[72] in budding yeast. They found that the amount of Whi5 in the G1 phase of the current cell cycle was correlated with the doubling time of the past cell cycle. As an inhibitor of the G1/S transition, higher Whi5 amounts during G1 can increase G1 duration, allowing Whi5 to link the nutrient availability during the previous cell cycle to cell cycle progression in the current cell cycle. This ‘memory’ mechanism could also be applied to the cell categories in this work that appeared to have a memory of the nutrient switch in their next cell cycles (Fig. 35).

Immediately after the nutrient switch, *S/G2/M-switchers* first arrest in the S/G2/M phase in their *switch-cell-cycles* (Fig. 21B, Fig. 35), which is also the phase during which Whi5 is synthesized[39,72]. This S/G2/M arrest increases the doubling time of the *switch-cell-cycle* of *S/G2/M-switchers*, which, according to Qu *et al*.[72], should increase the amount of Whi5 that the *S/G2/M-switchers* and their daughters (*first daughters of S/G2/M-switchers*) inherit upon division. Inheriting a higher amount of Whi5 is a potential explanation for the longer G1 arrests observed in these two cell categories. This hypothesis can also explain why no ‘memory’ is observed in the *G1-switchers* or their *first daughters* - because they do not undergo an S/G2/M arrest (Fig. 21B, Fig. 22B). However, if Whi5 was the only factor contributing to this ‘memory’, the G1 arrest of the *S/G2/M-switchers* and their *first daughters* would be expected to be rescued in the *whi5Δ* and the *whi5Δbck2Δ* strains. While the G1 arrest duration of *whi5Δ* cells is only slightly shorter than that of WT cells, the G1 arrest duration of *whi5Δbck2Δ* cells is partially rescued compared to that of *bck2Δ* cells, indicating the involvement of Whi5 as well as other factors in this 'memory' phenotype (Fig. 21B, Fig. 22B).

Another observation that supports the involvement of multiple factors in the 'memory' phenotype is that immediately after the nutrient switch, the S/G2/M arrest durations are similar between *S/G2/M-switchers* of various strains (Fig. 21B). However, these similar S/G2/M arrest durations lead to very different G1 arrest durations in the next cell cycles of these cells, especially in strains lacking Bck2. Thus, the deletion of Bck2 must also contribute to the memory of the nutrient switch observed in the *S/G2/M-switchers* and their *first daughters*. It is known that at the M/G1 transition, Bck2 promotes expression of Cln3[80] (Fig. 33). Accordingly, a deletion of *BCK2* leads to reduced and delayed Cln3 expression[80]. Cln3 transcription peaks at the M/G1 transition[80] and Cln3 is already known to be depleted immediately after a switch from rich to poor carbon[89]. Thus, an additional deletion of *BCK2* could delay and reduce Cln3 transcription at the next M/G1 transition in cells that face the nutrient switch in S/G2/M, leading to them starting their next cell cycles with lower than normal amounts of Cln3 and thereby experiencing longer G1 arrests. Additionally, Bck2 is also known to promote the expression of Swi4 at the M/G1 transition, which is a subunit of the SBF complex[80] (Fig. 33) that promotes expression of the G1/S regulon. Coupled with an expected reduction in Cln3 amounts in *bck2Δ* cells, an added reduction in Swi4 would further elongate the G1 arrest. However, these hypotheses regarding the mechanisms behind the memory phenotype are speculative and need to be experimentally verified. For example, quantifying Whi5, Cln3 and Swi4 amounts in single cells of different categories during the nutrient switch could provide insight into whether the cells that arrest in S/G2/M really start the next cell cycle with higher Whi5 or lower Cln3 and Swi4 amounts.

4.4. ***bck2Δ*** buds that face the nutrient switch after anaphase have the longest arrests and most overgrowth in their first G1

In the previous section, a potential link between Bck2's role in promoting Cln3 expression at the M/G1 transition and the memory of the nutrient switch in the first non-switch-facing cell cycles of *S/G2/M-switchers* and their *first daughters* is described. In agreement with this theory, this work also shows that when the first daughters of *S/G2/M-switchers* are categorised based on the specific S/G2/M stage of the mother at the time of the switch, the categories of *bck2Δ* and *whi5Δbck2Δ* daughters whose mothers were post-anaphasic at the time of the nutrient switch have the most extreme G1 arrest phenotypes (Fig. 26). The majority of these *bck2Δ* and *whi5Δbck2Δ* daughters remain arrested in G1 until the end of the experiment (Fig. 26B). None of the *bck2Δ* daughters whose mothers were post-anaphasic at the time of the nutrient switch exit G1 during the course of the experiment. Some of the *whi5Δbck2Δ* daughters whose mothers were post-anaphasic at the time of the nutrient switch do complete G1 during the experiment and this category has the longest G1 arrests (Fig. 26A). These results show that for the cell, it is most disadvantageous to face the nutrient switch after anaphase has ended while simultaneously lacking Bck2.

Why does facing a nutrient switch during telophase or cytokinesis lead to longer G1 arrests in the next cell cycle than facing a switch in metaphase or anaphase? Work from Leitao *et al.*[74] has shown that cells facing a nutrient downshift during metaphase can undergo a long metaphase arrest, whereas cells facing the nutrient downshift in anaphase do not show any delays in anaphase completion. They propose the existence of a nutrient-regulated bud growth sensor that increases metaphase duration if a nutrient downshift occurs before the bud has grown sufficiently. Such a sensor would not arrest the cell in anaphase upon a nutrient downshift because the bud usually achieves its target size before anaphase starts[74]. In fact, Talavera *et al*.[75] suggest that this nutrient-modulated bud growth sensing is brought about by components of the mitotic exit network, which are phosphorylated in a growth dependent manner and promote exit from mitosis in anaphase/telophase once sufficient growth has occurred. Given these findings, it is possible that pre-anaphasic and early anaphasic *switchers* in this work's dataset also underwent a long arrest after the nutrient switch to allow sufficient bud growth before mitotic exit. This would give these cells time to undergo metabolic reprogramming and resume Cln3 synthesis by the time they reach the M/G1 transition. On the other hand, cells that faced the nutrient switch in late anaphase, telophase or cytokinesis had likely already started mitotic exit and Cln3 synthesis. In these cells, the already synthesised Cln3 would be expected to be quickly degraded after the nutrient switch, which would result in cells entering G1 with much lower Cln3 amounts. On top of that, a deletion of *BCK2* would lead to one less activator at the G1/S transition, as well as further reduction and delay in Cln3 synthesis at the M/G1 transition, which could explain the strong arrests observed in *bck2Δ* and *whi5Δbck2Δ* daughters of post-anaphasic *switchers*.

4.5. Outlook and future work

The most important finding of this work is that studying size adaptation to changing nutrient conditions can reveal unique roles for size regulators that appear redundant in size homeostasis, which is typically studied in steady state conditions. This work describes one such case, where a double mutant lacking two size homeostasis regulators, *whi5Δbck2Δ*, does not have a strong size or size control phenotype under steady state conditions. However, studying the same strain under changing nutrient conditions reveals that it undergoes longer arrests and more cellular overgrowth than WT cells in the lag phase after a nutrient switch. Thus, changing nutrient conditions reveal a higher cost of the double mutation for the cell than what is observable in steady state conditions.

Moreover, the nutrient switch shows that this arrest and overgrowth phenotype of *whi5Δbck2Δ* cells is similar to that of *bck2Δ* cells, indicating a key role for Bck2 in size adaptation following a nutrient switch.

The main hypothesis of this work is that Bck2 serves as a 'backup' G1/S transition activator when Cln3 is depleted in the lag phases following nutrient switches. The most critical future experiment for this work, therefore, is the testing of this hypothesis. A clear test of this hypothesis would be whether or not stabilising Cln3 during the nutrient switch rescues the long arrests observed in the *bck2Δ* mutant. These experiments are already underway as part of the revision of the publication linked to this work[142].

Another experiment that would strongly support the hypothesis would be confirming the depletion of Cln3 at the single cell level, as so far it has only been done in bulk by Western blotting[89]. Cln3's instability makes it a difficult protein to visualise using regular fluorescent tagging[39] as the maturation time of the fluorescence protein is often longer than the half-life of Cln3, which is on the order of minutes[119]. Tagging a stabilised version of Cln3 is not an option if its dynamics during the nutrient switch need to be examined. Newer techniques such as split-GFP tagging[73] or superfolder-GFP tagging[86] that can bypass the long maturation times of fluorescent proteins can be used to visualise Cln3 using live cell microscopy during the nutrient-switch. As opposed to single-time-point techniques such as immunofluorescence, these techniques also preserve the history of the cell, which is necessary for the cell categorisation used in the nutrient switch analysis in this work. Alongside Cln3, quantifying Whi5 and Swi4 dynamics during the nutrient switch and their concentrations in different cell categories would be useful to ascertain the mechanism behind the memory of the nutrient switch observed in *S/G2/M-switchers* and their *first daughters*.

It would also be interesting to test if this increased importance of Bck2 is unique to a switch from glucose to glycerol-ethanol media or is also observed in other switches involving different growth media. While a switch from glucose to glycerol-ethanol as a carbon source requires metabolic reprogramming from fermentation to respiration, a switch from glucose to a fermentable sugar such as sucrose or fructose, for example, would maintain the cell's fermentative state. Thus, the arrest durations after a switch would be specific to the media combinations used. While Cln3 has been shown to be depleted in a switch from glucose to glycerol-ethanol media[89], how other combinations of nutrient switches would affect its abundance is not yet known. Switch experiments involving different media combinations would provide insight into which media switches lead to Cln3 depletion and whether Bck2's role as a 'back-up' G1/S activator is consistent in all media switches that deplete Cln3.

Taken together, the findings in this work describe a unique role in size adaptation for the relatively understudied G1/S activator Bck2. They emphasize the need for mimicking real-world conditions such as dynamic environments in the laboratory to uncover new functions for proteins and possibly solve redundancies between them. Furthermore, this work highlights the power of single cell tracking and categorisation in finding heterogeneous phenotypes within a cell population. To that end, it contributes an expansive single-cell dataset containing over 13700 manually checked complete cell cycles to the size control field. The generation of this dataset was enabled by the rapid development of machine-learning based image analysis approaches, which helped partially dismantle the bottleneck of image analysis. Parts of the image analysis pipeline, however, still lack automation or need supervision. In the future, this manually annotated dataset can be used as training or ground-truth data to further improve the accuracy of automated image analysis pipelines and help automate tasks that still need manual supervision. Automated image analysis pipelines that are accurate and quick will be key to analysing even bigger datasets, such as those originating from the microscopy of multiple types of nutrient switches. Biological inferences about both size homeostasis and size adaptation can then be made from this wealth of data by using the conceptual framework provided by this study for analysing heterogenous phenotypes in cell populations faced with a nutrient switch.

5. References

1. Kukhtevich IV, Rivero-Romano M, Rakesh N, Bheda P, Chadha Y, Rosales-Becerra P, Hamperl S, Bureik D, Dornauer S, Dargemont C, Kirmizis A, Schmoller KM, Schneider R. Quantitative RNA imaging in single live cells reveals age-dependent asymmetric inheritance. *Cell Rep*. 2022;41(7):111656. doi:10.1016/j.celrep.2022.111656

2. Smith DH. Stretch growth of integrated axon tracts: Extremes and exploitations. *Prog Neurobiol*. 2009;89(3):231-239. doi:10.1016/j.pneurobio.2009.07.006

3. Palenik B, Grimwood J, Aerts A, Rouzé P, Salamov A, Putnam N, Dupont C, Jorgensen R, Derelle E, Rombauts S, Zhou K, Otillar R, Merchant SS, Podell S, Gaasterland T, Napoli C, Gendler K, Manuell A, Tai V, Vallon O, Piganeau G, Jancek S, Heijde M, Jabbari K, Bowler C, Lohr M, Robbens S, Werner G, Dubchak I, Pazour GJ, Ren Q, Paulsen I, Delwiche C, Schmutz J, Rokhsar D, Van De Peer Y, Moreau H, Grigoriev IV. The tiny eukaryote *Ostreococcus* provides genomic insights into the paradox of plankton speciation. *Proc Natl Acad Sci*. 2007;104(18):7705-7710. doi:10.1073/pnas.0611046104

4. Hatton IA, Galbraith ED, Merleau NSC, Miettinen TP, Smith BM, Shander JA. The human cell count and size distribution. *Proc Natl Acad Sci*. 2023;120(39):e2303077120. doi:10.1073/pnas.2303077120

5. Balachandra S, Sarkar S, Amodeo AA. The Nuclear-to-Cytoplasmic Ratio: Coupling DNA Content to Cell Size, Cell Cycle, and Biosynthetic Capacity. *Annu Rev Genet*. 2022;56(1):165-185. doi:10.1146/annurev-genet-080320-030537

6. Fung HF, Bergmann DC. Function follows form: How cell size is harnessed for developmental decisions. *Eur J Cell Biol*. 2023;102(2):151312. doi:10.1016/j.ejcb.2023.151312

7. Cadart C, Heald R. Scaling of biosynthesis and metabolism with cell size. Schroer T, ed. *Mol Biol Cell*. 2022;33(9):pe5. doi:10.1091/mbc.E21-12-0627

8. Miettinen TP, Björklund M. Mitochondrial Function and Cell Size: An Allometric Relationship. *Trends Cell Biol*. 2017;27(6):393-402. doi:10.1016/j.tcb.2017.02.006

9. Kempe H, Schwabe A, Crémazy F, Verschure PJ, Bruggeman FJ. The volumes and transcript counts of single cells reveal concentration homeostasis and capture biological noise. Matera AG, ed. *Mol Biol Cell*. 2015;26(4):797-804. doi:10.1091/mbc.E14-08-1296

10. Padovan-Merhar O, Nair GP, Biaesch AG, Mayer A, Scarfone S, Foley SW, Wu AR, Churchman LS, Singh A, Raj A. Single Mammalian Cells Compensate for Differences in Cellular Volume and DNA Copy Number through Independent Global Transcriptional Mechanisms. *Mol Cell*. 2015;58(2):339-352. doi:10.1016/j.molcel.2015.03.005

11. Neurohr GE, Terry RL, Lengefeld J, Bonney M, Brittingham GP, Moretto F, Miettinen TP, Vaites LP, Soares LM, Paulo JA, Harper JW, Buratowski S, Manalis S, van Werven FJ, Holt LJ, Amon A. Excessive Cell Growth Causes Cytoplasm Dilution And Contributes to Senescence. *Cell*. 2019;176(5):1083-1097.e18. doi:10.1016/j.cell.2019.01.018

12. Lanz MC, Zhang S, Swaffer MP, Ziv I, Götz LH, Kim J, McCarthy F, Jarosz DF, Elias JE, Skotheim JM. Genome dilution by cell growth drives starvation-like proteome remodeling in mammalian and yeast cells. *Nat Struct Mol Biol*. 2024;31(12):1859-1871. doi:10.1038/s41594-024-01353-z

13. Zhurinsky J, Leonhard K, Watt S, Marguerat S, Bähler J, Nurse P. A Coordinated Global Control over Cellular Transcription. *Curr Biol*. 2010;20(22):2010-2015. doi:10.1016/j.cub.2010.10.002

14. Chadha Y, Khurana A, Schmoller KM. Eukaryotic cell size regulation and its implications for cellular function and dysfunction. *Physiol Rev*. 2024;104(4):1679-1717. doi:10.1152/physrev.00046.2023

15. Ginzberg MB, Kafri R, Kirschner M. On being the right (cell) size. *Science*. 2015;348(6236). doi:10.1126/science.1245075

16. Stenkula KG, Erlanson-Albertsson C. Adipose cell size: importance in health and disease. *Am J Physiol-Regul Integr Comp Physiol*. 2018;315(2):R284-R295. doi:10.1152/ajpregu.00257.2017

17. Dukkipati SS, Garrett TL, Elbasiouny SM. The vulnerability of spinal motoneurons and soma size plasticity in a mouse model of amyotrophic lateral sclerosis. *J Physiol*. 2018;596(9):1723-1745. doi:10.1113/JP275498

18. Martin TG, Juarros MA, Leinwand LA. Regression of cardiac hypertrophy in health and disease: mechanisms and therapeutic potential. *Nat Rev Cardiol*. 2023;20(5):347-363. doi:10.1038/s41569-022-00806-6

19. Levy D, Garrison RJ, Savage DD, Kannel WB, Castelli WP. Prognostic Implications of Echocardiographically Determined Left Ventricular Mass in the Framingham Heart Study. *N Engl J Med*. 1990;322(22):1561-1566. doi:10.1056/NEJM199005313222203

20. Khurana A, Chadha Y, Schmoller KM. Too big not to fail: Different paths lead to senescence of enlarged cells. *Mol Cell*. 2023;83(22):3946-3947. doi:10.1016/j.molcel.2023.10.024

21. Davies DM, Van Den Handel K, Bharadwaj S, Lengefeld J. Cellular enlargement - A new hallmark of aging? *Front Cell Dev Biol*. 2022;10:1036602. doi:10.3389/fcell.2022.1036602

22. Manohar S, Neurohr GE. Too big not to fail: emerging evidence for size-induced senescence. *FEBS J*. 2024;291(11):2291-2305. doi:10.1111/febs.16983

23. Xie S, Swaffer M, Skotheim JM. Eukaryotic Cell Size Control and Its Relation to Biosynthesis and Senescence. *Annu Rev Cell Dev Biol*. 2022;38(1):291-319. doi:10.1146/annurev-cellbio-120219-040142

24. Liu S, Tan C, Tyers M, Zetterberg A, Kafri R. What programs the size of animal cells? *Front Cell Dev Biol*. 2022;10. doi:10.3389/fcell.2022.949382

25. Cadart C, Monnier S, Grilli J, Sáez PJ, Srivastava N, Attia R, Terriac E, Baum B, Cosentino-Lagomarsino M, Piel M. Size control in mammalian cells involves modulation of both growth rate and cell cycle duration. *Nat Commun*. 2018;9(1). doi:10.1038/s41467-018-05393-0

26. Ginzberg MB, Chang N, D’Souza H, Patel N, Kafri R, Kirschner MW. Cell size sensing in animal cells coordinates anabolic growth rates and cell cycle progression to maintain cell size uniformity. *eLife*. 2018;7:e26957. doi:10.7554/eLife.26957

27. Liu S, Tan C, Melo-Gavin C, Ginzberg MB, Blutrich R, Patel N, Rape M, Mark KG, Kafri R. Oversized cells activate global proteasome-mediated protein degradation to maintain cell size homeostasis. *eLife*. 2025;14:e75393. doi:10.7554/eLife.75393

28. Fantes PA. Control of cell size and cycle time in *Schizosaccharomyces pombe*. *J Cell Sci*. 1977;24(1):51-67. doi:10.1242/jcs.24.1.51

29. Voorn WJ, Koppes LJH. Skew or third moment of bacterial generation times. *Arch Microbiol*. 1997;169(1):43-51. doi:10.1007/s002030050539

30. Pan KZ, Saunders TE, Flor-Parra I, Howard M, Chang F. Cortical regulation of cell size by a sizer cdr2p. *eLife*. 2014;3:e02040. doi:10.7554/eLife.02040

31. Soifer I, Robert L, Amir A. Single-cell analysis of growth in budding yeast and bacteria reveals a common size regulation strategy. *Curr Biol*. 2016;26(3):356-361. doi:10.1016/j.cub.2015.11.067

32. Rhind N. Cell-size control. *Curr Biol*. 2021;31(21):R1414-R1420. doi:10.1016/j.cub.2021.09.017

33. Killander D, Zetterberg A. A quantitative cytochemical investigation of the relationship between cell mass and initiation of DNA synthesis in mouse fibroblasts in vitro. *Exp Cell Res*. 1965;40(1):12-20. doi:10.1016/0014-4827(65)90285-5

34. Chandler-Brown D, Schmoller KM, Winetraub Y, Skotheim JM. The Adder Phenomenon Emerges from Independent Control of Pre- and Post-Start Phases of the Budding Yeast Cell Cycle. *Curr Biol*. 2017;27(18):2774-2783.e3. doi:10.1016/j.cub.2017.08.015

35. Proulx-Giraldeau F, Skotheim JM, Francois P. Evolution of cell size control is canalized towards adders or sizers by cell cycle structure and selective pressures. *eLife*. 2022;11. doi:10.7554/eLife.79919

36. Garmendia-Torres C, Tassy O, Matifas A, Molina N, Charvin G. Multiple inputs ensure yeast cell size homeostasis during cell cycle progression. *eLife*. 2018;7. doi:10.7554/eLife.34025

37. Miller KE, Vargas-Garcia C, Singh A, Moseley JB. The fission yeast cell size control system integrates pathways measuring cell surface area, volume, and time. *Curr Biol*. 2023;33(16):3312-3324.e7. doi:10.1016/j.cub.2023.06.054

38. Fantes P, Nurse P. Control of cell size at division in fission yeast by a growth-modulated size control over nuclear division. *Exp Cell Res*. 1977;107(2):377-386. doi:10.1016/0014-4827(77)90359-7

39. Schmoller KM, Turner JJ, Kõivomägi M, Skotheim JM. Dilution of the cell cycle inhibitor Whi5 controls budding-yeast cell size. *Nature*. 2015;526(7572):268-272. doi:10.1038/nature14908

40. D’Ario M, Tavares R, Schiessl K, Desvoyes B, Gutierrez C, Howard M, Sablowski R. Cell size controlled in plants using DNA content as an internal scale. *Science*. 2021;372(6547):1176-1181. doi:10.1126/science.abb4348

41. Zatulovskiy E, Zhang S, Berenson DF, Topacio BR, Skotheim JM. Cell growth dilutes the cell cycle inhibitor Rb to trigger cell division. *Science*. 2020;369(6502):466-471. doi:10.1126/science.aaz6213

42. Zhang S, Zatulovskiy E, Arand J, Sage J, Skotheim JM. The cell cycle inhibitor RB is diluted in G1 and contributes to controlling cell size in the mouse liver. *Front Cell Dev Biol*. 2022;10:965595. doi:10.3389/fcell.2022.965595

43. Zhang S, Valenzuela LF, Zatulovskiy E, Mangiante L, Curtis C, Skotheim JM. The G1/S transition is promoted by Rb degradation via the E3 ligase UBR5. Published online October 4, 2023. doi:10.1101/2023.10.03.560768

44. Li Y, Liu D, López-Paz C, Olson BJ, Umen JG. A new class of cyclin dependent kinase in Chlamydomonas is required for coupling cell size to cell division. *eLife*. 2016;5:e10767. doi:10.7554/eLife.10767

45. Liu D, Lopez-Paz C, Li Y, Zhuang X, Umen J. Subscaling of a cytosolic RNA binding protein governs cell size homeostasis in the multiple fission alga Chlamydomonas. Dutcher SK, ed. *PLOS Genet*. 2024;20(3):e1010503. doi:10.1371/journal.pgen.1010503

46. Facchetti G, Knapp B, Flor-Parra I, Chang F, Howard M. Reprogramming Cdr2-Dependent Geometry-Based Cell Size Control in Fission Yeast. *Curr Biol*. 2019;29(2):350-358.e4. doi:10.1016/j.cub.2018.12.017

47. Hartwell LH. Genetic control of the cell division cycle in yeast. *J Mol Biol*. 1971;59(1):183-194. doi:10.1016/0022-2836(71)90420-7

48. Hartwell L. Genetic control of the cell division cycle in yeast *1IV. Genes controlling bud emergence and cytokinesis. *Exp Cell Res*. 1971;69(2):265-276. doi:10.1016/0014-4827(71)90223-0

49. Culotti J, Hartwell LH. Genetic control of the cell division cycle in yeast. *Exp Cell Res*. 1971;67(2):389-401. doi:10.1016/0014-4827(71)90424-1

50. Johnston G, Pringle J, Hartwell L. Coordination of growth with cell division in the yeast. *Exp Cell Res*. 1977;105(1):79-98. doi:10.1016/0014-4827(77)90154-9

51. Nasmyth K, Nurse P. Cell division cycle mutants altered in DNA replication and mitosis in the fission yeast Schizosaccharomyces pombe. *Mol Gen Genet MGG*. 1981;182(1):119-124. doi:10.1007/BF00422777

52. Nurse P, Bissett Y. Gene required in G1 for commitment to cell cycle and in G2 for control of mitosis in fission yeast. *Nature*. 1981;292(5823):558-560. doi:10.1038/292558a0

53. Thuriaux P, Nurse P, Carter B. Mutants altered in the control co-ordinating cell division with cell growth in the fission yeast Schizosaccharomyces pombe. *Mol Gen Genet MGG*. 1978;161(2):215-220. doi:10.1007/BF00274190

54. Nurse P. Genetic control of cell size at cell division in yeast. *Nature*. 1975;256(5518):547-551. doi:10.1038/256547a0

55. Killander D, Zetterberg A. Quantitative cytochemical studies on interphase growth. *Exp Cell Res*. 1965;38(2):272-284. doi:10.1016/0014-4827(65)90403-9

56. Lee MG, Nurse P. Complementation used to clone a human homologue of the fission yeast cell cycle control gene cdc2. *Nature*. 1987;327(6117):31-35. doi:10.1038/327031a0

57. Hindley J, Phear GA. Sequence of the cell division gene CDC2 from Schizosaccharomyces pombe; patterns of splicing and homology to protein kinases. *Gene*. 1984;31(1-3):129-134. doi:10.1016/0378-1119(84)90203-8

58. Beach D, Durkacz B, Nurse P. Functionally homologous cell cycle control genes in budding and fission yeast. *Nature*. 1982;300(5894):706-709. doi:10.1038/300706a0

59. Vanderwaeren L, Dok R, Voordeckers K, Nuyts S, Verstrepen KJ. Saccharomyces cerevisiae as a Model System for Eukaryotic Cell Biology, from Cell Cycle Control to DNA Damage Response. *Int J Mol Sci*. 2022;23(19):11665. doi:10.3390/ijms231911665

60. Douzery EJP, Snell EA, Bapteste E, Delsuc F, Philippe H. The timing of eukaryotic evolution: Does a relaxed molecular clock reconcile proteins and fossils? *Proc Natl Acad Sci*. 2004;101(43):15386-15391. doi:10.1073/pnas.0403984101

61. Kachroo AH, Laurent JM, Yellman CM, Meyer AG, Wilke CO, Marcotte EM. Systematic humanization of yeast genes reveals conserved functions and genetic modularity. *Science*. 2015;348(6237):921-925. doi:10.1126/science.aaa0769

62. Foury F. Human genetic diseases: a cross-talk between man and yeast. *Gene*. 1997;195(1):1-10. doi:10.1016/S0378-1119(97)00140-6

63. Goffeau A, Barrell BG, Bussey H, Davis RW, Dujon B, Feldmann H, Galibert F, Hoheisel JD, Jacq C, Johnston M, Louis EJ, Mewes HW, Murakami Y, Philippsen P, Tettelin H, Oliver SG. Life with 6000 Genes. *Science*. 1996;274(5287):546-567. doi:10.1126/science.274.5287.546

64. Cherry JM, Hong EL, Amundsen C, Balakrishnan R, Binkley G, Chan ET, Christie KR, Costanzo MC, Dwight SS, Engel SR, Fisk DG, Hirschman JE, Hitz BC, Karra K, Krieger CJ, Miyasato SR, Nash RS, Park J, Skrzypek MS, Simison M, Weng S, Wong ED. Saccharomyces Genome Database: the genomics resource of budding yeast. *Nucleic Acids Res*. 2012;40(D1):D700-D705. doi:10.1093/nar/gkr1029

65. Duina AA, Miller ME, Keeney JB. Budding Yeast for Budding Geneticists: A Primer on the *Saccharomyces cerevisiae* Model System. *Genetics*. 2014;197(1):33-48. doi:10.1534/genetics.114.163188

66. Chavez CM, Groenewald M, Hulfachor AB, Kpurubu G, Huerta R, Hittinger CT, Rokas A. The cell morphological diversity of *Saccharomycotina* yeasts. *FEMS Yeast Res*. 2024;24:foad055. doi:10.1093/femsyr/foad055

67. Li F, Long T, Lu Y, Ouyang Q, Tang C. The yeast cell-cycle network is robustly designed. *Proc Natl Acad Sci*. 2004;101(14):4781-4786. doi:10.1073/pnas.0305937101

68. Spellman PT, Sherlock G, Zhang MQ, Iyer VR, Anders K, Eisen MB, Brown PO, Botstein D, Futcher B. Comprehensive Identification of Cell Cycle–regulated Genes of the Yeast *Saccharomyces cerevisiae* by Microarray Hybridization. Fink GR, ed. *Mol Biol Cell*. 1998;9(12):3273-3297. doi:10.1091/mbc.9.12.3273

69. Skotheim JM, Di Talia S, Siggia ED, Cross FR. Positive feedback of G1 cyclins ensures coherent cell cycle entry. *Nature*. 2008;454(7202):291-296. doi:10.1038/nature07118

70. Di Talia S, Skotheim JM, Bean JM, Siggia ED, Cross FR. The effects of molecular noise and size control on variability in the budding yeast cell cycle. *Nature*. 2007;448(7156):947-951. doi:10.1038/nature06072

71. Schmoller KM, Lanz MC, Kim J, Koivomagi M, Qu Y, Tang C, Kukhtevich IV, Schneider R, Rudolf F, Moreno DF, Aldea M, Lucena R, Skotheim JM. Whi5 is diluted and protein synthesis does not dramatically increase in pre- Start G1. *Mol Biol Cell*. 2022;33(5). doi:10.1091/mbc.E21-01-0029

72. Qu Y, Jiang J, Liu X, Wei P, Yang X, Tang C. Cell Cycle Inhibitor Whi5 Records Environmental Information to Coordinate Growth and Division in Yeast. *Cell Rep*. 2019;29(4):987-994.e5. doi:10.1016/j.celrep.2019.09.030

73. Chen Y, Zhao G, Zahumensky J, Honey S, Futcher B. Differential Scaling of Gene Expression with Cell Size May Explain Size Control in Budding Yeast. *Mol Cell*. 2020;78(2):359-370.e6. doi:10.1016/j.molcel.2020.03.012

74. Leitao RM, Kellogg DR. The duration of mitosis and daughter cell size are modulated by nutrients in budding yeast. *J Cell Biol*. 2017;216(11):3463-3470. doi:10.1083/jcb.201609114

75. Talavera RA, Prichard BE, Sommer RA, Leitao RM, Sarabia CJ, Hazir S, Paulo JA, Gygi SP, Kellogg DR. Cell growth and nutrient availability control the mitotic exit signaling network in budding yeast. *J Cell Biol*. 2024;223(8):e202305008. doi:10.1083/jcb.202305008

76. De Bruin RAM, McDonald WH, Kalashnikova TI, Yates J, Wittenberg C. Cln3 Activates G1-Specific Transcription via Phosphorylation of the SBF Bound Repressor Whi5. *Cell*. 2004;117(7):887-898. doi:10.1016/j.cell.2004.05.025

77. Costanzo M, Nishikawa JL, Tang X, Millman JS, Schub O, Breitkreuz K, Dewar D, Rupes I, Andrews B, Tyers M. CDK Activity Antagonizes Whi5, an Inhibitor of G1/S Transcription in Yeast. *Cell*. 2004;117(7):899-913. doi:10.1016/j.cell.2004.05.024

78. Swaffer MP, Kim J, Chandler-Brown D, Langhinrichs M, Marinov GK, Greenleaf WJ, Kundaje A, Schmoller KM, Skotheim JM. Transcriptional and chromatin-based partitioning mechanisms uncouple protein scaling from cell size. *Mol Cell*. 2021;81(23):4861-4875.e7. doi:10.1016/j.molcel.2021.10.007

79. Barber F, Amir A, Murray AW. Cell-size regulation in budding yeast does not depend on linear accumulation of Whi5. *Proc Natl Acad Sci*. 2020;117(25):14243-14250. doi:10.1073/pnas.2001255117

80. Bastajian N, Friesen H, Andrews BJ. Bck2 Acts through the MADS Box Protein Mcm1 to Activate Cell-Cycle-Regulated Genes in Budding Yeast. *PLoS Genet*. 2013;9(5). doi:10.1371/journal.pgen.1003507

81. Kõivomägi M, Swaffer MP, Turner JJ, Marinov G, Skotheim JM. G 1 cyclin–Cdk promotes cell cycle entry through localized phosphorylation of RNA polymerase II. *Science*. 2021;374(6565):347-351. doi:10.1126/science.aba5186

82. Xiao J, Turner JJ, Kõivomägi M, Skotheim JM. Whi5 hypo- and hyper-phosphorylation dynamics control cell-cycle entry and progression. *Curr Biol*. 2024;34(11):2434-2447.e5. doi:10.1016/j.cub.2024.04.052

83. Doncic A, Falleur-Fettig M, Skotheim JM. Distinct Interactions Select and Maintain a Specific Cell Fate. *Mol Cell*. 2011;43(4):528-539. doi:10.1016/j.molcel.2011.06.025

84. Jorgensen P, Nishikawa JL, Breitkreutz BJ, Tyers M. Systematic Identification of Pathways That Couple Cell Growth and Division in Yeast. *Science*. 2002;297(5580):395-400. doi:10.1126/science.1070850

85. Teng X, Yau E, Sing C, Hardwick JM. Whi2 signals low leucine availability to halt yeast growth and cell death. *FEMS Yeast Res*. 2018;18(8):foy095. doi:10.1093/femsyr/foy095

86. Litsios A, Huberts DHEW, Terpstra HM, Guerra P, Schmidt A, Buczak K, Papagiannakis A, Rovetta M, Hekelaar J, Hubmann G, Exterkate M, Milias-Argeitis A, Heinemann M. Differential scaling between G1 protein production and cell size dynamics promotes commitment to the cell division cycle in budding yeast. *Nat Cell Biol*. 2019;21(11):1382-1392. doi:10.1038/s41556-019-0413-3

87. Dorsey S, Tollis S, Cheng J, Black L, Notley S, Tyers M, Royer CA. G1/S Transcription Factor Copy Number Is a Growth-Dependent Determinant of Cell Cycle Commitment in Yeast. *Cell Syst*. 2018;6(5):539-554.e11. doi:10.1016/j.cels.2018.04.012

88. Tollis S. The G1/S repressor WHI5 is expressed at similar levels throughout the cell cycle. *BMC Res Notes*. 2022;15(1). doi:10.1186/s13104-022-06142-9

89. Sommer RA, DeWitt JT, Tan R, Kellogg DR. Growth-dependent signals drive an increase in early G1 cyclin concentration to link cell cycle entry with cell growth. *eLife*. 2021;10. doi:10.7554/eLife.64364

90. Taberner FJ, Quilis I, Igual JC. Spatial regulation of the start repressor Whi5. *Cell Cycle Georget Tex*. 2009;8(18):3010-3018.

91. Balachandra S, Sarkar S, Amodeo AA. The Nuclear-to-Cytoplasmic Ratio: Coupling DNA Content to Cell Size, Cell Cycle, and Biosynthetic Capacity. *Annu Rev Genet*. 2022;56(1):165-185. doi:10.1146/annurev-genet-080320-030537

92. Ferrezuelo F, Aldea M, Futcher B. Bck2 is a phase-independent activator of cell cycle-regulated genes in yeast. *Cell Cycle*. 2009;8(2):239-252. doi:10.4161/cc.8.2.7543

93. Wijnen H, Futcher B. Genetic Analysis of the Shared Role of CLN3 and BCK2 at the G1-S Transition in Saccharomyces cerevisiae. *Genetics*. 1999;153(3):1131-1143. doi:10.1093/genetics/153.3.1131

94. Lee KS, Hines LK, Levin DE. *A Pair of Functionally Redundant Yeast Genes (PPZJ and PPZ2) Encoding Type 1-Related Protein Phosphatases Function within the PKC1-Mediated Pathway.*; 1993:5843-5853.

95. Epstein CB, Cross FR. Genes that can bypass the CLN requirement for Saccharomyces cerevisiae cell cycle START. *Mol Cell Biol*. 1994;14(3):2041-2047. doi:10.1128/mcb.14.3.2041-2047.1994

96. Soifer I, Barkai N. Systematic identification of cell size regulators in budding yeast. *Mol Syst Biol*. 2014;10(11). doi:10.15252/msb.20145345

97. Hall DD. Regulation of the Cln3-Cdc28 kinase by cAMP in Saccharomyces cerevisiae. *EMBO J*. 1998;17(15):4370-4378. doi:10.1093/emboj/17.15.4370

98. Parviz F, Heideman W. Growth-independent regulation of CLN3 mRNA levels by nutrients in Saccharomyces cerevisiae. *J Bacteriol*. 1998;180(2):225-230. doi:10.1128/JB.180.2.225-230.1998

99. Gomar-Alba M, Méndez E, Quilis I, Bañó MC, Igual JC. Whi7 is an unstable cell-cycle repressor of the Start transcriptional program. *Nat Commun*. 2017;8(1):329. doi:10.1038/s41467-017-00374-1

100. Yahya G, Parisi E, Flores A, Gallego C, Aldea M. A Whi7-Anchored Loop Controls the G1 Cdk-Cyclin Complex at Start. *Mol Cell*. 2014;53(1):115-126. doi:10.1016/j.molcel.2013.11.015

101. Ros-Carrero C, Spiridon-Bodi M, Igual JC, Gomar-Alba M. The CDK Pho85 inhibits Whi7 Start repressor to promote cell cycle entry in budding yeast. *EMBO Rep*. 2024;25(2):745-769. doi:10.1038/s44319-023-00049-7

102. Méndez E, Gomar-Alba M, Banõó MC, Mendoza M, Quilis I, Igual JC. The budding yeast Start repressor Whi7 differs in regulation from Whi5, emerging as a major cell cycle brake in response to stress. *J Cell Sci*. 2020;133(24). doi:10.1242/jcs.251413

103. García R, Bermejo C, Grau C, Pérez R, Rodríguez-Peña JM, Francois J, Nombela C, Arroyo J. The Global Transcriptional Response to Transient Cell Wall Damage in Saccharomyces

cerevisiae and Its Regulation by the Cell Integrity Signaling Pathway. *J Biol Chem*. 2004;279(15):15183-15195. doi:10.1074/jbc.M312954200

104. Buschauer R, Matsuo Y, Sugiyama T, Chen YH, Alhusaini N, Sweet T, Ikeuchi K, Cheng J, Matsuki Y, Nobuta R, Gilmozzi A, Berninghausen O, Tesina P, Becker T, Coller J, Inada T, Beckmann R. The Ccr4-Not complex monitors the translating ribosome for codon optimality. *Science*. 2020;368(6488):eaay6912. doi:10.1126/science.aay6912

105. Collart MA. The Ccr4-Not complex is a key regulator of eukaryotic gene expression. *WIREs RNA*. 2016;7(4):438-454. doi:10.1002/wrna.1332

106. Manukyan A, Zhang J, Thippeswamy U, Yang J, Zavala N, Mudannayake MP, Asmussen M, Schneider C, Schneider BL. Ccr4 alters cell size in yeast by modulating the timing of CLN1 and CLN2 expression. *Genetics*. 2008;179(1):345-357. doi:10.1534/genetics.108.086744

107. Ferrezuelo F, Colomina N, Palmisano A, Garí E, Gallego C, Csikász-Nagy A, Aldea M. The critical size is set at a single-cell level by growth rate to attain homeostasis and adaptation. *Nat Commun*. 2012;3. doi:10.1038/ncomms2015

108. Irvali D, Schlottmann FP, Muralidhara P, Nadelson I, Kleemann K, Wood NE, Doncic A, Ewald JC. When yeast cells change their mind: cell cycle “Start” is reversible under starvation. *EMBO J*. 2023;42(2). doi:10.15252/embj.2021110321

109. Argüello-Miranda O, Marchand AJ, Kennedy T, Russo MAX, Noh J. Cell cycle–independent integration of stress signals by Xbp1 promotes Non-G1/G0 quiescence entry. *J Cell Biol*. 2022;221(1):e202103171. doi:10.1083/jcb.202103171

110. Wood NE, Kositangool P, Hariri H, Marchand AJ, Henne WM. Nutrient Signaling, Stress Response, and Inter-organelle Communication Are Non-canonical Determinants of Cell Fate. *Cell Rep*. 2020;33(9):108446. doi:10.1016/j.celrep.2020.108446

111. Ewald JC. How yeast coordinates metabolism, growth and division. *Curr Opin Microbiol*. 2018;45:1-7. doi:10.1016/j.mib.2017.12.012

112. Dechant R, Peter M. Nutrient signals driving cell growth. *Curr Opin Cell Biol*. 2008;20(6):678-687. doi:10.1016/j.ceb.2008.09.009

113. Van Zeebroeck G, Demuyser L, Zhang Z, Cottignie I, Thevelein JM. Nutrient sensing and cAMP signaling in yeast: G-protein coupled receptor versus transceptor activation of PKA. *Microb Cell*. 2021;8(1):17-27. doi:10.15698/mic2021.01.740

114. Steyfkens F, Zhang Z, Van Zeebroeck G, Thevelein JM. Multiple Transceptors for Macro- and Micro-Nutrients Control Diverse Cellular Properties Through the PKA Pathway in Yeast: A Paradigm for the Rapidly Expanding World of Eukaryotic Nutrient Transceptors Up to Those in Human Cells. *Front Pharmacol*. 2018;9:191. doi:10.3389/fphar.2018.00191

115. González A, Hall MN. Nutrient sensing and TOR signaling in yeast and mammals. *EMBO J*. 2017;36(4):397-408. doi:10.15252/embj.201696010

116. Pérez-Hidalgo L, Moreno S. Coupling TOR to the Cell Cycle by the Greatwall–Endosulfine–PP2A-B55 Pathway. *Biomolecules*. 2017;7(3):59. doi:10.3390/biom7030059

117. Chica N, Rozalén AE, Pérez-Hidalgo L, Rubio A, Novak B, Moreno S. Nutritional control of cell size by the greatwall-endosulfine-PP2A·B55 pathway. *Curr Biol*. 2016;26(3):319-330. doi:10.1016/j.cub.2015.12.035

118. García-Blanco N, Vázquez-Bolado A, Moreno S. Greatwall-Endosulfine: A Molecular Switch that Regulates PP2A/B55 Protein Phosphatase Activity in Dividing and Quiescent Cells. *Int J Mol Sci*. 2019;20(24):6228. doi:10.3390/ijms20246228

119. Tyers M, Tokiwa G, Nash R, Futcher B. The Cln3-Cdc28 kinase complex of S. cerevisiae is regulated by proteolysis and phosphorylation. *EMBO J*. 1992;11(5):1773-1784. doi:10.1002/j.1460-2075.1992.tb05229.x

120. Pedruzzi I, Dubouloz F, Cameroni E, Wanke V, Roosen J, Winderickx J, De Virgilio C. TOR and PKA Signaling Pathways Converge on the Protein Kinase Rim15 to Control Entry into G0. *Mol Cell*. 2003;12(6):1607-1613. doi:10.1016/S1097-2765(03)00485-4

121. Hartwell LH, Culotti J, Reid B. Genetic Control of the Cell-Division Cycle in Yeast, I. Detection of Mutants. *Proc Natl Acad Sci*. 1970;66(2):352-359. doi:10.1073/pnas.66.2.352

122. Padovani F, Mairhörmann B, Falter-Braun P, Lengefeld J, Schmoller KM. Segmentation, tracking and cell cycle analysis of live-cell imaging data with Cell-ACDC. *BMC Biol*. 2022;20(1):174-174. doi:10.1186/s12915-022-01372-6

123. Dietler N, Minder M, Gligorovski V, Economou AM, Joly DAHL, Sadeghi A, Chan CHM, Koziński M, Weigert M, Bitbol AF, Rahi SJ. A convolutional neural network segments yeast microscopy images with high accuracy. *Nat Commun*. 2020;11(1):5723-5723. doi:10.1038/s41467-020-19557-4

124. Bheda P, Aguilar-Gómez D, Becker NB, Becker J, Stavrou E, Kukhtevich I, Höfer T, Maerkl S, Charvin G, Marr C, Kirmizis A, Schneider R. Single-Cell Tracing Dissects Regulation of Maintenance and Inheritance of Transcriptional Reinduction Memory. *Mol Cell*. 2020;78(5):915-925.e7. doi:10.1016/j.molcel.2020.04.016

125. Schuh L, Kukhtevich I, Bheda P, Schulz M, Bordukova M, Schneider R, Marr C. Altered expression response upon repeated gene repression in single yeast cells. *PLOS Comput Biol*. 2022;18(10):e1010640-e1010640. doi:10.1371/journal.pcbi.1010640

126. Shabestary K, Klemm C, Carling B, Marshall J, Savigny J, Storch M, Ledesma-Amaro R. Phenotypic heterogeneity follows a growth-viability tradeoff in response to amino acid identity. *Nat Commun*. 2024;15(1):6515-6515. doi:10.1038/s41467-024-50602-8

127. Stockwell SR, Rifkin SA. A living vector field reveals constraints on galactose network induction in yeast. *Mol Syst Biol*. 2017;13(1). doi:10.15252/msb.20167323

128. Hesketh A, Vergnano M, Wan C, Oliver SG. Bacterial Signaling Nucleotides Inhibit Yeast Cell Growth by Impacting Mitochondrial and Other Specifically Eukaryotic Functions. Davies JE, ed. *mBio*. 2017;8(4):e01047-17. doi:10.1128/mBio.01047-17

129. Claude KL, Bureik D, Chatzitheodoridou D, Adarska P, Singh A, Schmoller KM. Transcription coordinates histone amounts and genome content. *Nat Commun*. 2021;12(1):4202. doi:10.1038/s41467-021-24451-8

130. Padovani F, Čavka I, Neves ARR, López CP, Al-Refaie N, Bolcato L, Chatzitheodoridou D, Chadha Y, Su XA, Lengefeld J, Cabianca DS, Köhler S, Schmoller KM. SpotMAX: a generalist framework for multi-dimensional automatic spot detection and quantification. Published online October 23, 2024. doi:10.1101/2024.10.22.619610

131. Chatzitheodoridou D, Bureik D, Padovani F, Nadimpalli KV, Schmoller KM. Decoupled transcript and protein concentrations ensure histone homeostasis in different nutrients. *EMBO J*. 2024;43(19):1-28. doi:10.1038/s44318-024-00227-w

132. Di Como CJ, Chang H, Arndt KT. Activation of *CLN1* and *CLN2* G_1 Cyclin Gene Expression by BCK2. *Mol Cell Biol*. 1995;15(4):1835-1846. doi:10.1128/MCB.15.4.1835

133. Lew DJ, Marini NJ, Reed SI. Different G1 cyclins control the timing of cell cycle commitment in mother and daughter cells of the budding yeast S. cerevisiae. *Cell*. 1992;69(2):317-327. doi:10.1016/0092-8674(92)90412-6

134. Jorgensen P, Tyers M. How Cells Coordinate Growth and Division. *Curr Biol*. 2004;14(23):R1014-R1027. doi:10.1016/j.cub.2004.11.027

135. Barber F, Amir A, Murray AW. Cell-size regulation in budding yeast does not depend on linear accumulation of Whi5. doi:10.1073/pnas.2001255117/-/DCSupplemental

136. Liu X, Yan J, Kirschner MW. Cell size homeostasis is tightly controlled throughout the cell cycle. Pines J, ed. *PLOS Biol*. 2024;22(1):e3002453. doi:10.1371/journal.pbio.3002453

137. Travesa A, Kalashnikova TI, De Bruin RAM, Cass SR, Chahwan C, Lee DE, Lowndes NF, Wittenberg C. Repression of G_1/S Transcription Is Mediated via Interaction of the GTB Motifs of Nrm1 and Whi5 with Swi6. *Mol Cell Biol*. 2013;33(8):1476-1486. doi:10.1128/MCB.01333-12

138. Bloom K. Nuclear migration: Cortical anchors for cytoplasmic dynein. *Curr Biol*. 2001;11(8):R326-R329. doi:10.1016/S0960-9822(01)00176-2

139. Bhaduri S, Pryciak PM. Cyclin-Specific Docking Motifs Promote Phosphorylation of Yeast Signaling Proteins by G1/S Cdk Complexes. *Curr Biol*. 2011;21(19):1615-1623. doi:10.1016/j.cub.2011.08.033

140. Liu X, Wang X, Yang X, Liu S, Jiang L, Qu Y, Hu L, Ouyang Q, Tang C. Reliable cell cycle commitment in budding yeast is ensured by signal integration. *eLife*. 2015;4:e03977. doi:10.7554/eLife.03977

141. Entian KD, Meurer B, Helmut K, Mann KH, Mecke D. Studies on the regulation of enolases and compartmentation of cytosolic enzymes in Saccharomyces cerevisiae. *Biochim Biophys Acta BBA - Gen Subj*. 1987;923(2):214-221. doi:10.1016/0304-4165(87)90006-7

142. Chadha Y, Kukhtevich IV, Padovani F, Schneider R, Schmoller KM. Single-cell imaging reveals a key role of Bck2 in budding yeast cell size adaptation to nutrient challenges. *bioRxiv*. Published online January 1, 2024:2024.10.04.616606. doi:10.1101/2024.10.04.616606

143. Levin DE. Cell Wall Integrity Signaling in Saccharomyces cerevisiae. *Microbiol Mol Biol Rev*. 2005;69(2):262-291. doi:10.1128/MMBR.69.2.262-291.2005

144. Kuravi VK, Kurischko C, Puri M, Luca FC. Cbk1 kinase and Bck2 control MAP kinase activation and inactivation during heat shock. *Mol Biol Cell*. 2011;22(24):4892-4907. doi:10.1091/mbc.e11-04-0371

145. Martin-Yken H, Dagkessamanskaia A, Talibi D, Francois J. KNR4 is a member of the PKC1 signalling pathway and genetically interacts with BCK2, a gene involved in cell cycle progression in Saccharomyces cerevisiae. *Curr Genet*. 2002;41(5):323-332. doi:10.1007/s00294-002-0299-6

146. Visinoni F, Royle W, Scholey R, Hu Y, Timouma S, Zeef L, Louis EJ, Delneri D. Impact of inter-species hybridisation on antifungal drug response in the Saccharomyces genus. *bioRxiv*. Published online January 2024:2024.01.29.577396-2024.01.29.577396. doi:10.1101/2024.01.29.577396

147. Min M, Rong Y, Tian C, Spencer SL. Temporal integration of mitogen history in mother cells controls proliferation of daughter cells. *Science*. 2020;368(6496):1261-1265. doi:10.1126/science.aay8241